Preparation and characterisation of certain II-VI, I-III-VI$_2$ semiconductor thin films and transparent conducting oxides

Thesis submitted to
COCHIN UNIVERSITY OF SCIENCE AND TECHNOLOGY
in partial fulfillment of the requirements
for the award of the degree of
DOCTOR OF PHILOSOPHY

Aldrin Antony

Department of Physics
Cochin University of Science and Technology
Cochin – 682 022, Kerala, India

October 2004

Preparation and characterisation of certain II-VI, I-III-VI$_2$ semiconductor thin films and transparent conducting oxides

Ph.D thesis in the field of material science

Author:

Aldrin Antony
Optoelectronics Device Laboratory
Department of Physics
Cochin University of Science and Technology
Cochin – 682 022, Kerala, India
email: aldrinantony@hotmail.com

Supervisor:

Dr. M.K. Jayaraj
Reader
Optoelectronics Device Laboratory
Department of Physics
Cochin University of Science and Technology
Cochin – 682 022, Kerala, India
email: mkj@cusat.ac.in

October 2004

Dedicated to my Parents and brother

Dr. M.K. Jayaraj
Reader
Department of Physics
Cochin University of Science and Technology
Cochin – 682 022

_____

18th October 2004

Certificate

Certified that the work presented in this thesis entitled "*Preparation and characterisation of certain II-VI, I-III-VI$_2$ semiconductor thin films and transparent conducting oxides*" is based on the authentic record of research done by *Mr. Aldrin Antony* under my guidance in the Department of Physics, Cochin University of Science and Technology, Cochin – 682 022 and has not been included in any other thesis submitted for the award of any degree.

Dr. M.K. Jayaraj

(Supervising Guide)

_____

Phone : +91 484 2577404 extn 33   Fax: 91 484 2577595   email: mkj@cusat.ac.in

Declaration

Certified that the work presented in this thesis entitled "*Preparation and characterisation of certain II-VI, I-III-VI$_2$ semiconductor thin films and transparent conducting oxides*" is based on the original research work done by me under the supervision and guidance of Dr. M.K. Jayaraj, Reader, Department of Physics, Cochin University of Science and Technology, Cochin-682022 has not been included in any other thesis submitted previously for the award of any degree.

Cochin – 22
18th October 2004
Aldrin Antony

Acknowledgements

_____

Contents

CHAPTER 3

Chemical bath deposition of II-VI semiconductor
thin films for buffer layer application in solar cells   **53**

Part A

Preparation and characterisation of CdS thin films by
chemical bath deposition

Part B

Part C

Part B

CHAPTER 5

Preparation and characterisation of indium tin oxide thin films by rf magnetron sputtering **165**

CHAPTER 6

Preface

There is an increasing demand for renewable energies due to the limited availability of fossil and nuclear fuels and due to growing environmental problems. Photovoltaic (PV) energy conversion has the potential to contribute significantly to the electrical energy generation in the future. Currently, the cost for photovoltaic systems is one of the main obstacles preventing production and application on a large scale. The photovoltaic research is now focused on the development of materials that will allow mass production without compromising on the conversion efficiencies. Among important selection criteria of PV material and in particular for thin films, are a suitable band gap, high absorption coefficient and reproducible deposition processes capable of large-volume and low cost production. The chalcopyrite semiconductor thin films such as Copper indium selenide and Copper indium sulphide are the materials that are being intensively investigated for lowering the cost of solar cells. Conversion efficiencies of 19 % have been reported for laboratory scale solar cell based on $CuInSe_2$ and its alloys.

The main objective of this thesis work is to optimise the growth conditions of materials suitable for the fabrication of solar cell, employing cost effective techniques. A typical heterojunction thin film solar cell consists of an absorber layer, buffer layer and transparent conducting contacts. The most appropriate techniques have been used for depositing these different layers, viz; chemical bath deposition for the window layer, flash evaporation and two-stage process for the absorber layer, and RF magnetron sputtering for the transparent conducting layer. Low cost experimental setups were fabricated for selenisation and sulphurisation experiments, and the magnetron gun for the RF sputtering was indigenously fabricated. The films thus grown were characterised using different tools. A powder X-ray diffractometer was used to analyse the crystalline nature of the films. The energy dispersive X-ray analysis (EDX) and scanning electron microscopy

(SEM) were used for evaluating the composition and morphology of the films. Optical properties were investigated using the UV-Vis-NIR spectrophotometer by recording the transmission/absorption spectra. The electrical properties were studied using the two probe and four probe electrical measurements. Nature of conductivity of the films was determined by thermoprobe and thermopower measurements. The deposition conditions and the process parameters were optimised based on these characterisations.

The results of the investigations are presented in 6 chapters. An overview of the developments in the filed of photovoltaic is briefly presented in *Chapter 1* with focus on the I-III-VI$_2$ based solar cells. The advantages of I-III-VI$_2$ group chalcopyrite thin film semiconductors over other solar cell materials are discussed. The device structure, performance and the defect chemistry of a solar cell is also presented in this section. The review gives an insight into the developments in the field of photovoltaic and references to the literature on chalcopyrite polycrystalline solar cells during the past decade.

Chapter 2 deals with the various deposition methods and characterisation tools employed in the present study. Different customised experimental setups were fabricated for thin film depositions.

Chemical bath deposition (CBD) was effectively utilised for the preparation of some II-VI group semiconductors as the buffer layers for solar cells and the results are summarised in *Chapter 3*. The chapter is divided into four parts and the relevant literature review is included in each part. Part A describes the preparation and characterisation of CdS thin films. The chemical bath deposited CdS films were uniform and was having a high carrier concentration of $\sim 10^{17}$ carriers/cm^3. The films showed a blue shift in the absorption edge (E$_g$) due to the nanocrystalline growth, which is advantageous for the application in solar cells to get higher conversion efficiency. The relatively low band gap of the CdS films limits the conversion efficiency of the solar cells. Higher band gap buffer layers are needed to enhance the response in short wavelength region. With this outlook a ternary derivate of CdS, Zn$_x$Cd$_{1-x}$S films were prepared by CBD.

The Zn incorporation into the CdS facilitates band gap engineering. It was observed that, though the band gap increased with Zn incorporation, the resistivity of the film also increases, which is undesirable for a window layer in the solar cell. In order to enhance the conductivity, indium was doped by adding $InCl_3$ in the chemical bath for the growth of $Zn_xCd_{1-x}S$ films. The results of the preparation and characterisation of $Zn_xCd_{1-x}S$ thin films and the effect of indium doping are presented in Part B of Chapter 3. Part C deals with the preparation and characterisation of a cadmium free, wide band gap ZnS buffer layer. ZnS thin films were prepared from two different host solutions of Zn. The reaction mechanism and the effect of pH on the electrical and optical properties of the CBD-ZnS are presented. The properties of CBD-ZnS are compared with the ZnS films prepared by electron beam evaporation. Part D describes a simple method to prepare ZnO thin films from the chemical bath deposited ZnS films by thermal oxidation. Poly crystalline ZnO films were obtained and the films were showing high resistivity.

Chapter 4 describes the preparation and characterisation of chalcopyrite absorber layers for solar cells. The chapter is divided into two parts, Part A discusses the preparation and characterisation of copper indium selenide and Part B deals with copper indium sulphide thin films. Chalcopyrite $CuInSe_2$ thin films were prepared by flash evaporation followed by the annealing in selenium vapour. The effect of selenisation on the electrical and optical properties of the films is investigated. $CuInS_2$ is a promising chalcopyrite material, which is expected to show superior efficiency than $CuInSe_2$ due to its ideal band gap. The 'two stage process'; which is a simple, scalable and cost effective technique; was optimised for preparing single phase, p-type $CuInS_2$ thin films. The two-stage process involves the preparation of Cu-In alloy followed by the sulphurisation using H_2S gas. The dependence of processing parameters and the Cu/In ratios of the starting precursors on the electrical, optical and structural properties have been studied and are presented in Part B of Chapter 4.

Tin doped indium oxide (ITO) thin films are having numerous applications in opto-electronic devices and are widely used as the transparent conducing electrode in solar cells. ITO films have been deposited by RF magnetron sputtering at room temperature and the results are presented in *Chapter 5*. The effect of target to substrate spacing and the post deposition annealing in vacuum, on the structural, electrical and optical properties of the films are discussed. Poly crystalline films were obtained by the room temperature sputtering, which is advantageous for many device applications where flexible substrates are used. Highly conducting and transparent films were obtained by post deposition vacuum annealing. *Chapter 6* is the concluding chapter, which highlights the major results and proposes the future steps for fabricating and improving the device performance using the techniques developed for the growth of various layers presented in the thesis.

Part of the thesis has been published in the internationally referred journals.

I. Growth of CuInS$_2$ thin films by sulphurisation of Cu-In alloys, **Aldrin Antony**, Asha A.S., Rahana Yoosuf, Manoj R., M.K.Jayaraj, Sol. Energy Mater. Sol. Cells 81 (2004) 407

II. Influence of target to substrate spacing on the properties of ITO thin films, **Aldrin Antony**, Nisha M., Manoj R., M.K. Jayaraj, Appl. Surf. Sci. 225 (2004) 294

III. Preparation and characterisation of ZnS thin films by chemical bath deposition and electron beam evaporation, Murali K.V., **Aldrin Antony**, Manoj Ramachandran. and M. K. Jayaraj, Materials, Active Devices and Optical Amplifiers, (Eds) C. Hasnain, J. Connie, H. Dexiu, N. Yoshiaki, R. Xiaomin, in: Proc. SPIE Int. Conf. APOC 2003, Wuhan,China, 5280 (2004) p 600

IV. Effect of pH on the growth and properties of chemical bath deposited ZnS thin films, **Aldrin Antony**, K.V. Murali, Manoj R., M.K. Jayaraj, Mater. Phys. and Chem. (in press)

V. Effect of selenisation on the flash evaporated copper indium selenide thin films, **Aldrin Antony** and M.K.Jayaraj (communicated)

VI. ZnO thin films prepared by the thermal oxidation of chemical bath deposited ZnS, **Aldrin Antony** and M.K.Jayaraj (communicated)

Conference Proceedings

I. Influence of substrate temperature on the properties of rf magnetron sputtered ITO thin films, Anusha S, Nisha M, **Aldrin Antony**, Manoj R and M.K. Jayaraj, DAE Solid State Physics Symposium, 2003

II. Thermal diffusivity of flash evaporated $CuInSe_2$ thin films by photothermal beam deflection, Mohamed M. A. Fadhali, Asha A. S., **Aldrin Antony**, Jyotsna Ravi, K. P. R. Nair, T. M. A. Rasheed and M. K. Jayaraj, DAE Solid State Physics Symposium, 2003

III. Effect of heat treatment on the properties of rf magnetron sputtered ITO thin films, M.Nisha, **Aldrin Antony**, Manoj.R and M.K.Jayaraj, in: Proc. DAE Solid State Physics Symposium, 45 (2002) p327

IV. Preparation and characterisation of single phase $CuInS_2$ films by two stage process, **Aldrin antony**, M.Gafoor, Asha.A.S, Rahna Yousf and M.K.Jayaraj, in: Proc. DAE Solid State Physics Symposium, 45 (2002) p475

V. Chemical Bath deposition of indium doped ZnCdS Thin Films, **Aldrin Antony**, Manoj.R and M.K.Jayaraj, in: Proc. National conf. Thin Film Techniques and Applications (2002) p68

VI. Characterisation of $Zn_xCd_{1-x}S$ thin films grown by chemical bath depostion, **Aldrin Antony**, A.K.Sandya, Lissa J Mangattu, Deneshan.P and M.K.Jayaraj, National Seminar on Physics of Materials for Electronics and Optoelectronics Devices, 1999

Other publications to which author has contributed,

   I. β-In$_2$S$_3$ Thin Films Prepared by The Sulphurisation of Evaporated Indium Films, Rahana Yoosuf, Jerome Kalloor Cheekku, **Aldrin Antony**, Manoj Ramachandran and Madambi K. Jayaraj, Materials, Active Devices and Optical Amplifiers, (Eds) C. Hasnain, J. Connie, H. Dexiu, N. Yoshiaki, R. Xiaomin, in: Proc. SPIE Int. Conf. APOC 2003, Wuhan,China, 5280 (2004) p669

  II. Transparent conducting zinc oxide thin film prepared by off-axis rf magnetron sputtering, M.K.Jayaraj, **Aldrin Antony**, and R. Manoj, Bull Mater. Sci. 25 (2002) 227

 III. Green electroluminescence from Zn$_{1-x}$Mg$_x$S:Mn ACTFEL devices, M.K.Jayaraj, **Aldrin Antony** and Deneshan.P, Thin Solid Films 389 (2001) 284

  IV. Effect of oxygen partial pressure on growth of Pulsed Laser Deposited ZnO:Al thin films, Manoj R, Maneesh C, **Aldrin Antony** and M.K. Jayaraj, Second National Symposium on Pulsed Laser Deposition of thin films 2003.

   V. Growth of Single Phase In$_2$S$_3$ Films by Chalcogenisation of Metallic Indium Films, Rahana Yoosuf, **Aldrin Antony**, Manoj R, Mini Krishna, Nisha M and M.K.Jayaraj, DAE Solid State Physics Symposium, 2003

  VI. Preparation of ZnO:Al thin films by pulsed laser deposition, Manoj.R, **Aldrin Antony**, Vineeth.C and M.K.Jayaraj, in: Proc. of DAE-BRNS National Laser Symposium (2002) p423

 VII. Preparation of ZnO:Ga thin films by pulsed laser deposition, Vineeth.C, Manoj.R, **Aldrin Antony**, Reeja.M, and M.K.Jayaraj, in: Proc. DAE Solid State Physics Symposium, 45 (2002) p329

VIII. Zinc Oxide thin Films Prepared by off axis rf Magnetron sputtering, Manoj.R, **Aldrin Antony** and M.K.Jayaraj, Proc. National conference on Thin Film Techniques and Applications, (2002) p39

  IX. A.S. Asha, Rahana Yoosuf, G. Sukesh, Aldrin Antony and M.K. Jayaraj, 2nd International Conf. on Electrochemical Power Systems (Hyderabad, India, December 2004)

CHAPTER 1

General Introduction to solar cells and importance of chalcopyrite thin films

1.1 Introduction

Today one of our major challenges to the world scientific community is to find a sustainable supply of electrical energy. At present, most of our energy comes from fossil (i.e. coal, liquefied petroleum, oil, natural gas) and nuclear resources. Not only are these sources of energy non-renewable and in dwindling quantities, they can also be polluting to the environment. Burning of fossil fuels releases almost 7 billion tons of CO_2 per year, resulting in environmental problems such as the greenhouse effect and global warming. Burning of unrefined coal also results in acid rain, which is directly responsible for large area forest and wildlife destruction as well as soil pollution. A series of incidents at several nuclear power plants, combined with the lack of a long-term waste disposal strategy, has resulted in the termination of nuclear power programmes in the USA and most European countries. These events have stimulated interest in clean renewable energy alternatives. In general these energy systems do not depend on resources, which are limited to our earth, but on the constant radiation of the sun. There are three basic reasons for the development of alternative energy sources:

- o The rapid depletion of oil and gas resources
- o The need to develop clean renewable energy sources to curb the generation of greenhouse gases (CO_2 and CH_4)
- o Growing worldwide demand for electrical energy, especially in rural areas

Potential new energy sources include biomass, geothermal energy, hydroelectricity, ocean, thermal energy, wind energy and the direct conversion of sunlight into electricity by the photovoltaic (PV) effect. Among these renewable energies, the direct conversion of sunlight is the most promising. The photovoltaic source of energy, i.e. solar irradiation, has the advantage of being widely distributed over the world, although the largest demand does not always correlate with the supply. The solar irradiation impinging on the earth's surface is not a limiting factor and supersedes our needs. Future design of our energy system will be a combination of different alternatives. Solar cells never will or can constitute the only solution. The resource must be sustainable and the price must be in

level with today's cost of energy. Furthermore we must have a technology to scale up and produce this system. Solar cell technology is about to meet all of these standards. Equally important is the role of PV systems in meeting some of the most essential needs of humanity. In India, by the end of 2002, 5084 solar PV water pumps had been installed in rural areas, with a total capacity of about 5.55 MW power. And 2,400 villages and hamlets had been electrified in India with PV. This barely taps into the potential for bringing fresh water and light to the poor and remote populations in India, but it certainly confirms the feasibility and benefits [1].

1.2 History of solar cells

The development of the solar cell starts from the work of the French experimental physicist Antoine-Cesar Becquerel back in the 19th century. In 1839, Becquerel observed that shining light on an electrode submerged in a conductive solution would create an electric current. In the same year another French physicist, Edmond Becquerel found that a certain material would produce a small amount of an electric current when it was exposed to a light. This was described as the photovoltaic (PV) effect. It was an interesting part of science for the next three quarters of a century. In 1877, Charles Fritts constructed the first true solar cell (made from solid materials) by using junctions formed by coating the semiconductor selenium with an ultrathin, nearly transparent layer of gold. Fritts's devices were very inefficient, transforming less than 1 percent of the absorbed light into electrical energy, but they were a start.

Substantial improvements in solar cell efficiency had to wait for a better understanding of the physical principles involved in their design, provided by Einstein in 1905 and Schottky in 1930. By 1927 another metal-semiconductor junction solar cell made of copper and the semiconductor copper oxide, had been demonstrated. By the 1930s both the selenium cell and the copper oxide cell were being employed in light-sensitive devices such as photometers for use in photography.

Solar cell efficiency finally saw substantial progress with the development of the first silicon cell by an American scientist Russell Ohl in 1941. In 1954, three other American researchers, G.L. Pearson, Daryl Chapin, and Calvin Fuller, demonstrated a further-refined silicon solar cell capable of 6% energy conversion efficiency (in direct sunlight). Parallel efforts were also initiated to find alternative materials that could be processed in thin film form to provide a still lower-cost alternative to crystalline silicon. Initial efforts were concentrated on thin film solar cells of polycrystalline Cu_2S/CdS and amorphous silicon. Cu_2S/CdS type solar cells displayed severe stability problems and their development were discontinued by the early 1980s. Amorphous silicon solar cell technology has been more successful, and products based on this technology became available commercially. However, because these products have low conversion efficiencies, their use is limited to special consumer applications. To respond to the potential demand in the power generation market, which required module with high efficiencies in excess of 10%, research and development efforts shifted gradually to two other polycrystalline thin film material systems: copper indium diselenide ($CuInSe_2$) and cadmium telluride (CdTe) based solar cells. During the past twenty years, these research and development efforts resulted in conversion efficiency improvements from 6% to 19% for $CuInSe_2$ based, and from 8% to 16% for CdTe based, small area, laboratory devices. As a result, these materials systems are being considered seriously as the basis of PV module technologies for terrestrial power generation.

1.3 Principle of solar cells

Solar cells, or photovoltaic devices, are devices that convert sunlight directly into electricity. The power generating part of a solid-state solar cell consists of a semiconductor that forms a rectifying junction either with another semiconductor or with a metal. Thus, the structure is basically a pn-diode or a Schottky diode. In some junctions, a thin insulator film is placed between the two semiconductors or between semiconductor and the metal, thereby forming a semiconductor – insulator– semiconductor or a metal – insulator – semiconductor junction. Moreover, pn-junctions may be classified into

4

homojunctions and heterojunctions according to whether the semiconductor material on one side of the junction is the same as or different from that on the other side. Also liquid-junction solar cells exist where the junction is formed between a semiconductor and a liquid electrolyte.

When the junction is illuminated, the semiconductor material absorbs the incoming photons if their energy hν is larger than that of the band gap of the semiconductor material. The absorbed photons generate electron-hole pairs. These photogenerated electron-hole pairs are separated by the internal electric field of the junction: holes drift to one electrode and electrons to the other one [2,3]. The electricity produced by a photovoltaic device is direct current and can be used as such, converted into alternating current, or stored for later use.
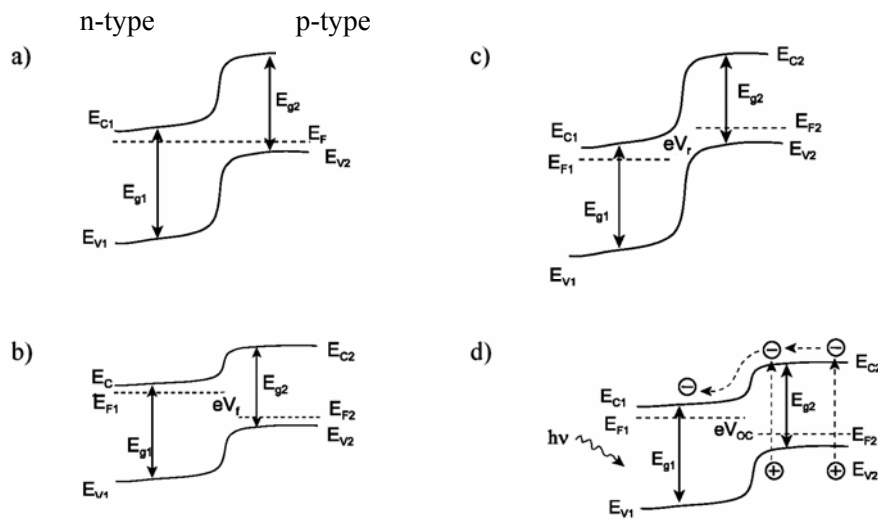
Figure 1.1 Energy band diagram of a pn-heterojunction solar cell: (a) at thermal equilibrium in dark (b) under a forward bias (c) under a reverse bias and (d) under illumination, open circuit conditions.

Figure 1 presents a schematic energy band diagram of a pn-heterojunction solar cell (a) at thermal equilibrium in dark, (b) under a forward bias, (c) under a reverse bias, and (d) under illumination, open circuit conditions. E_{ci}

and E_{vi} in Fig.1.1 refer to the conduction and valence band energies of n and p type semiconductor respectively. E_{gi} and E_{Fi} are the band gaps and Fermi levels, respectively. In the absence of an applied potential (Fig.1.1a), the Fermi levels of the semiconductors coincide, and there is no current flow. A forward bias V_f (Fig.1.1b) shifts the Fermi level of the n-type semiconductor upwards and that of the p-type semiconductor downwards, thus lowering the potential energy barrier of the junction, and facilitating the current flow across it. The effect of a reverse bias V_r (Fig.1.1c) is opposite: it increases the potential barrier and thus impedes the current flow. Illumination of the junction (Fig.1.1d) creates electron-hole pairs, causing an increase in the minority carrier concentration. The potential energy barrier decreases, allowing the current to flow, and a photovoltage V_{OC} (photovoltage under open circuit conditions, or open circuit voltage) is generated across the junction [2, 4].

Solar cells are characterized by current-voltage (I-V) measurements in the dark and under standardized illumination that simulates the sunlight. Figure1.2 shows an example of diode characteristics of a solar cell in the dark and under illumination. The most important parameters that describe the performance of a solar cell (open circuit voltage V_{OC}, short circuit current density J_{SC} and fill factor FF) can be derived from the J-V curve measured under illumination.
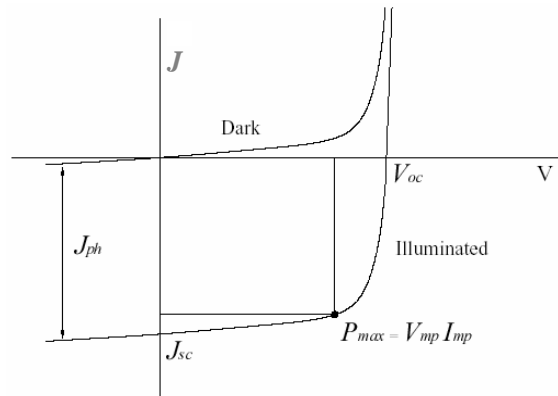
Fig. 1. 2 Current-voltage characteristics of a solar cell in dark and under illumination

The open circuit voltage is limited by the band gap energy E_g of the absorber material, and its maximum value is calculated by dividing the band gap energy by the charge of an electron (E_g /e). Because of electron-hole pair recombination, the open circuit voltages of real solar cells are considerably below their maximum limits. The maximum value of short circuit current density, in turn, is the photogenerated current density J_{ph} [3] that depends on the amount of absorbed light. Fill factor, which describes the shape of the illuminated I-V curve, is expressed according to the following equation:

$$FF = \frac{V_{mp} J_{mp}}{V_{OC} J_{SC}} \qquad (1.1)$$

where V_{mp} represents the photo voltage and J_{mp} the photocurrent density at the maximum power point P_{max}. The conversion efficiency η of a solar cell is simply the ratio of the incoming power to the maximum power output $P_{max} = V_{mp} J_{mp}$ that can be extracted from the device.

$$\eta = \frac{V_{mp} J_{mp}}{P_{in}} \qquad (1.2)$$

Based on the above considerations, the band gap value is one of the most important properties of the absorber material of a solar cell. The optimum band gap value for the absorber material of a single-junction solar cell is about 1.5 eV, which results in a theoretical maximum efficiency of 30 % [3]. This is because V_{OC} and FF increase, and j_{sc} decreases with increasing band gap [2]. Even higher efficiencies can be achieved with tandem solar cell structures or by using solar radiation concentrators.

Most commercial solar cells of today are made of mono- or polycrystalline silicon. Silicon is a very abundant and well-known material of which a lot of experience has been gained over the decades - the first pn-junction solar cell based on crystalline silicon was made already in the 1950's [5]. Silicon photovoltaics owes a lot to the microelectronics industry that has gained the knowledge of the material properties as well as developed the manufacturing techniques. Additionally, rejects from microelectronics industry have served as a supply for high quality source material that has thus been available at a relatively low price [3, 6].

However, owing to its indirect band gap, silicon is not an ideal absorber material for solar cells. Semiconductor materials with indirect band gaps do not absorb light as efficiently as those with direct band gaps, and therefore a thick layer of material is needed to achieve sufficient light absorption. For example, 100μm of crystalline silicon is needed for 90 % light absorption in comparison with 1 μm of GaAs, which is a direct band gap semiconductor [6]. An inevitable result of such a large thickness is that the silicon used in solar cells must be of very high quality in order to allow for minority carrier lifetimes and diffusion lengths long enough so that recombination of the photogenerated charge carriers is minimized, and they are able to contribute to the photocurrent. These strict material requirements increase the production costs. Moreover, by the current production technologies, material losses during the fabrication of silicon solar cells are high.

The high production costs of crystalline silicon solar cells are compensated by their high efficiencies. Moreover since the 1950's, an important application of silicon solar cells has been as power sources in space vehicles where reliability and high efficiency are far more important issues than the cost. Also other expensive high-efficiency materials, such as GaAs and InP have been used in space applications. [7]

1.4 Thin film solar cells

Due to the limitations of crystalline silicon, other absorber materials have been studied extensively. These are semiconductors with direct band gaps and high absorption coefficients, and consequently they can be used in thin film form. Thin film solar cells have several advantages over crystalline silicon cells [6]. The consumption of materials is less because the thicknesses of the active layers are only a few micrometers. Therefore, impurities and crystalline imperfections can be tolerated to a much higher extent as compared to crystalline silicon. Thin films can be deposited by a variety of vacuum and non-vacuum methods on inexpensive substrates such as glass. Also curved and/or flexible substrates such as polymeric sheets can

be used, leading to lighter modules. Furthermore, composition gradients can be obtained in a more easily controllable manner.

The main candidates for low-cost thin film solar cell materials are amorphous hydrogenated silicon (a-Si:H), CdTe (cadmium telluride), $CuInSe_2$ and its alloys with Ga and/or S [8,9] and $CuInS_2$. Of these, amorphous silicon solar cells have currently the largest market share [10]. The absorption coefficient of amorphous silicon is higher than that of crystalline silicon, which enables its use in thin film form, and its band gap is closer to the ideal value of about 1.5 eV. A serious disadvantage is the light-induced degradation of solar cells made of this material, which leads to a drop of conversion efficiency from the initial value [3]. This Staebler-Wronski effect results from defects (dangling bonds) created by illumination that act as recombination centers. The stabilized efficiencies of amorphous silicon solar cells are quite low, about 13 % [9].

The polycrystalline compound semiconductor materials (CdTe and Cu $(In,Ga)(S,Se)_2$) do not suffer from light-induced degradation. In fact, the performances of CIS-based solar cells have even shown some improvement after illumination under normal operating conditions [11,12]. Another advantage is that they are direct band gap materials that have high absorption coefficients. The band gap of CdTe (1.4 eV) is very close to the ideal value. Despite that, the record efficiency for CdTe solar cells is only 16.5 % [13].

Thin film technology benefits from low material consumption and low price compared to crystalline silicon cells. The up scaling of this technology from the single solar cell to the large area module is straight forward since many cells can be interconnected from material deposited on one substrate in the form of stacked film layers. Compared to the crystalline material, thin film solar cells can be manufactured with less input of energy. This will shorten the energy pay back time, defined as the time it takes until the photo-generated energy output equals the energy that was consumed to produce the device. Specific advantages of the polycrystalline $CuInSe_2$ and its alloys

9

with Ga/S are their wide compositional tolerance and high optical absorption in the visible spectrum

1.5 Advantages of chalcopyrite thin films

Photovoltaic research has moved beyond the use of single crystalline materials such as Group IV elemental Si and Group III-V compounds like GaAs to much more complex compounds of the Group I-III-VI$_2$ with chalcopyrite structure. The ternary ABC$_2$ chalcopyrites (A = Cu; B = In, Ga or Al; C= S, Se or Te) form a large group of semiconducting materials with diverse structural and electrical properties. These materials are attractive for thin film photovoltaic application for a number of reasons.

The band gap of CuInSe$_2$ is relatively low, 1.04 eV, but it can be adjusted to better match the solar spectrum either by substituting part of In by Ga or part of Se by S. The flexibility of the material system allows in principle the band gap variation from 1.04 eV of CuInSe$_2$ via 1.53 eV of CuInS$_2$ and 1.68 eV of CuGaSe$_2$ (CGS) to 2.43 eV of CuGaS$_2$ [8]. The high flexibility in the optical properties of these materials is illustrated in figure 1.3. The band gap values of the different copper ternaries with chalcopyrite structure are given in table 1.1. The ternary Cu-chalcogenides crystallize in the tetragonal chalcopyrite structure. Sometimes, however, the cubic sphalerite phase, a disordered form of the chalcopyrite is observed. The Cu-chalcopyrites exhibit the highest efficiencies among thin film solar cells – the present record efficiency is 19.2 % for a device with a Cu(In,Ga)Se$_2$ (CIGS) absorber [14]. An additional advantage of the Cu-based absorber materials is that they do not have the acceptability problems associated with CdTe since these materials are less toxic [15]. Nevertheless, the Cd issue is somewhat shared also by the Cu(In,Ga)(Se,S)$_2$ technology because a CdS buffer layer is commonly used. The amount of Cd is, however, much less in the Cu(In,Ga)(Se,S)$_2$ cells than in the CdTe cells since the CdS layer is very thin.

One would expect that the higher band gap absorbers of the Cu(In,Ga)(S,Se)$_2$ system would result in devices with higher conversion

efficiencies, but this is not the case – conversion efficiencies achieved by $CuInS_2$ or $CuGaSe_2$ absorbers lag far behind those achieved by $Cu(In,Ga)Se_2$ or even $CuInSe_2$. This is partly due to the longer research history of $CuInSe_2$ and $Cu(In,Ga)Se_2$ solar cells and due to some fundamental differences between the low band gap ($CuInSe_2$ and $Cu(In,Ga)Se_2$ with a low Ga content) and wide band gap ($CuInS_2$ and $CuGaSe_2$) materials [16].
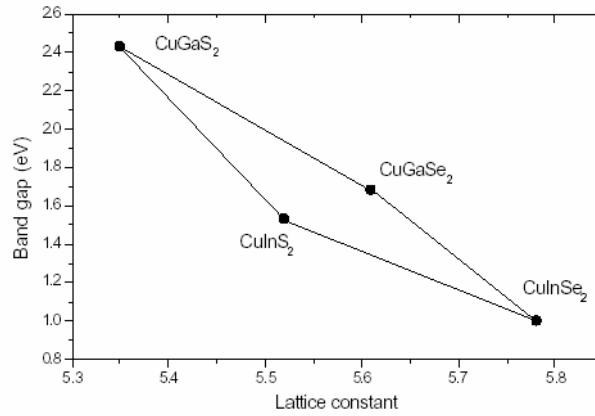
Fig. 1.3 Band gap versus lattice constant for various chalcopyrite semiconductors.

Table 1.1 Band gap values of the chalcopyrite Cu-ternaries

Ternary	Band gap (eV)
$CuInSe_2$	1.04
$CuGaSe_2$	1.68
$CuInS_2$	1.53
$CuGaS_2$	2.43
$CuAlSe_2$	2.67
$CuInTe_2$	0.96
$CuAlTe_2$	2.06
$CuGaTe_2$	1.23

$CuInSe_2$ has the highest optical absorption coefficient ($\alpha > 10^5$ cm^{-1}) of all known thin film materials (Fig. 1.4). This high value implies that 99% of the

incoming photons are absorbed within the first micrometer of the material. As a result, only 1–2µm of this material is enough to effectively absorb the incoming photons compared to bulk Si where at least 300µm of material is required.

The parameter that depends most strongly on the choice of semiconductor material is the band gap energy. The increase in the band gap will cause a decrease in the saturation current of the solar cell pn junction and as a result the open circuit voltage increases. Therefore a maximum in the efficiency exists. Figure 1.5 shows the predicted efficiencies as a function of band gap. It shows that the optimum band gap occurs between 1.4 and 1.6. The band gap value of the $CuInSe_2$ films can be tuned by alloying with Ga to obtain the optimum band gap needed for the high efficiency. $CuInS_2$ have a band gap of 1.53 eV is closely matching the requirements to yield high efficiency.
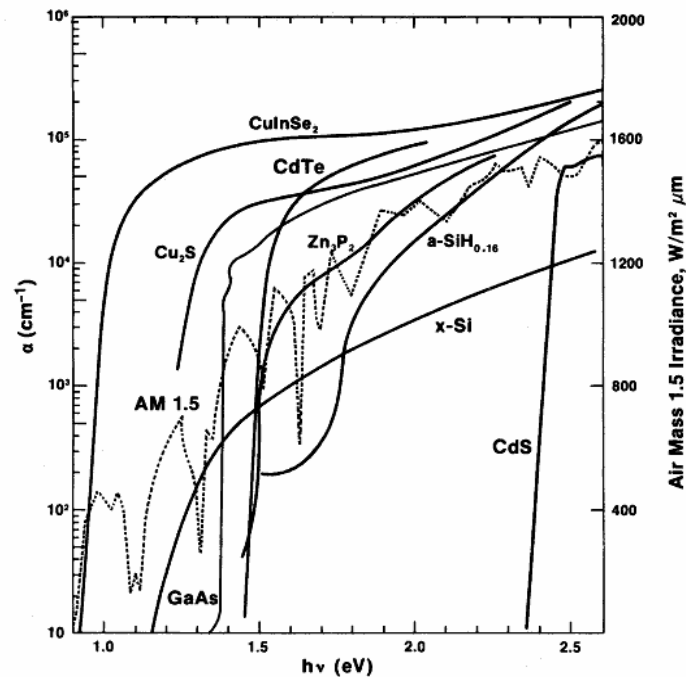
Fig. 1.4 Absorption spectrum of $CuInSe_2$ compared with the other photovoltaic semiconductors [17].
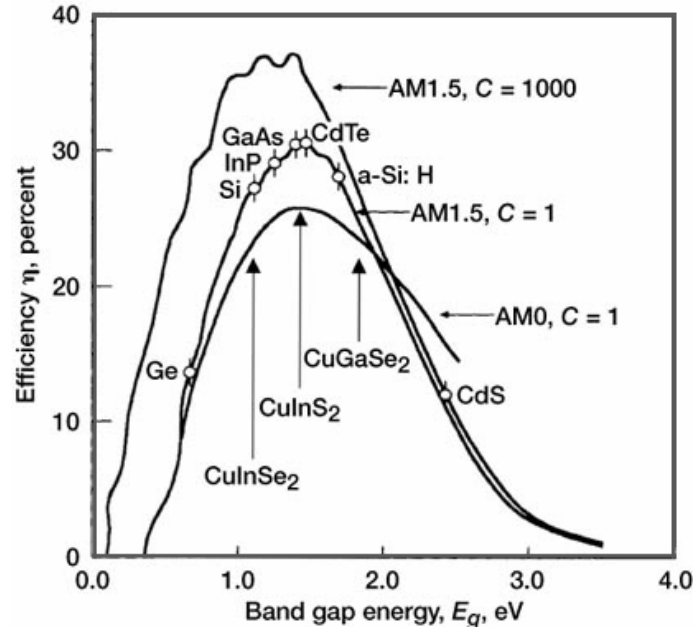
Fig 1.5 Ideal solar cell efficiency as a function of the band gap energy for the spectral distribution AM0 and AM1.5 with a power density of 1sun, and for AM1.5 with 1000sun [18].

Table 1.2 shows the highest efficiencies (η) produced by the thin film laboratory-scale solar cells of $CuInSe_2$ and its alloys. $CuInSe_2$ based solar cell devices have demonstrated good thermal, environment and electrical stability. Preliminary tests have indicated that the radiation tolerance of $CuInSe_2$ thin film is superior to that of single crystalline Si or GaAs devices when tested under high-energy electron and proton radiation [19].

Table 1.2 Reported performances of laboratory-scale solar cells based on $CuInSe_2$ and its alloys.

Device type	Area (cm^2)	% Efficiency (η)
$CuInSe_2/CdS/ZnO$	0.263	14.8
$Cu(In,Ga)Se_2/CdS/ZnO$	0.408	19.2
$CuGaSe_2/CdS/ZnO$	0.38	9.3
$CuInS_2/CdS/ZnO$	0.38	12

13

1.6 Solar cells based on CuInSe$_2$

1.6.1 Device Structure

The basic device structure of any heterojunction solar cell consists of the following layers; substrate, window layer, active layer and the contacts to the external circuits.

Substrate or superstrate

This serves as the protective layer for the active materials of the solar cell. The most common substrate is glass, but metal foils and some flexible plastic substrates may also serve the same purpose.

Window layer or buffer layer

It is a thin layer of a compound semiconductor, whose primary role is to couple the light optically into the next layer, the absorber, with minimal reflection losses. This layer also constitutes the first half of the p-n junction. Since the role of this window layer is not to absorb photons, it can be heavily doped (usually to n-type), which reduces the overall series resistance of the cell.

Absorber layer

This is the region where light is absorbed and the photocurrent is initiated. The band gap of the absorber should thus be suitable for the absorption of photons. The absorber is usually 100 times thicker than the window layer, and of p-type conductivity.

The contacts

This serves as the link to the external circuit. Usually the transparent conducting oxides and the metal coatings on both sides of the active materials acts as the contact grids.

Cells can be classified into two different categories according to how sunlight enters the cell: front wall and back wall configurations.

1.6.1.1 Substrate or back wall configuration

In this mode of solar cell, light enters from the opposite side of the substrate, hitting the front contact transparent conducting layer first. Figure 1.6a shows

a schematic representation of a CIS solar cell in the back wall configuration. Cell preparation starts by the deposition of the Mo back contact on glass, followed by the p-type CIS absorber, CdS or other weakly n-type buffer layer, undoped ZnO, n-type transparent conductor (usually doped ZnO or In_2O_3), metal grids for the contacts. Finally, the device is encapsulated to protect it against surroundings.

The structure of a CIS cell is quite complex since it contains several compounds as stacked films that may react with each other. Fortunately, all detrimental interface reactions are either thermodynamically or kinetically inhibited at ambient temperatures. The formation of a thin p-type $MoSe_2$ layer between the Mo and the absorber that occurs during the absorber preparation at sufficiently high temperatures [20, 21] is beneficial for the cell performance for several reasons: first, it forms a proper ohmic back contact. The Mo/CIS contact without the $MoSe_2$ layer is not an ohmic but a Schottky type contact which causes resistive losses [20,22]. Another advantage is the improved adhesion of the absorber to the Mo back contact. Further, since the band gap of $MoSe_2$ is wider (about 1.4 eV) [20] than that of a typical CIS absorber, it forms a back surface field for the photogenerated electrons [20,23,24], providing simultaneously a low-resistivity contact for holes [23]. The back surface field reduces recombination at the back contact since the insertion of a wider band gap layer (of the same conductivity type as the absorber) between the back contact and the absorber creates a potential barrier that confines minority carriers in the absorber [25]. Finally, the $MoSe_2$ layer prevents further reactions between CIS and Mo [21].

A moderate interdiffusion of CdS and CIS, that occurs to some extent in photovoltaic-quality material too [26,27], is potentially beneficial to the cell performance [21]. Further, the reaction of CdS with CIS to form Cu_2S is inhibited as long as photovoltaic quality (Cu-deficient) material is used. Similar stability is not present at a CIS/ZnO interface since Cu-poor CIS may react with ZnO to form ZnSe and In_2O_3 [21]. This, in addition to the sputter induced damage during ZnO deposition may contribute to the lower efficiencies of buffer-free devices [21].

15
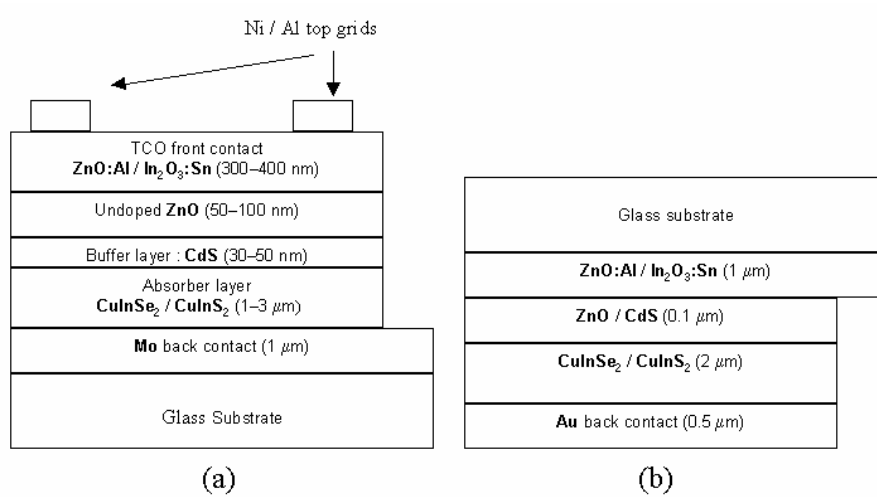
Fig.1.6. Schematic CIS solar cell structure:(a) substrate configuration (b) superstrate configuration

1.6.1.2 Superstrate or front wall configuration

Here the light enters the cell through the glass. A schematic superstrate solar cell structure is shown in figure 1.6b. The back contact in the diagram shown is a thin gold layer. Such a luxurious choice of back contact will of course not be economical in large-scale productions, and several alternatives such as graphite are often used.

The preparation of this so-called superstrate cell starts with the deposition of the transparent conductor, followed by the absorber deposition. The CdS layer is usually omitted in modern superstrate cells because the high absorber deposition temperatures would cause its intermixing with the CIS layer [28,29]. The advantages of the inverted configuration include lower cost, easier encapsulation and the possible integration as the top cell in future tandem cells [28]. The conversion efficiencies achieved by superstrate cells are, so far much lower than those of the substrate cells.

1.6.2 Stability and defect chemistry of CIS

In addition to the conversion efficiency, another crucial issue of a solar cell is its stability since it affects directly the cost of the electricity produced, and thus the energy payback time. Despite the complex solid state chemistry of the CIS solar cell structure, they have shown exceptionally stable performances both under normal operating conditions [11,12] as well as under harsh conditions such as irradiation by X-rays [30], electrons [31–33], or protons [32,34,35]. Radiation hardness demonstrates the suitability of CIS based cells to space applications.

Besides the interfacial stability discussed above, the most important factors that contribute to the electrical and chemical stability of the CIS-based solar cells are the unique properties of the absorber material, especially the wide single-phase domain and the fact that the doping level remains non-degenerate (below 10^{18} cm^{-3}) over a wide composition range. Both of these effects result from the strong self-compensation of the chalcopyrite compounds: defects that are caused by deviations from the stoichiometry are compensated by new defects that neutralize them, i.e., formation energies of the compensating ionic defects are low. As a result, most of the defects or defect complexes are electrically inactive with respect to the carrier recombination [21].

According to Zhang et al. [36], the formation energies of defects and defect complexes in CuInSe$_2$ are low. The energetically most favoured isolated point defect is the shallow copper vacancy V_{Cu} that contributes to the very efficient p-type doping ability of CIS. The most favorable defect complex is $(2V_{Cu} + In_{Cu})$ that prevents degenerate doping in In-rich material. Because of the high concentration of $(2V_{Cu} + In_{Cu})$ complexes, they interact with each other, which lowers the formation energies further. The existence of the ordered defect compounds (ODC) CuIn$_3$Se$_5$, CuIn$_5$Se$_8$ etc. may be explained as periodically repeating $(2V_{Cu} + In_{Cu})$ units. Other defects may be present too but their formation energies are higher [36].

17

CIS solar cells exhibit electrical metastabilities that are manifested as the increase of the open circuit voltage and improvement of fill factor upon illumination, and the effect of reverse biasing the junction. Illumination-induced metastabilities may occur both in the absorber and at the CIS/CdS interface, depending on the wavelength of illumination [21,37]. Effects caused by long-wavelength (red) illumination are related to the CIS absorber since red light (low energies) is mostly absorbed in CIS. Red illumination causes a metastable increase of net carrier concentration, which decreases the width of the space charge layer. The open circuit voltage increases due to the reduced recombination in the narrower space charge layer [37]. Thus the increase of the open circuit voltage upon illumination is related to the CIS absorber [21,37].

Short-wavelength illumination (blue light), in turn, affects mostly the regions at or near the CdS/CIS interface. Blue light is to a great extent absorbed into the buffer layer, and the photogenerated holes are injected into the near-surface region of the CIS absorber [37]. Illumination by blue light has been reported to improve the fill factor, which probably results from the ionization of deep donors in CdS. The positively charged fixed donors cause downward band bending in the CdS and reduce the barrier height to electrons [21,38]. The photogenerated holes have also been suggested to neutralize the negative defect states that are present on the CIS surface [37]. The improvement of the FF upon illumination is therefore related to the CIS/CdS interface.

Radiation hardness has also been suggested to be due to the self-repair of the radiation induced damages rather than due to the resistance of the material to damage. The self-healing mechanism is a result of the mobility of Cu and reactions involving Cu-related defects or defect complexes [39]. Thus the electrical stability of the CIS material system seems to be of dynamic nature rather than static. The material is not resistant to changes but it is flexible because of inherent self-healing mechanisms. Particularly, the mobility of Cu, as well as the high defect density of CIS, are actually advantages in CIS since they help in repairing damages, thus contributing to the unusual

impurity tolerance and to the radiation hardness. Also the Cu-poor surface composition of photovoltaic-quality CIS films has been proposed to result from the migration of Cu in the electric field of the space charge region [21]. The wide range of possible preparation techniques and preparation conditions for Cu-chalcopyrites has been suggested to be an indication of a stable energetic minimum that can be reached via different routes [39].

1.6.3 Effect of sodium and oxygen

Yet another interesting feature is the beneficial effect of sodium on the structural and electrical properties of Cu-chalcopyrite thin films. The phenomenon was discovered in 1993 [40,41] when solar cells prepared on soda lime glass substrates showed considerably higher efficiencies than those prepared on borosilicate glass. X-ray photoelectron spectroscopy and secondary ion mass spectrometry studies revealed the presence of Na at relatively high concentrations both on the surface and in the bulk of the CIGS films deposited on Mo/soda lime glass [40]. Sodium is normally detrimental to semiconductors but its presence during the growth of CIS-based films has been reported to increase the grain size [40–43], smoothen the surface morphology [42,43], enhance the crystallinity, results in a higher (112) preferred orientation [40–45], and increase the p-type conductivity (carrier concentration) [44–48]. Sodium has been suggested to aid the formation of the beneficial $MoSe_2$ layer between Mo and CIS [20]. As a result, improved solar cell efficiencies have been obtained due to the presence of Na [42–47].

Sodium thus affects both the growth and the doping of Cu-chalcopyrite films. Na^+ ions migrate from the substrate to the CIS film along grain boundaries [49], and their incorporation into a CIS film occurs via interaction with Se [49,50]. The Na contents in the CIS films are quite high, typically about 0.1 at. % or higher [44,48,49,51,52]. According to Granata et al. [48], the ideal Na content in CIS and CIGS films is between 0.05 and 0.5 at.%. Most of the sodium is located at the film surface, near the Mo back contact, or at the grain boundaries [43,45,47–50,53]. The increased p-type

conductivity of Na-containing Cu-chalcopyrite films is generally attributed to the suppression of donor-type defects such as In_{Cu} [45,46,54,55] that act as majority carrier traps. On the other hand, the removal of a minority-carrier trap state has also been reported [46].

The possible concentration of In_{Cu} in photovoltaic-quality CIS films is high. Sodium eliminates the In_{Cu}-related donor states or inhibits their formation by incorporating at the Cu site which results in an increased hole concentration [45,52]. The calculations of Wei et al. [55] supports the conclusion that the main effect of sodium on the electronic properties of CIS is to reduce the amount of intrinsic donor defects. When present at low concentrations, Na eliminates first the In_{Cu} defects, which results in a higher p-type conductivity [55]. This removal of In_{Cu} antisites may lead to a more ordered structure, which may also explain the enhanced (112) orientation [45].

In most cases, the diffusion of Na into the absorber film from the soda lime glass through the Mo back contact at high deposition temperatures is considered to provide a sufficiently high Na concentration, but deliberate incorporation of Na by introducing Na-containing precursors such as NaF [42,43,46], Na_2S [53,54], Na_2Se [47,56], Na_xO [57], $NaHCO_3$ [56] or elemental Na [44], has also been studied. The advantage of this approach is the possibility of a better control over the sodium content and thus a better reproducibility since the Na supply from the glass depends on the absorber deposition process as well as on the properties of the Mo back contact [42,56] and the glass itself. Thus, the amount of Na diffusing from the substrate is difficult to estimate accurately. Moreover, since the diffusion of Na from the substrate slows down at low temperatures, the deliberate addition of Na allows one to use lower deposition temperatures without so much degradation of the cell efficiency [43,44].

In addition to the effects discussed above, Na also enhances the influence of oxygen in the CIS based films [57–60]. The main role of oxygen is the passivation of positively charged Se vacancies (V_{Se}) that are present on the surfaces and grain boundaries of the Cu-chalcopyrite thin films [55,59,60].

The presence of Se vacancies at grain boundaries is especially detrimental since they decrease the effective p-type doping of the film. Additionally, they act as recombination centers for the photogenerated electrons [58–61]. The passivation of Se vacancies is therefore of significant importance to the performance of the solar cell [58–60]. Air annealing has in fact been used routinely to improve the photovoltaic properties of the CIGS solar cells [51]. Physisorbed oxygen that is present on the surfaces and grain boundaries of oxygen-exposed CIGS films, chemisorbs as O^{2-} which occupies the positively charged vacant Se sites, and thus obviates their disadvantageous effects. Sodium has been suggested to promote the formation of chemisorbed O^{2-} ions by weakening the O-O bond [55,57,58]. The correlated concentration distributions of these two elements in air-exposed CIGS films [45,47,49,53, 57] support this idea.

1.7 Present study

Chalcopyrite based heterojunction solar cells have specific advantage over the other solar cells. In this thesis work cost effective techniques are employed for the preparation of different thin film materials suitable for fabricating a heterojunction solar cell. Low cost chemical bath deposition (CBD) technique was used to deposit CdS buffer layer with high transparency and low resistivity. Wide band gap (ZnCd)S buffer layers were also prepared by CBD and the resistivity of these films were reduced by doping indium. A cadmium free wide band gap buffer layer, ZnS was also prepared and its advantages are compared with the electron beam evaporated ZnS films. $CuInSe_2$ and $CuInS_2$ thin films have been prepared by flash evaporation and two-stage process. Two stage process has been optimised for producing single phase, p-type $CuInS_2$ thin films. Indium tin oxide thin films have been prepared by rf magnetron sputtering so as to use it as the transparent conducting contact for the solar cell.

References

[1] Donald W. Aitken, Transitioning to a renewable energy future, White paper by International Solar Energy Society (Germany, 2003)

[2] J. L. Stone, Phys. Today, (September 1993) 22.

[3] A. Shah, P. Torres, R. Tscharner, N. Wyrsch and H. Keppner, Science 285 (1999) 692

[4] Solar Cells and Their Applications, (Eds) L.D. Partain, (John Wiley & Sons Inc., N.Y., 1995) p600

[5] D.M.Chapin, C.S.Fuller and G.L. Pearson, J. Appl. Phys. 25 (1954) 676

[6] A. Goetzberger and C.Hebling, Sol.Energy Mater. Sol.Cells 62 (2000) 1

[7] H. Tsubomura and H. Kobayashi, Crit. Rev. Solid State Mater. Sci. 18 (1993) 261

[8] R.W. Birkmire, Sol. Energy Mater. Sol. Cells 65 (2001) 17

[9] A. Goetzberger, J.Luther and G.Willeke, Sol. Energy Mater. Sol. Cells 74 (2002)1

[10] A.S. Bahaj, Renew. Energy 27 (2002) 97

[11] H.-W. Schock and R. Noufi , Prog. Photovolt.: Res. Appl. 8 (2000) 151

[12] T. Kojima, T. Koyanagi, K. Nakamura, T. Yanagisawa, K. Takahisa, M. Nishitani and T. Wada, Sol. Energy Mater. Sol. Cells 50 (1998) 87

[13] X. Wu, J.C. Keane, R.G. Dhere, C. DeHart, A. Duda, T.A. Gessert, S. Asher, D.H. Levi, P. Sheldon, in: Proceedings of the 17th Eur. Photovolt. Sol. Energy Conf. (Munich, 2001) p995

[14] K. Ramanathan K, M.A. Contreras, C.L. Perkins, S. Asher, F.S. Hasoon, J. Keane, D. Young, M. Roberto, W. Metzger, R. Noufi, J. Ward, A. Duda, Prog. Photovolt: Res. Appl., 11 (2003) 225

[15] V.M. Fthenakis, S.C. Morris, P.D. Moskowitz, and D.L. Morgan, Prog. Photovolt.: Res. Appl. 7 (1999) 489

[16] S. Siebentritt, Thin Solid Films, 403-404 (2002) 1

[17] J. E. Jaffe, A. Zunger, Phys. Rev B 29 (1984) 1882.

[18] S.M. Sze, Physics of Semiconductor Devices (Wiley & Sons, New York, 1981) p790

[19] R. A. Mickelsen et al., in: Proc. 18th IEEE Photovolt. Spec. Conf. (Kissimime, 1985) p1069.

[20] T. Wada, N. Kohara, S. Nishiwaki and T. Negami, Thin Solid Films 387 (2001) 118

[21] J.F. Guillemoles, L. Kronik, D. Cahen, U. Rau, A. Jasenek and H.W. Schock, J. Phys. Chem. B 104 (2000) 4849

[22] D. Schmid, M. Ruckh and H.W. Schock, Sol. Energy Mater. Sol. Cells 41-42 (1996) 281

[23] H.W. Schock and U. Rau, Physica B 308-310 (2001) 1081

[24] J.-F. Guillemoles, P. Cowache, A. Lusson, K. Fezzaa, F. Boisivon, J. Vedel and D. Lincot, J. Appl. Phys. 79 (1996) 7293

[25] R.J. Schwartz and J.L. Gray, in: Proc. 21st IEEE Photovolt. Spec. Conf. (Kissimmee, FL,1990) p570

[26] C. Heske et al., Appl. Phys. Lett. 74 (1999) 1451

[27] T. Nakada, and A. Kunioka, Appl. Phys. Lett. 74 (1999) 2444

[28] T. Nakada, T. Kume, T. Mise andA. Kunioka, Jpn. J. Appl. Phys. 37 (1998) L499

[29] F.-J. Haug, D. Rudmann, G. Bilger, H. Zogg and A.N. Tiwari, Thin Solid Films 403-404 (2002) 293

[30] J. Tringe, J. Nocerino, R. Tallon, W. Kemp, W. Shafarman and D. Marvin, J. Appl. Phys. 91 (2002) 516

[31] A. Jasenek, U. Rau, K. Weinert, I.M. Kotschau, G. Hanna, G. Voorwinden, M. Powalla, H.W. Schock, and J.H. Werner, Thin Solid Films 387 (2001) 228

[32] A. Jasenek and U. Rau, J. Appl. Phys. 90 (2001) 650

[33] M. Yamaguchi, J. Appl. Phys. 78 (1995) 1476

[34] S. Kawakita, M. Imaizumi, M. Yamaguchi, K. Kushiya, T. Ohshima, H. Itoh and S. Matsuda, Jpn. J. Appl. Phys. Part 2, 41 (2002) L797

[35] A. Boden, D. Bräunig, J. Klaer, F.H. Karg, B. Hosselbarth and G.La Roche, in: Proc. 28th IEEE Photovolt. Spec. Conf. (Anchorage, AK, 2000) p1038

[36] S.B. Zhang, S.-H. Wei, A. Zunger and K. H. Yoshida, H., Phys. Rev. B 57 (1998) 9642

[37] P. Zabierowski, U.Rau and M. Igalson, Thin Solid Films 387 (2001) 147

[38] M. Kontges, R. Reineke-Koch, P. Nollet, J. Beier, R. Schäffler and J. Parisi, Thin Solid Films 403-404 (2002) 280

[39] J.-F. Guillemoles, U. Rau, L. Kronik, H.W. Schock, and D. Cahen, Adv. Mater. 11 (1999) 957

[40] J. Hedstram et al., in: Proc. 23rd IEEE Photovolt. Spec. Conf. (Louisville, KY, 1993) p364

[41] L. Stolt, J. Hedström, J. Kessler, M. Ruckh, K.-O. Velthaus and H..W. Schock, Appl. Phys. Lett. 62 (1993) 597

[42] K. Granath, M. Bodegard and L. Stolt, Sol. Energy Mater. Sol. Cells 60 (2000) 279

[43] M.Bodegard, K.Granath and L.Stolt, Thin Solid Films 361-362 (2000) 9

[44] M.Lammer, U. Klemm and M. Powalla, Thin Solid Films 387 (2001) 33

[45] M.A. Contreras, B. Egaas, P. Dippo, J.Webb, J.Granata, K.Ramanathan, S. Asher, A. Swartzlander and R. Noufi, in: Proc.26th IEEE Photovolt. Spec. Conf. (Anaheim, CA, 1997) p359

[46] B.M.Keyes, F. Hasoon, P. Dippo, A. Balcioglu and F. Abulfotuh, in: Proc. 26th IEEE Photovolt. Spec. Conf. (Anaheim, CA, 1997) p479

[47] T. Nakada, D. Iga, H. Ohbo and A. Kunioka, Jpn. J. Appl. Phys. 36 (1997) 732

[48] J.E. Granata, J.R. Sites, S. Asher and J. Matson, in: Proc. 26th IEEE Photovolt. Spec.Conf. (Anaheim, CA, 1997) p387.

[49] D. Braunger, D. Hariskos, G. Bilger, U. Rau and H.W. Schock, Thin Solid Films 361-362 (2000) 161

[50] C. Heske et al., Appl. Phys. Lett. 75 (1999) 2082.

[51] U.Rau and H.W.Schock, Appl.Phys.A:Mater.Sci.Process. 69 (1999) 131

[52] D.W. Niles, K. Ramanathan, F. Hasoon, R. Noufi, B.J. Tielsch and J.E. Fulghum, J. Vac. Sci. Technol. A 15 (1997) 3044

[53] A. Rockett et al., Thin Solid Films, 372 (2000) 212

[54] R. Kimura et al., Sol. Energy Mater. Sol. Cells 67 (2001) 289

[55] S.-H. Wei, S.B.Zhang, S.B and A. Zunger, J.Appl.Phys. 85 (1999) 7214

[56] A. Rockett et al., Sol. Energy Mater. Sol. Cells. 59 (1999) 255

[57] M. Ruckh, D. Scmid, M. Kaiser, R. Schäffler, T. Walter and H.W. Schock, in: Proc. 1st World Conf. Photovolt. Energy Conf. (Waikoloa, Hawai 1994) p156

[58] L. Kronik, D. Cahen and H.W. Schock, Adv. Mater. 10 (1998) 31

[59] D. Cahen, and R. Noufi, Appl. Phys. Lett. 54 (1989) 558

[60] L. Kronik, U. Rau, J.-F. Guillemoles, D. Braunger, H.W. Schock and D. Cahen, Thin Solid Films 361-362 (2000) 353

[61] U. Rau, D. Braunger, R. Herberholz, H.W. Schock, J.-F. Guillemoles, L. Kronik and D. Cahen, J. Appl. Phys. 86 (1999) 497

CHAPTER 2

Thin film deposition techniques and characterisation tools

2.1 Introduction

Any solid or liquid object with one of its dimensions very much less than that of the other two may be called a 'thin film' [1]. Thin film devices would typically be about 5 to 50 μm thick in contrast to bulk devices, which are about 50 to 250 μm thick [2]. Again, it is not the thickness that is important in defining a film, but rather the way it is created with the consequential effects on its microstructure and properties. The microstructural features of the absorber layer sensitively influence the photovoltaic performance of a solar cell and in some cases, specific microstructures may be necessary to obtain the desired performance. A wide variety of microstructures and consequently properties can be obtained by simply varying the deposition conditions during the growth of the film. Thin film properties are strongly dependent on the methods of deposition, the substrate materials, the substrate temperature, the rate of deposition and the background pressure. The application and the properties of the given material determine the most suitable technique for the preparation of thin films of the material.

The different materials for the window layer, active layer and the transparent conducting electrodes for solar cells were prepared and characterised. Various deposition techniques were employed for the deposition of these materials in thin film form and the structural, optical and electrical properties of these films were studied using different characterisation tools. The various thin film deposition techniques and the characterisation methods employed are summarized in this chapter.

2.2 Thin film Preparation Techniques

Generally any thin film deposition follows the sequential steps: a source material is converted into the vapour form (atomic/molecular/ionic species) from the condensed phase (solid or liquid), which is transported to the substrate and then it is allowed to condense on the substrate surface to form the solid film [2]. Depending on how the atoms/molecules/ions/clusters of species are created for the condensation process, the deposition techniques

are broadly classified into two categories, viz. Physical methods and Chemical methods [2]. The general physical methods used in the work presented in this thesis are vacuum evaporation and sputtering. The vacuum evaporation techniques employed in the current work include, thermal evaporation by resistive heating, flash evaporation, and electron beam evaporation. All these physical methods of deposition of thin film were done in a high vacuum system in which a vacuum of 10^{-5} mbar was created using a diffusion pump backed by a rotary pump. RF magnetron sputtering was used for the preparation of transparent conducting oxide (tin doped indium oxide) thin films. Chemical bath deposition was effectively used to deposit certain II-VI chalcogenides (CdS and ZnS) semiconductors. Other special technique used in this work is the two stage processes, which involve the preparation of the precursor employing thermal evaporation followed by the sulphurisation. The following sections discuss the methodology and experimental set-ups used in various thin film depositions.

2.2.1 Thermal evaporation in vacuum by resistive heating

It is the most widely used technique for the preparation of thin films for the deposition of metals, alloys, and also many compounds, as it is very simple and convenient. Here the only requirement is to have a vacuum environment in which sufficient amount of heat is given to the evaporants to attain the vapour pressure necessary for the evaporation. The evaporated material is allowed to condense on a substrate kept at a suitable temperature.

When evaporation is made in vacuum, the evaporation temperature will be considerably lowered and the formation of the oxides and incorporation of impurities in the growing layer will be reduced. Evaporation is normally done at a pressure of 10^{-5} Torr. At this pressure a straight line path for most of the emitted vapour atoms is ensured for a substrate to source distance of nearly 10 to 50 cm [3]. The characteristics and quality of the deposited film will depend on the substrate temperature, rate of deposition, ambient pressure, etc. and the uniformity of the film depends on the geometry of the evaporation source and its distance from the source. The deposition by

thermal evaporation is simple, convenient and is widely used. Excellent and detailed reviews on the know-how of the thermal evaporation have been discussed by Holland [4].

Thermal evaporation evaporation has been used at various stages of the work. In the two-stage process for the preparation of CuInS$_2$ thin films, thermal evaporation was used to deposit In-Cu bilayers. Thin layer of vacuum evaporated indium or aluminium was used as electrodes in electrical measurements. Molybdenum boat was used as the evaporation source for the deposition of copper and indium, and tungsten coils were used for the deposition of aluminium.

2.2.2 Electron beam evaporation

In electron beam evaporation (EBE) a stream of electrons is accelerated through fields of typically 5–10kV and focussed onto the surface of the material for evaporation. The electrons lose their energy very rapidly upon striking the surfaces and the material melts at the surface and evaporates. That is, the surface is directly heated by impinging electrons, in contrast to conventional heating modes. Direct heating allows the evaporation of materials from water-cooled crucibles. Such water-cooled crucibles are necessary for evaporating reactive and in particular reactive refractory materials to avoid almost completely reactions with crucible walls. This allows the preparation of high purity films because crucible materials or their reaction products are practically excluded from evaporation [3,5].

Electron beam guns can be classified into thermionic and plasma electron categories. In the former type the electrons are generated thermionically from heated refractory metal filaments, rods or disks. In the latter type, the electron beams are extracted from plasma confined in a small space. We have used a thermionic system for the deposition of ZnS thin films. EBE was carried out in vacuum (2x10^{-5} mbar) using an electron beam gun of 6KW (make-Hind High Vacuum, Bangalore).

2.2.3 Flash evaporation

Flash evaporation is a technique for the deposition of films whose constituents have different vapour pressures. This method has the difficulty in controlling stoichiometry of the films due to the differences in the vapor pressure of the component elements [1,3]. In contrast to two-source evaporation, it does not require provisions to monitor the vapour density, nor is the control of the source temperature particularly critical. The objective of film-composition control is accomplished by evaporating to completion small quantities of the constituents in the desired ratio. Only one filament is used at a temperature sufficiently high to evaporate the less volatile material. The technique is applicable for the evaporation of alloys, metal-dielectric mixtures and compounds. In most cases, the vapours impinging on the substrate are highly supersaturated so that the film composition is not affected by condensation coefficients. Generally, the control of film composition is determined by how well the objective of complete evaporation of the source material is accomplished. For this purpose, several experimental techniques are available which are characterized by three criteria namely, the form in which the evaporant material is introduced, the mechanism used to dispense the evaporant and the type of flash filament employed. The greatest freedom in regard to the form of the evaporant material is when it is available in the powder form. Various powder dispensers are available, which have storage hoppers that differ in the powder release and transport mechanisms. The flash evaporation filament chosen depends on the nature of the evaporant material and it should be capable of attaining temperatures of typically 2000^0C without volatilization or heavy reaction with the evaporant.

A universal problem encountered in the flash evaporation of powders from flat filaments is incomplete evaporation due to particle ejection and deflection. Since the evaporant has a large surface-to-volume ratio but can usually not be degassed prior to evaporation, the sudden release of gases upon impact on the filament is often sufficient to expel particles. Another loss mechanism is the deflection of falling powder away from the filament

by the current of rising vapours. The latter effect is stronger at higher evaporation rates. Small particles are more strongly deflected than larger ones, which is the reason for using graded powders. In the evaporation of homogenous powders such as compounds or alloys, particle ejection and deflection affect only the economy of the process and the maintenance of the vacuum system. There is also a risk that particles may be thrown against the substrate surface. To avoid these difficulties, coarser powders and cylindrical or conical crucibles have been used in the evaporation of pervoskites and III-V compounds.

Flash evaporation has mostly been performed in poor vacuum of 10^{-5} to 10^{-4} Torr. This is attributable to the high gas content of the evaporant powder and outgassing from the surfaces surrounding the relatively large-area flash filament. The effect of the high background pressure on film properties may be inconsequential, especially in the case of oxide films. However, this is not so if strongly electropositive metals are deposited. The temperature of the substrates determines primarily the degree of order and crystallinity of the films.

Flash evaporation technique has been used for the deposition of the copper indium selenide thin films. The copper indium selenide powder with the desired composition ratio was prepared by the solid-state reaction of the constituent elements. The flash evaporation was carried out in a vacuum chamber at a base pressure of $2x10^{-5}$ mbarr. The powder was taken in a specially designed stainless steel crucible, which was connected to a vibrator. The speed of the vibrator was controlled externally. The $CuInSe_2$ powder coming out of the grove of the crucible was channelled to fall on to the hot molybdenum boat using a glass chute. The outgassing occurred during the flash evaporation resulted in the variation of vacuum in the range $2x10^{-5} – 5x10^{-5}$ mbar. The films were deposited on cleaned glass substrates, which were kept at 10 cm above the evaporation source. The deposition was carried out without any intentional heating of the substrate. The evaporation itself has raised the temperature of the substrate to around 100^0C. The thickness of the films during deposition was monitored using a digital

thickness monitor. The as deposited CuInSe$_2$ thin films were found to be selenium deficient and hence they were subjected to selenisation to compensate the loss of selenium in the film.

2.2.4 Sputtering

Sputtering is one of the most versatile techniques used for the deposition of transparent conductors when device quality films are required. Sputtering process produces films with higher purity and better controlled composition, provides films with greater adhesion and homogeneity and permits better control of film thickness. The sputtering process involves the creation of gas plasma usually an inert gas such as argon [6] by applying voltage between a cathode and anode. The cathode is used as a target holder and the anode is used as a substrate holder. Source material is subjected to intense bombardment by ions. By momentum transfer, particles are ejected from the surface of the cathode and they diffuse away from it, depositing a thin film onto a substrate. Sputtering is normally performed at a pressure of 10^{-2} –10^{-3} Torr.

Normally there are two modes of powering the sputtering system; dc and rf biasing. In dc sputtering system a direct voltage is applied between the cathode and the anode. This method is restricted for conducting targets only. RF sputtering is suitable for both conducting and non-conducting targets; a high frequency generator (13.56 MHz) is connected between the electrodes of the system. Magnetron sputtering is a process in which the sputtering source uses, magnetic field at the sputtering target surface. Magnetron sputtering is particularly useful when high deposition rates and low substrate temperatures are required [7].

Both reactive and non-reactive forms of dc, rf and magnetron sputtering have been employed for the deposition of compound semiconductors. In reactive sputtering, the reactive gas is introduced into the sputtering chamber along with argon to deposit oxide films. The deposition rates and properties of the films strongly depend on the sputtering conditions such as the partial

pressure of the reactive gas, the sputtering pressure, substrate temperature and spacing.
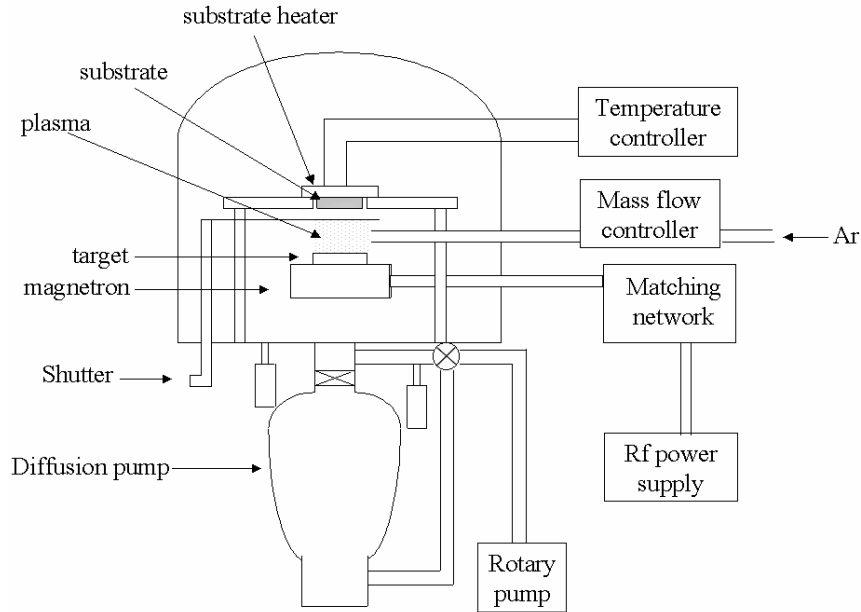
Fig 2.1 RF Sputter Deposition System

The process of RF sputter deposition is made possible due to the large difference in mass, and hence mobility, of electrons and inert gas ions. Because electrons are many times less massive than ions, electrons attain much greater velocities and travel much further than ions during each cycle of the applied rf voltage waveform. Since electrons travel much further, they eventually accumulate on the target, substrate and chamber walls such that the plasma is the most positive potential in the system. These induced negative voltages or "sheath voltages", cause acceleration of positive ions toward the negatively charged surfaces, which subsequently leads to sputtering events. The volume adjacent to a surface tends to be relatively free of electrons because of the negatively charged surface. This leads to a "dark space" because electrons are not available to excite gas atoms [8]. A schematic diagram of the rf sputtering system is shown in figure 2.1.

34

The target is selectively sputtered by controlling the relative surface areas of the target and the substrate holder. If space charge limited current is assumed, the ion current flux, J can be estimated by the Child- Langmuir equation [8],

$$J = \frac{KV^{3/2}}{D^2 m_{ion}} \qquad (2.1)$$

Where D is the dark space thickness, V is the sheath voltage, m_{ion} is the ionic mass and K is the proportionality constant. Since the positive ion current must be equal at both the electrodes,

$$\frac{A_A V_A}{D_A^2} = \frac{A_B V_B}{D_B^2} \qquad (2.2)$$

Where A_A and A_B are the surface areas of electrodes A and B respectively. It should be noted that this step differs from the assumption of treating the positive ion current densities equal. If the positive ion current densities were equal, there would be a much greater positive ion current flowing during one half cycle of the applied voltage waveform than the other due to the much greater area of the grounded substrate electrode. Therefore, because this system is assumed to be in steady state, the total positive ion current per half cycle should be the relevant quantity.

The glow discharge itself is a region where large quantities of positive and negative charge exist and can be modelled as a wire. Since most of the voltage in the glow discharge is dropped across the dark space, and they have small conductivities, they can be modelled as capacitors such that the capacitances,

$$C \propto A/D \qquad (2.3)$$

Furthermore, an AC voltage will divide across two series capacitors such that,

$$\frac{V_A}{V_B} = \frac{C_B}{C_A} \qquad (2.4)$$

From equations (2.1), (2.2) and (2.3),

$$\frac{V_A}{V_B} = \left(\frac{A_B}{A_A}\right)^2 \qquad (2.5)$$

This equation tells that smaller area will see larger sheath voltage, whereas larger area will see a smaller sheath voltage by a power of 2. The usefulness of this result is that $A_B > A_A$ must hold to selectively sputter the target. This is done in practice by grounding the substrate holder to the entire chamber resulting in a very large A_B. For this reason it is extremely important that the substrate holder and the system are well grounded to ensure that resputtering of the growing film does not occur.
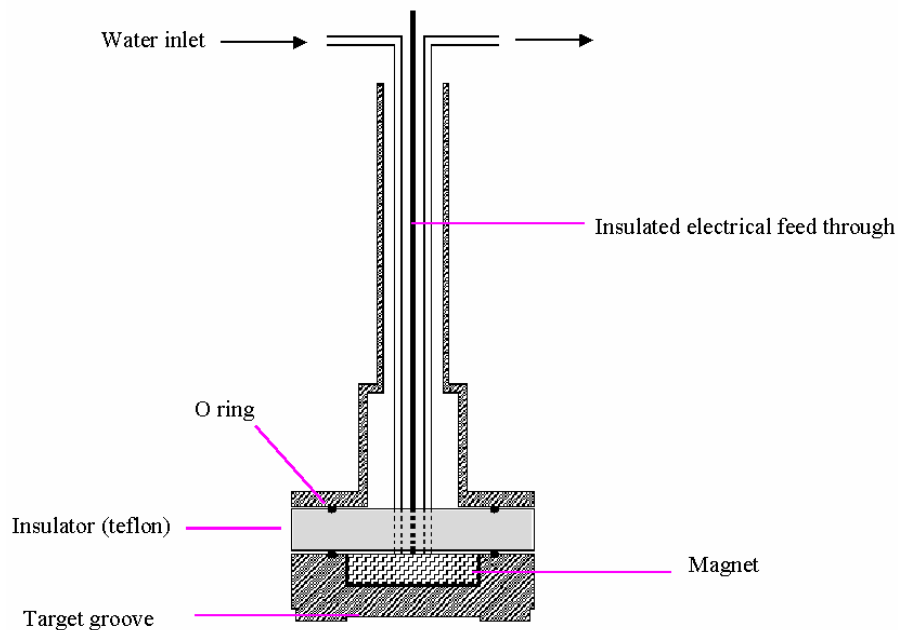
Fig 2.2 Schematic structure of the magnetron

We have used an in-house made magnetron for the rf sputtering of tin doped Indium oxide thin films. A magnet of 2000gauss was used to deflect the ions. A schematic diagram of the magnetron is shown in figure 2.2. The vacuum system consists of a six-inch diameter diffusion pump backed by a rotary pump (make – Indovision, Bangalore). The rf supply was connected to the magnetron through a capacitive matching network (make–Digilog

Instruments, Bangalore). The flow of argon gas into the vacuum chamber was controlled using a mass flow controller (make Bronkhorst, Holland).

2.2.5 Chemical bath deposition

Unlike the physical methods of preparation of thin films involving evaporation or ejection of material from a source, chemical methods of thin film deposition entail a definite chemical reaction. Chemical methods for film deposition in general use simpler equipment and are more economical than physical approaches. More over chemical methods do not require high vacuum and can be carried out at lower temperatures. CBD is a simple and low cost method that produces uniform, adherent and reproducible large area thin films for PV related applications [9].

In chemical bath deposition, a complexing agent is used to bind the metallic ions to avoid the homogeneous precipitation of the corresponding compound. Formation of complex ion is essential to control the rate of the reaction and to avoid the immediate precipitation of the compound in the solution. The metal complex hydrolyses slowly to generate the positive ions in the solution. The solution containing the metal complexes was mixed with the solution which produces the negative ion by hydrolyses. The deposition of the compound occurs when the ionic product exceeds the solubility product of the compound to be deposited. Either homogeneous or heterogeneous deposition can occur. The homogeneous process is the faster one resulting in the adsorption of powdery particles on the substrate due to the bulk precipitation. So, the formation of metal complexes is essential to minimize the homogeneous process. In the heterogeneous process, due to the slow release of the ions by the metal complexes, the preferential adsorption of the ions will take place leading to the uniform nucleation and growth of the thin film.
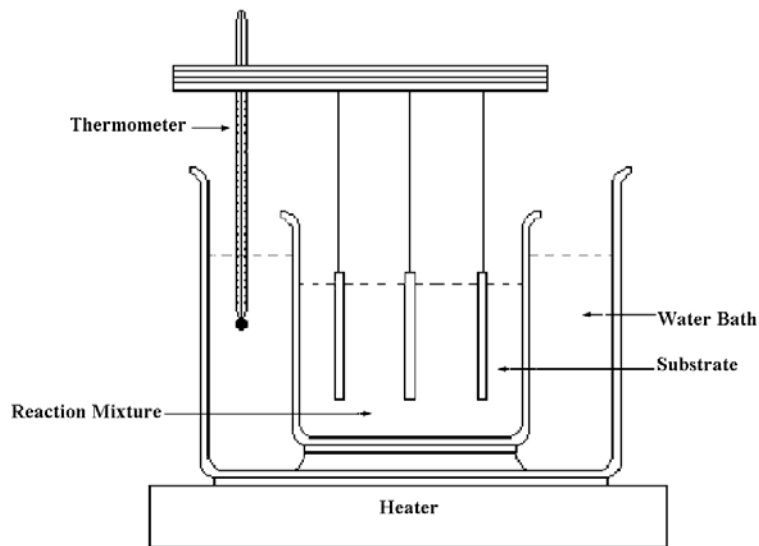
Fig.2.3 Set up for Chemical bath deposition

The main disadvantage of the chemical bath deposition is the wastage of the material due to the deposition on the walls of the container and precipitation into the solution. Preparation of the films with a definite geometric pattern on the substrate is difficult because perfect masking is not possible. The quality of the film deposited depends on the bath parameters like temperature, time of deposition, concentration of the reactants and the pH of the chemical bath. The experimental set up for the chemical bath deposition is shown in figure 2.3.

Although chemical bath deposition has been used as a technique for preparing films since 1960, utilization of CBD semiconductors in photovoltaic devices started only by 1990 by integrating CdS buffer layer over sputtered ZnO films [10]. A number of review articles discussing the status and applications of CBD have been appeared in the literature [9,11,12]. In this thesis work CdS, ZnS and their ternary derivative $Zn_xCd_{1-x}S$ thin films were deposited by the chemical bath deposition technique. Detail reaction mechanism during the chemical bath deposition and the role of the complexing agents are discussed in chapter 3.

2.2.6 Two stage process

Two stage processes is a simple method for the preparation of chalcogenide and selenide thin film [13]. This method has been effectively employed to produce high efficiency solar cells. The two stage processes consists of two steps; 1) Preparation of the precursor 2) chalcogenisation of the precursor. The precursor can be, evaporated or sputtered metallic layers or a metallic alloy formed by the annealing of metallic multilayers. We have used the two stage processes to prepare copper indium sulphide ($CuInS_2$) thin films. Here Copper and Indium layers are deposited on glass substrates by thermal evaporation. The Cu-In bi-layer is annealed in vacuum to form the copper indium alloy ($Cu_{11}In_9$). This alloy was sulphurised at various temperatures to form $CuInS_2$ thin films. Sulphurisation was carried out in a specially designed set up as shown in figure 2.4. The set up consists of a reaction vessel made of quarts, temperature controlled heater and the sulphurisation source. H_2S was used as the sulphurising agent, which was prepared using a Kipp's apparatus by the reaction between dilute hydrochloric acid and ferrous sulphide. The sulphurisation temperature was varied from 250^0C to 400^0C.
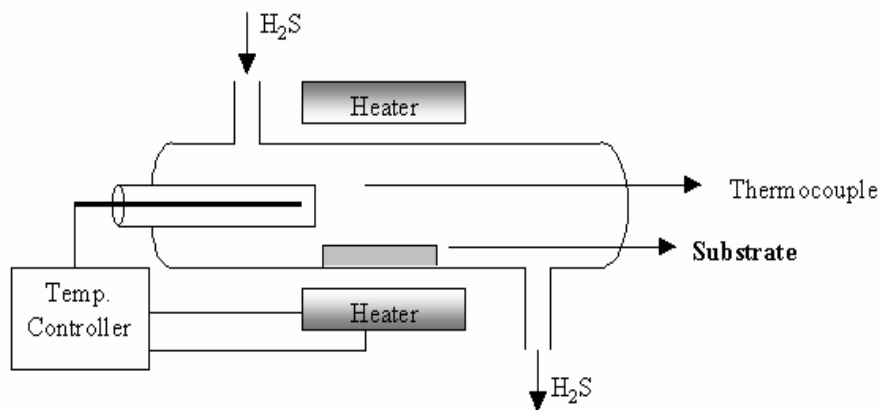
Fig 2.4 Sulphurisation set up for the preparation of $CuInS_2$

2.2.7 Selenisation set up

The flash evaporated CuInSe$_2$ thin films were found to be selenium deficient [13] and hence post deposition annealing in selenium was carried out to compensate the selenium loss. The set up used for the selenisation is as shown in figure 2.5.
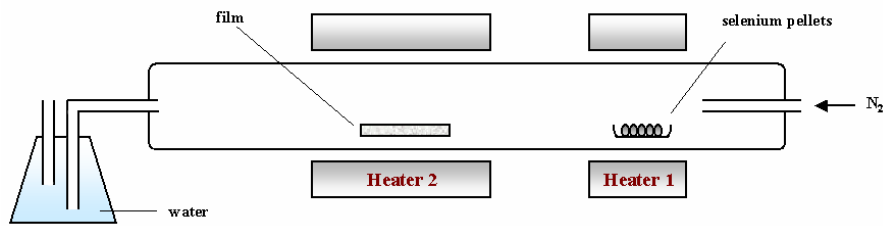
Fig. 2.5 Selenisation set up

Two heating zones are used for the selenisation as shown in the figure 2.5. The selenium pellets at the heating zone1 will be sublimated and the selenium vapours will be carried to the heating zone 2 by the nitrogen gas. The selenium vapour will react with the CuInSe$_2$ films, which is kept at a temperature of 400^0C resulting in a chalcopyrite CIS film.

2.3 Characterisation tools

The optimisation of the preparation conditions is the main task in order to get device quality films. This is to be done on the basis of detailed structural, compositional, morphological, optical and electrical properties of the films obtained at different growth conditions. In the following sections the techniques used for the film characterizations are discussed briefly.

2.3.1 Thin film thickness

Thickness plays an important role in the film properties unlike a bulk material. Reproducible properties are achieved only when the film thickness

and the deposition parameters are kept constant. Film thickness may be measured either by in-situ monitoring of the rate of deposition or after the film deposition.

Gravimetric method

The method depends on the increase of the weight (w) of a film due to its mass increase and from the knowledge of its density (ρ) and the deposit area (A) [2]. The film thickness *'t'* can be evaluated from the relation,

$$t = \frac{w}{\rho A}$$
(2.6)

The increase in weight *'w'* was measured using a microgram balance. This method was used for calculating the thickness of the chemical bath deposited ZnS films and the CuInS$_2$ films prepared by the two-stage process.

Quartz crystal monitor

This method was first investigated by Sauerbrey [14] independently and later modified by Lostis [15] and many others. In this in-situ method, thickness measurement depends on the oscillation of a quartz crystal when excited and the frequency of its oscillation depends on its thickness as given by the relation [2],

$$f = \frac{v}{2d} = \frac{N}{t}(nmkc / \sec)$$
(2.7)

where, v is the velocity of the transverse elastic waves normal to the crystal plate, d is the thickness of the crystal and N is the frequency constant depending on the nature of the crystal.

When a film of thickness t is deposited on the quartz plate, the mass of the crystal changes. The corresponding change in the frequency of the crystal can be utilised to find the average thickness of the film deposited.

$$t = \frac{\Delta f}{C\sigma}$$
(2.8)

where, σ is the density of the deposited film and $C = \frac{f^2}{N\rho}$ (ρ is the density

of the quarts crystal) is called the sensitivity for mass determination which is a constant of the crystal used. We have used a quartz thickness monitor

41

(Model C200) in which the changes in the resonant frequency of the quartz crystal oscillator with the film deposition is calibrated to give the deposition rate and the thickness of the film. The quartz thickness monitor was used during the flash evaporation of CuInSe$_2$ films, electron beam evaporation of ZnS and in the deposition of In and Cu layers in the two stage processes.

Optical interference method

Film thickness can be measured accurately from interference fringes using multiple beam interferometry. This technique was first used by Weiner [16] and later was modified by Tolansky [17]. Two reflecting surfaces are brought in close proximity such that a small wedge with a small air gap in between them is formed. If a monochromatic light falls at normal incidence on it, interference of light due to the multiple reflected beams results in a series of fringes (Fizeau). The distance between the fringes depends on the air gap as well as on the wavelength of the monochromatic light.

The film for thickness measurement is deposited on a flat surface so as to leave a sharp edge between the film and the uncoated region of the substrate. Over this film a highly reflecting coating of aluminium forms a sharp step on the film edge. Another optically flat glass slide known as the reference plate with a partially transparent aluminium film is then placed over the specimen with the metal coated surfaces in contact with each other so as to leave a small air gap at the step. A monochromatic parallel beam of light is then incident on this two plates assembly and reflected light is then observed through a microscope. A set of sharp fringes perpendicular to the step with equal displacements will be observed and the thickness (t) can be determined using the relation,

$$t = \frac{b\lambda}{2a} \tag{2.9}$$

where b is the displacement of the fringes at the step and a is the distance between consecutive fringes. The sharpness of the fringes depends on the reflectivity of the metal coating, the spread of the incident beam, air gap etc. This method was used for determining the film thickness of rf magnetron sputtered ITO films and chemical bath deposited CdS and Zn$_x$Cd$_{1-x}$S films.

2.3.2 Surface morphology

The uniformity and roughness of the thin film surface plays an important role in the optical properties of thin films. When the surface is rough, the films will be less transparent and the grain boundaries will affect the electrical properties of the thin films. The surface morphology of the films is studied using scanning electron microscopy (SEM) and atomic force microscopy (AFM).

Scanning electron microscopy (SEM) is one of the most widely used techniques for obtaining micro structural and surface features of thin films. An electron beam is focused onto the surface of the specimen and results in the ionization of the atoms in the specimen. This will cause the ejection of the secondary electrons from the surface, very close to the incident beam position. These secondary electrons can be attracted to a positively charged detector with high efficiency. The secondary electron yield per primary electron is high and increases as the angle between electron beam and the surface normal increases [18]. The secondary electrons generated from the specimens are used for Z-modulation in a corresponding raster on an oscilloscope. In order to avoid charging problems a thin layer of gold is deposited on the specimen without altering the surface features. The secondary electron mode is generally preferred for topographical feature determination since these electrons generate only from about $10A^0$ or less from the film surface and hence the picture obtained is a faithful reproduction of the surface features.

The scanning electron microscopy can be effectively used for the surface analysis to know the details regarding the grain size, presence of minor or secondary phases, the orientation of the grains, uniformity, porosity of the sample etc. SEM gives a pictorial overview of the grains on the thin film surface, whereas AFM is an effective tool to study the surface roughness and also the average cluster size on the thin film surface. AFMs can achieve a

resolution of 10 pm, and unlike electron microscopes, can image samples in air and under liquids.

2.3.3 Energy dispersive X-ray analysis (EDX)

EDX was used to estimate the composition of the thin film samples. X rays are generated by the incident electrons within a volume similar to but rather larger than that for the backscattered electrons. Peak X-ray energies corresponding to the characteristics of the elements within that volume can be identified and the relative compositions of elements can be estimated. Thus the bulk composition of the sample and of the individual grains in a polycrystalline sample can be determined [18].

2.3.4 X-ray diffraction studies

Electrical and optical properties of the materials are influenced by the crystallographic nature of the films. X-ray diffraction (XRD) studies were carried out to study the crystallograoghic properties of the thin films prepared.

A given substance always produces a characteristic X-ray diffraction pattern whether that substance is present in the pure state or as one constituent of a mixture of substances. This fact is the basis for the diffraction method of chemical analysis. The particular advantage of X-ray diffraction analysis is that it discloses the presence of a substance and not in terms of its constituent chemical elements. Diffraction analysis is useful whenever it is necessary to know the state of chemical combination of the elements involved or the particular phase in which they are present. Compared with ordinary chemical analysis the diffraction method has the advantage that it is much faster, requires only very small sample and is non destructive [19].

The basic law involved in the diffraction method of structural analysis is the Bragg's law. When monochromatic X-rays impinge upon the atoms in a crystal lattice, each atom acts as a source of scattering. The crystal lattice

acts as series of parallel reflecting planes. The intensity of the reflected beam at certain angles will be maximum when the path difference between two reflected waves from two different planes is an integral multiple of λ. This condition is called Bragg's law and is given by the relation,

$$2dSin\theta = n\lambda \qquad (2.10)$$

where n is the order of diffraction, λ is the wavelength of the X-rays, d is the spacing between consecutive parallel planes and θ is the glancing angle (or the complement of the angle of incidence)[20].

Xray diffraction studies gives a whole range of information about the crystal structure, orientation, average crystalline size and stress in the films. Experimentally obtained diffraction patterns of the sample are compared with the standard Powder Diffraction Files published by the International Centre for Diffraction Data (ICDD).

The average grain size of the film can be calculated using the Scherrer's formula [19],

$$d = \frac{0.9\lambda}{\beta Cos\theta} \qquad (2.11)$$

where, λ is the wavelength of the X-ray and β is the full width at half maximum intensity in radians.

The lattice parameter values for different crystallographic systems can be calculated from the following equations using the (hkl) parameters and the interplanar spacing d.

Cubic system, $\qquad \dfrac{1}{d^2} = \dfrac{h^2 + k^2 + l^2}{a^2}$ $\qquad (2.12)$

Tetragonal system, $\qquad \dfrac{1}{d^2} = \dfrac{h^2 + k^2}{a^2} + \dfrac{l^2}{c^2}$ $\qquad (2.13)$

Hexagonal system, $\qquad \dfrac{1}{d^2} = \dfrac{4}{3}\left(\dfrac{h^2 + hk + k^2}{a^2}\right) + \dfrac{l^2}{c^2}$ $\qquad (2.14)$

X-ray diffraction measurements of the different films were done using Rigaku automated X-ray diffractometer. The filtered copper Kα (λ=1.5418A^0) radiation was used for recording the diffraction pattern.

45

2.3.5 Optical characterisation

Determination of band gap energy

Intrinsic optical absorption of a single photon across the band gap is the dominant optical absorption process in a solar cell. When the energy of the incident photon ($h\nu$) is larger than the band gap energy the excitation of electrons from the valence band to the empty states of the conduction band occurs. The light passing through the material is then absorbed and the number of electron hole pairs generated depends on the number of incident photons $S_0(\nu)$ (per unit area, unit time and unit energy). The frequency ν is related to the wavelength λ by the relation, $\lambda = c/\nu$, where c is the velocity of light. The photon flux $S(x,\nu)$ decreases exponentially inside the crystal according to the relation [13],

$$S(x,\nu) = S_0(\nu)\, exp(-\alpha x) \tag{2.15}$$

where, the absorption coefficient, ($\alpha(\nu) = 4\pi k\nu/c$) is determined by the absorption process in semiconductors and k is the extinction coefficient.

According to Bardeen et al. [21] for the parabolic band structure, the relation between the absorption coefficient (α) and the band gap of the material is given by,

$$\alpha = \frac{A}{h\nu}\,(h\nu - E_g)^r \tag{2.16}$$

where, r=1/2 for allowed direct transitions, r=2 for allowed indirect transitions, r=3 for forbidden indirect transitions and r=3/2 for forbidden direct transitions. A is the parameter which depends on the transition probability. The absorption coefficient can be deduced from the absorption or transmission spectra using the relation,

$$I = I_0 e^{-\alpha t} \tag{2.17}$$

where, I is the transmitted intensity and I_0 is the incident intensity of the light and t is the thickness of the film. In the case of direct transition, from equation.2.16, $(\alpha h\nu)^2$ will show a linear dependence on the photon energy ($h\nu$). A plot of $(\alpha h\nu)^2$ against $h\nu$ will be a straight line and the intercept on energy axis at $(\alpha h\nu)^2$ equal to zero will give the band gap energy.

Determination of optical constants

The optical constants, the refractive index (n) and the extinction coefficient (k) of the films are calculated using the theory of Manificer et al. [22] for weakly absorbing films.

In the case of weakly absorbing films, the measurement of transmission of light through the film in the region of transparency gives the complex refractive index, n* = n – ik.

In the case of normal incidence and weak absorption, $k^2 << (n - n_0)^2$ and $k^2 << (n-n_1)^2$. If n_0, n and n_1 are the refractive indices of the substrate, film and the medium respectively, then the refractive index of the film is given by,

$$n = \left[N + \left(N^2 - n_0{}^2 n_1{}^2 \right)^{1/2} \right]^{1/2} \qquad (2.18)$$

where, $N = n_0{}^2 + n_1{}^2 + 2n_0 n_1 \dfrac{T_{max} - T_{min}}{T_{max} \, T_{min}}$ (2.19)

where, T_{max} and T_{min} are found out from the interference fringes of the transmission spectra by fitting envelops for the maximum and minimum values.

The extinction coefficient (k) can be calculated using the relation,

$$\alpha = 4\pi k/\lambda \qquad (2.20)$$

where, α is the absorption coefficient for the wavelength λ which can be found out from the transmission spectra.

2.3.6 Electrical characterisation

Resistivity by two probe method

The resistivity of the films is determined by the two-probe method with the electrodes in planar geometry. Evaporated indium layers or high conducting silver paste was used as the electrodes. The current voltage measurements were carried out using a Keithley`s source measure unit (Model SMU236). The resistivity (ρ) of the films is calculated applying ohm's law, by the relation ρ = RA/L. Where R is the resistance given by the slope of the

current- voltage characteristic curves. A is the area of the film in planar geometry which is given by the product of the film thickness and the width of the film. L is the spacing between the electrodes.

Hall measurement

The electrical resistivity of a semiconductor thin film can be written using Ohm's law,

$$\rho = \frac{1}{en\mu} \qquad (2.21)$$

where 'ρ' is the film resistivity, e is the electronic charge, n is the number of carriers corresponding to the carrier concentration and 'μ' is the carrier mobility. According to Ohm's law the carrier mobility affects resistivity. Low resistivity can be achieved by increasing the carrier concentration or mobility or both. Increasing carrier concentration is self-limiting because at some point the increased number of free carriers decreases the mobility of the film due to carrier scattering. Hence there is a trade off between the carrier density and carrier mobility for achieving low resistivity.

In the case of Indium tin oxide films, the resistivity (ρ), carrier concentration (n), carrier mobility (μ), and sheet resistance were measured using Vander Pauw four point probe in geometry [23]. Samples used were 1cm x 1cm in size. The ohmic contacts were made using silver paste. The silver paste was applied at the corners of the sample symmetrically as shown.
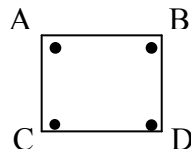
Let R_1 be the potential difference between A and B per unit current through C and D or vice versa. Similarly R_2 the potential difference between B and C per unit current through D and A.
Then sheet resistance R_s can be calculated using the relation

$$R_s = \left(\frac{\pi}{\ln 2}\right)\left(\frac{R_1 + R_2}{2}\right)f\left(\frac{R_1}{R_2}\right) \tag{2.22}$$

where $f\left(\dfrac{R_1}{R_2}\right)$ is the Vander Pauw function and is given by the relation,

$$f\left(\frac{R_1}{R_2}\right) = 1 - 0.3466\left(\frac{R_1 - R_2}{R_1 + R_2}\right)^2 \tag{2.23}$$

The Hall signal was measured between two ends while passing the current through the other two ends. Hall mobility is,

$$\mu = \Delta R \times \frac{10^8}{BR_s} \tag{2.24}$$

where ΔR is the change in resistance due to magnetic field (B) which was applied to measure Hall voltage. Carrier concentration was determined using the equation 2.21. The hall coefficient R_H is given by,

$$R_H = \mu \, x \, \rho \tag{2.25}$$

The type of carriers can be understood from the sign of the R_H. The negative values of R_H correspond to the electrons (n-type) carriers and positive values to holes (p-type).

Nature of conductivity

Thermo power measurement is a useful technique for the evaluation of the type of carriers responsible for the conduction. Thermo power measurements were carried out using a modified set up [24] which is similar to the one designed by D.L. Young et al.[25]. The slope of the thermoemf versus ΔT curve gives the Seebeck coefficient. A positive Seebeck coefficient is obtained when the majority carriers are holes and a negative Seebeck coefficient for electrons.

References

[1] Leon I. Maissel and Reinhard Glang, Handbook of Thinfilm technology (1983) Mc Graw Hill Book Company.

[2] A.Goswami, Thin Film Fundamentals. New Age International (P) Limited, New Delhi, 1996

[3] K.L. Chopra, Thin Film Phenomena, Robert E. Krieger Publishing Co. Inc., New York, 1979

[4] L. Holland, Vacuum Deposition of Thin films, John Wiley & Sons Inc., New York, 1956

[5] J.George, Preparation of thin films, Marcel Dekker Inc.,NewYork, 1992

[6] B. Chapman and S. Mangano, Thin-film deposition processes and techniques

[7] F.L.Akkad, A.Punnose, J.Prabu, J.Appl.Phys A 71(2000) 157

[8] B.Chapman, Glow Discharge Processes, New York, John Wiley & Sons, 1980

[9] R.S. Mane and C.D. Lokhande, Mater. Chem. Phys. 65 (2000) 1

[10] J. Herrero, M.T. Gutierrez, C.Guillen, J.M. Dona, M.A. Martinez, A.M. Chapparo and R.Bayon, Thin Solid Films 361-362 (2000) 28

[11] P.K.Nair, M.T.S. Nair, A.Fernandez, M.Ocapo, J.Phys.D, 33 (1989) 829

[12] C.D. Lokhande, Mater. Chem. Phys. 27 (1991) 1

[13] H.J. Moller, Semiconductors for solar cells, Rtech. House Inc., London 1993

[14] G.Sauerbrey, Z.Physik 155 (1959) 206

[15] P.Lostis, Rev. Opt. 38 (1959) 1

[16] O.Weiner, Wied.Ann. 31(1887) 629

[17] S. Tolansky, Multiple Beam Interferometry of Surfaces and Thin films, Oxford University Press, Fair Lawn, NJ, 1948

[18] D.J.O'Connor, B.A. Sexton, R.St.C.Smart (Eds), Surface Analysis Methods in Material Science, Springer-Verlag, Berlin-Heidelberg 1992

[19] B.D. Cullity and S.R. Stock, Elements of X ray diffraction, Third edition, (New Jersey, Prentice Hall, 2001)

[20] Charles Kittel, Introduction to Solid State Physics, Seventh edn (Wiley Eastern Limited, 1996)

[21] J.Bardeen, F.J.Blatt and L.H. Hall, in: Proceedings of Photoconductivity Conf. (1954,Atlantic City), (Eds) R.Breckenridze, B.Russel and T.Hahn, (J.Wiley and Chapman and Hall, New York, 1956) p146

[22] J.C. Manifacier, J. Gasiot, J.P. Fallard, J. Phys. E 9 (1976) 1002

[23] Manual, Model H 50 MMR technologies Inc. California

[24] R.Manoj, P. Pramodan, J. Isaac and M. K. Jayaraj, Proceedings of the DAE Solid State Physics Symposium, India, 2003 (in press)

[25] D.L.Young, T.J.Coutts, V.I. Kaydanov, Rev. Sci. Instruments 71 (2000) 462

CHAPTER 3

Chemical bath deposition of II-VI semiconductor thin films for buffer layer application in solar cells

Part A

Preparation and characterisation of CdS thin films by chemical bath deposition

Cadmium sulphide thin films on glass and ITO coated glass substrates were prepared by the chemical bath deposition technique. The band gap of the as deposited films varied in the range 2.43 eV to 2.67 eV. The as deposited films were smooth and uniform with a carrier concentration of 1.97×10^{17} carriers/cm^3. These films have low resistivity (~10^2 Ωcm) and high transparency (>80%) in the visible region.

3A.1 Introduction

Over the years cadmium sulphide thin films have been extensively investigated as an n-type buffer layer to form thin film heterojunction solar cells with p-CdTe and p-CuInSe$_2$ absorber layers. Most of the high-efficiency CIS based solar cells of today have a thin (50 nm or less) CdS buffer layer and an undoped ZnO layer between the absorber and the transparent conducting oxide (see Chapter 1, Fig 1.6). The role of CdS and undoped ZnO are related to some extent [1]. Although the open circuit voltages of high-efficiency CIS devices are mostly determined by the electronic quality of the bulk absorber material [2,3], the cell performances are nevertheless heavily influenced by the formation of the ZnO/CdS/CIS heterojunction [1]. The role of the buffer layer is twofold: it affects the electrical properties of the junction and protects it from chemical reactions and mechanical damage. From the electronic point of view, the CdS layer optimizes the band alignment of the device [4,5] and builds a sufficiently wide depletion width that minimizes tunneling and establishes a higher contact potential that allows higher open circuit voltage [5]. The buffer layer plays also a very important role as a "mechanical buffer" since it protects the junction electronically and mechanically against the damage that may otherwise be induced by the oxide deposition. Moreover, in large-area devices the electronic quality of the CIS film is not necessarily the same over the entire area, and recombination may be enhanced at grain boundaries or by local shunts. Together with the undoped ZnO layer, CdS enables self-limitation of electrical losses by preventing electrical inhomogeneities from dominating the open circuit voltage of the entire device [1].

3A.2 Cadmium sulphide buffer layer

A variety of techniques are being used to deposit CdS thin films, such as; molecular beam epitaxy (MBE) [6], metal organic chemical vapour deposition (MOCVD) [7], close spaced sublimation (CSS) [8,9], screen printing [10,11] physical vapour deposition [12,13], rf sputtering [14],

pulsed laser ablation [15], spray pyrolysis [16,17] and chemical bath deposition [8,9,18-25].

The characteristics of the CdS thin films required for the application as solar cell buffer layer are, it should be conductive ($\sim 10^{16}$ carriers/cm^3), thin to allow high transmission (50-100nm) and uniform to avoid short circuit effects [26]. Thickness as well as the deposition method of the CdS layer has a large impact on device properties. During the early days of the development of CuInSe$_2$/CdS junction, a thick (about 1-3 Ωm) CdS layer [27–29] was used as the buffer layer. The CdS layers of these devices were most often prepared by evaporation at substrate temperatures between RT and about 200^{0}C, or in some cases by sputtering [28]. The CdS film was often doped either with In [28] or Ga [30]. In some cases, a CdS bilayer was used [31,32], consisting of a thinner high-resistivity layer, prepared either by evaporation [31] or chemical bath deposition [31–33] and a thicker low-resistivity layer, doped with 2% In [32] or Ga [33]. Evaporated CdS has been used also in combination with the transparent conducting oxide layer [34–36]. Nowadays, chemical bath deposition is used almost exclusively [37,38], and therefore this section of the thesis focuses mainly on the chemical bath deposited CdS buffer layer. Solar cell with Mo/CIGS/CdS/ZnO device structure with the chemical bath deposited CdS has shown a record efficiency of 19.2% [39].

The chemical bath deposition of CdS modifies the absorber surface. The bath has been suggested to re-establish positively charged surface states and creates Cd$_{Cu}$ donors at the surface region [37,40]. Thus the interface between CIS and CBD-CdS is not abrupt but the layers are intermixed to some extent [41,42]. Both Cu-and Cd-diffusion play a role, and the intermixing is further enhanced during the post-deposition air annealing [1]. According to Nakada et al. [42], substitution of Cu by Cd takes place at the surface region of CIS (depth about 10 nm). The diffusion depth of Cd atoms may be related to the thickness of the Cu-deficient surface layer (CuIn$_3$Se$_5$) of CIS [42]. On the other hand, Heske et al. [41] have observed diffusion of Se and In from CIS into CdS and the diffusion of S from CdS into CIS. The extent of

interdiffusion depends on the structure of the absorber: (220/204) oriented CIS films have been found to allow more Cd atoms to diffuse into the CIS film [43].

Recently there has been a renewed interest in the study of nanocrystalline CdS thin films. The quantum confinement in the nanocrystalline thin films leads to the blue shift in the absorption edge resulting in a wide band gap energy, which can be effectively used to spectrally tune the optical properties of semiconductors [44]. The blue shift in the band gap due to the decrease in crystallite size has achieved a special attention because of its exciting scopes in fabricating novel electronic devices and solar cells of better efficiency [45,46]. Nanocrystalline CdS thin films have been prepared by different techniques such as sol-gel [47], chemical bath deposition [44, 48–51], electrostatic deposition [52] etc.

In this section we discuss the properties of the CdS films deposited on glass and indium tin oxide (ITO) coated glass substrates by chemical bath deposition. The films deposited on the ITO/glass substrates shows a blue shift in the band gap suggesting the nanocrystalline growth of the films.

3A.3 Experimental details

Cadmium sulphide thin films were prepared by the chemical bath deposition technique. The films were smooth, reflecting, and was bright yellow in appearance. The thickness of the film was calculated using Tolansky's multiple beam interferometry technique (see section 2.3.1). The thickness of the CdS film on ITO substrate for a deposition time of 45 minutes (single dip) was 52 nm. In order to get thicker films, multiple depositions were carried out with fresh reaction bath for each deposition. The measured thicknesses of the films are given in table 3.1.

The structural studies of the films were performed using the x-ray diffractometer. The optical absorption and transmission spectra of the as-deposited and annealed samples were recorded using UV-Vis-NIR

spectrophotometer (Hitachi-Model U3410). Four-probe method was used to study the electrical properties of the film (see section 2.3.6).

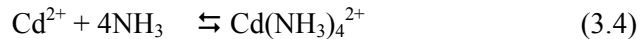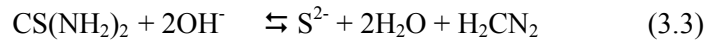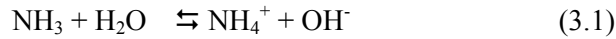## 3A.3.1. Preparation of the chemical bath

CdS thin films were deposited onto glass and indium tin oxide (ITO) coated glass substrates from an aqueous chemical bath containing 0.01 M cadmium chloride ($CdCl_2$), 0.1M thiourea ($CS(NH_2)_2$), 25% ammonia solution (NH_4OH) and triethanolamine (TEA). The volume mixture ratio of the cadmium chloride and thiourea was 1:1 and TEA was added by 4% of the volume of cadmium chloride. The pH of the solution was kept at 10.8 by adding ammonia solution and the bath temperature was maintained constant at 80^0C.

The substrates, both glass and ITO coated glass were cleaned thoroughly with detergent solution, rinsed in distilled water and then immersed in freshly prepared Chromic acid for two hours to remove traces of organic compounds. The substrates were again cleaned with distilled water and then kept in an ultrasonic cleaner for about 20 minutes to remove the microscopic impurities. Isopropyl alcohol was used for cleaning ITO coated glass substrate. The cleaned substrates were immersed vertically in the chemical bath and the deposition was carried out without any stirring for 45 minutes. After the deposition the films were rinsed in distilled water and dried in hot air oven. The post deposition annealing of the samples were done at 300^0C for one hour in vacuum (2×10^{-5} mbar).

3A.3.2 Reaction mechanism

In the growth of the CdS thin film from chemical bath, triethanolamine and ammonia act as the complexing agents to bind the Cd^{2+} ions. Formation of complex ion is essential to control the rate of the reaction and to avoid the immediate precipitation of the compound in the solution. The metal complexes hydrolyse slowly to generate the Cd^{2+} in the solution. Thiourea furnishes the necessary S^{2-} ions by hydrolysis. The deposition mechanisms

during chemical bath deposition of CdS thin films have been discussed by Chu et al.[53] and Herrero et al.[22]. The various reactions involved in the CdS growth process can be explained by the equations (3.1) – (3.7).

$$NH_3 + H_2O \leftrightarrows NH_4^+ + OH^- \qquad (3.1)$$

$$CdCl_2 \rightarrow Cd^{2+} + 2Cl^- \qquad (3.2)$$

$$CS(NH_2)_2 + 2OH^- \leftrightarrows S^{2-} + 2H_2O + H_2CN_2 \qquad (3.3)$$

$$Cd^{2+} + 4NH_3 \leftrightarrows Cd(NH_3)_4^{2+} \qquad (3.4)$$

$$Cd^{2+} + 2(TEA) \leftrightarrows Cd(TEA)_2^{2+} \qquad (3.5)$$

$$Cd^{2+} + S^{2-} \leftrightarrows CdS \qquad (3.6)$$

Assuming the metallic complex of the form CdL_n^{2+}, where L is the complexing agent, the general reaction for the CdS deposition can be represented as,
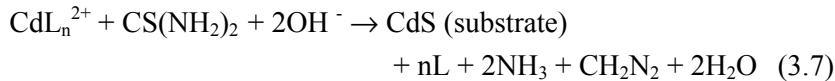
$$CdL_n^{2+} + CS(NH_2)_2 + 2OH^- \rightarrow CdS \text{ (substrate)}$$
$$+ nL + 2NH_3 + CH_2N_2 + 2H_2O \quad (3.7)$$

The pH of the reaction mixture is controlled by the addition of NH_4OH. The addition of NH_4OH increases the presence of NH_3 in the solution and there by increases the concentration of metal complex $Cd(NH_3)_4^{2+}$ (eqn 3.4) . At the same time the addition of NH_4OH increases the OH^- ion concentration in the solution and thereby favours the hydrolysis (eqn 3.3) of the chalcogen precursor. In the presence of sufficient NH_3 and TEA, Cd^{2+} ions exist in the solution mainly as $Cd(NH_3)_4^{2+}$ and $Cd(TEA)_2^{2+}$. The deposition of CdS occurs when the ionic product of Cd^{2+} and S^{2-} exceeds the solubility product. At a given temperature the rate of formation of CdS is determined by the concentration of Cd^{2+} provided by $Cd(NH_3)_4^{2+}$ and $Cd(TEA)_2^{2+}$ and the concentration of S^{2-} by the hydrolysis of $(NH_2)_2CS$.

3A.4 Results and discussion

3A.4.1 Structural analysis

The structure of the as-deposited and the annealed CdS films are investigated using the X-ray diffraction studies. The XRD spectra of the single dipped CdS films didn't show any peaks. This may be due to the very low thickness (67 nm) and nanoscale clustering of the as-deposited film. The double

dipped CdS films with 167 nm thickness, showed only a single peak at $2\theta = 26.6^0$ as shown in the figure 3.1. This single diffraction peak may be due to the reflection from the (111) plane of the cubic zinc blend or (002) plane of the hexagonal wurtzite structure of CdS (Fig.3.3a). The XRD spectra of the CdS films on ITO coated glass substrates are shown in figure 3.2. Here also the film showed only a single diffraction peak at $2\theta = 26.6^0$. All other peaks are that of the ITO.
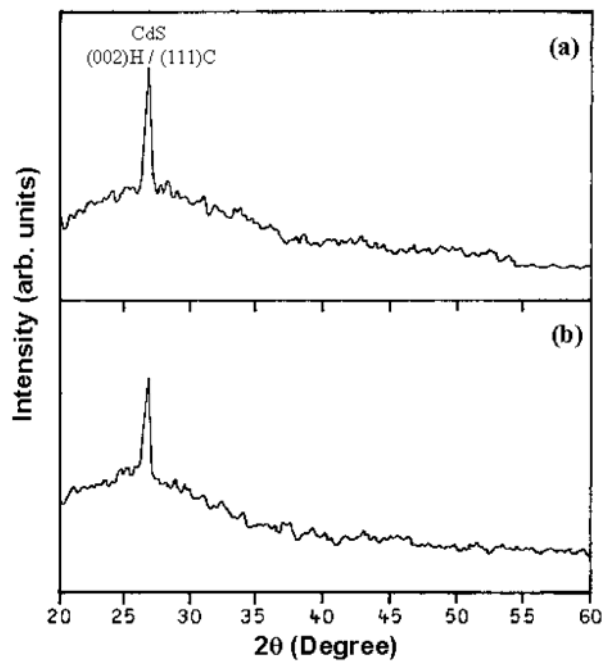
Fig.3.1 XRD pattern of double dipped CdS thin films on glass (a) as-deposited (b) annealed at 300^0C in vacuum

The structure of chemical bath deposited CdS thin films is reported to be cubic [54], hexagonal [20], mixed structure or poly type [21,53,55,56]. It has been reported that the cubic structure of CdS is a metastable one and the transition from the cubic to stable hexagonal structure can be achieved by annealing the films in controlled Ar + S_2 atmosphere [21,24,54]. In our experiment noticeable changes in the crystalline structure, or new phases were not observed on vacuum annealing at 300^0C for one hour. Similar

results have been reported for the CBD CdS films annealed at 400^0C in air [57,58]. Gosh et al.[59] have reported that the CdS nanocrystallites do not exhibit any structural transitions on vacuum annealing. Gibson et al. [56] have reviewed and modelled the structure of CdS
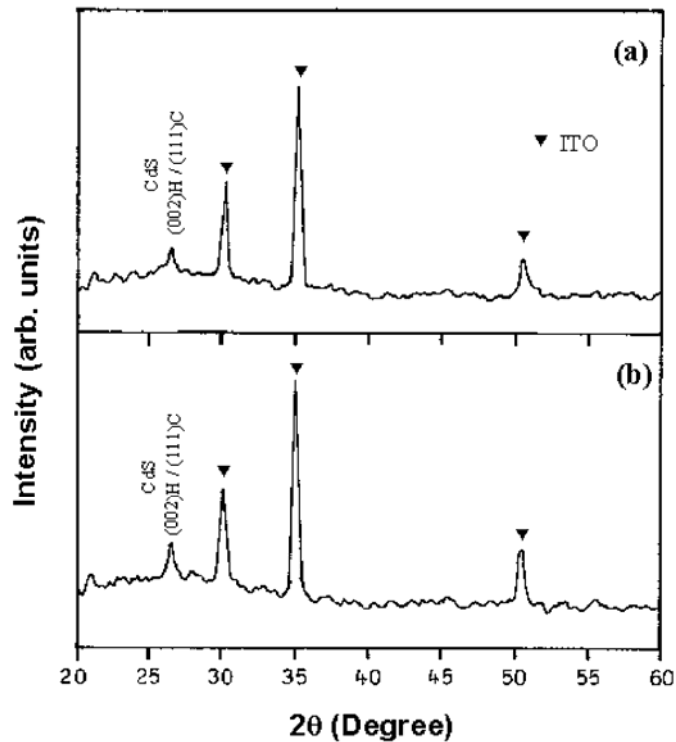
Fig.3.2 XRD pattern of double dipped CdS thin films on ITO coated glass substrates (a) as-deposited (b) annealed at 300^0C in vacuum

films and reported that when there is only a main peak near 27^0 and a clear hexagonal (102) peak or a clear cubic (200) peak is absent, a random poly type structure will be predominant in the film. Most of the nanocrystalline CdS films and nanoparticles can often be associated with a randomly oriented, randomly sequenced poly type structure rather than the hexagonal wurtzite or cubic zinc blend structures. Thin CBD films of CdS are also not textured. Thicker films may show better cubic or hexagonal crystal structure and a more pronounced texture [56]. Upon annealing in air, the diffraction patterns change only very slightly and practically no crystal growth occurs,

61
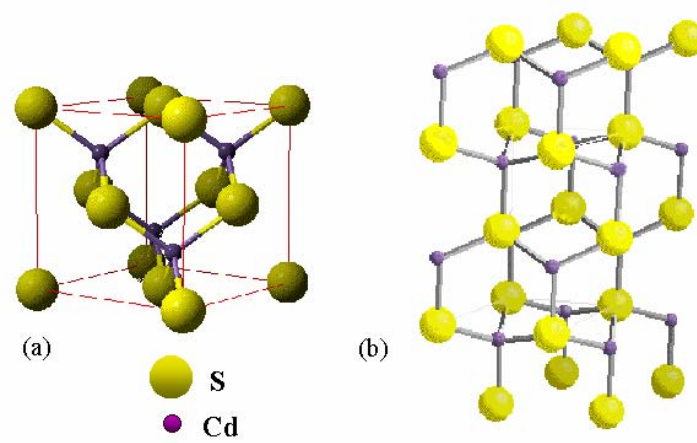
Fig. 3.3 The crystal structure of CdS (a) cubic zinc-blend (b) hexagonal wurtzite

confirming the proposal that the poly type structure is stabilized by a surface energy-volume energy competition that occurs in nanoparticles. Therefore the CdS films obtained in our experiment should be a polytype one exhibiting nanocrystallinity. The optical properties, like blue shifts in the band gap of the CdS films deposited on ITO coated substrates confirm this conclusion. The average grain sizes of the CdS films were estimated using
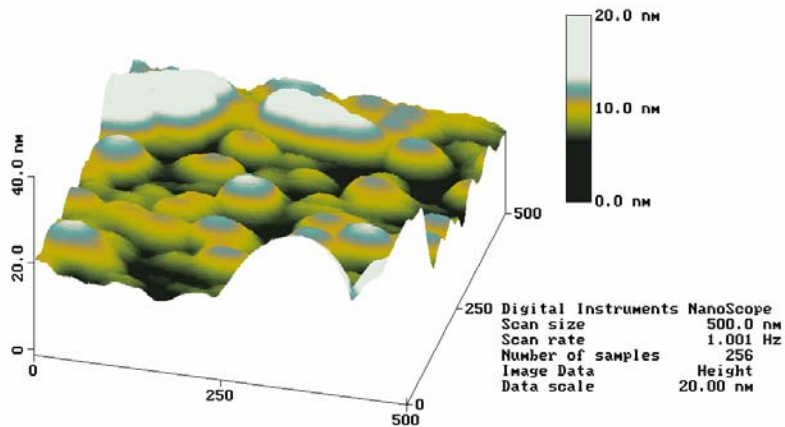
Fig 3.4 AFM image of the double dipped CdS film deposited on glass substrate

the Scherrer's formula (see section 2.3.4). The average grain sizes calculated for the as-deposited and annealed CdS films (double dipped) on glass

substrates were 24nm and 26nm respectively, whereas in the case of CdS films (double dipped) on ITO, these values were 11nm and 13nm. The AFM picture of the CdS films (double dipped) deposited on glass substrate is shown in figure 3.4. The film shows an average surface roughness of 10nm suggesting a uniform and smooth growth over the surface.

3A.4.2 Optical characterisation

The optical transmission spectra of the as-deposited and annealed samples show that the double dipped samples have more transparency in the visible region compared to the single dipped films (Fig 3.4). This might be due to the surface roughness of the single dipped films. The films prepared on ITO have more transparency (>85%) than that on glass substrates. This might be
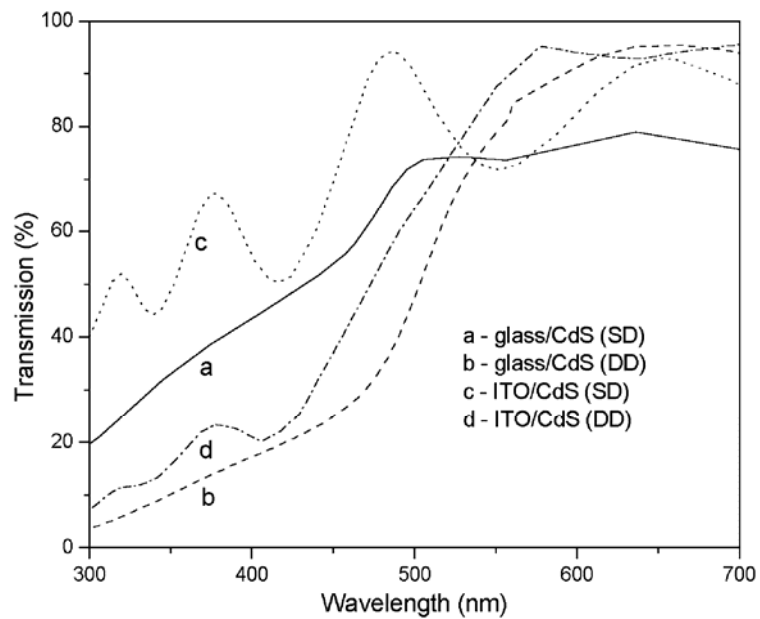
Fig. 3.4 Transmission spectra of the as-deposited CdS films

63

due to the ordered and uniform growth of the CdS films on crystalline ITO substrates. Since CdS is a direct band gap material their band gap values are calculated from the $(\alpha h\nu)^2$ against hν plots (see section 2.3.5). The $(\alpha h\nu)^2$ curves of the as-prepared and annealed films are shown in figures 3.5 and 3.6. The calculated values of the band gaps are summarized in table 3.1. The single dipped films show higher band gap than the double dipped films. Vacuum annealing of the films resulted in the reduction of the band gap. But in the case of double dipped CdS films on glass, the band gap didn't show any appreciable change due to annealing. The reduction in band gap of the single dipped CdS films on glass may be due to the changes in the crystallinity of the film.

Table 3.1 The band gap values and the crystalline sizes of the CdS thin films

substrate	no. of dips	thickness (nm)	band gap (eV)		Crystalline size (nm)			
					from band gap		from XRD	
			as deposited	annealed	as deposited	annealed	as deposited	annealed
Glass	single	67	2.46	2.40	16	-	-	-
Glass	double	167	2.43	2.42	22	27	24	26
ITO	single	52	2.67	2.60	7.3	8.5	-	-
ITO	double	115	2.58	2.55	9	10	11	13

The quantum size effect causes a perturbation in the electronic structure and the conduction and valence band are broken down to discrete states resulting in the widening of the forbidden band gap compared to the bulk [48,60]. In the case of nanoparticle growth of thin films, a hyperbolic band model has been proposed to explain the change of energy gap as a function of particle size [48,61]. According to this model, the equation for the band gap of nanocrystallites (E_n) is given by,

$$E_n = \left(E_b^2 + \frac{2E_b \hbar^2 \pi^2}{m^* R^2} \right)^{1/2} \qquad (3.8)$$

where, E_b is the band gap for the bulk semiconductor (2.4 eV for CdS), R is

the particle radius and m* is the effective electron mass. For CdS, $m^*/m_e = 0.2$ [48], where m_e is the mass of the free electron.
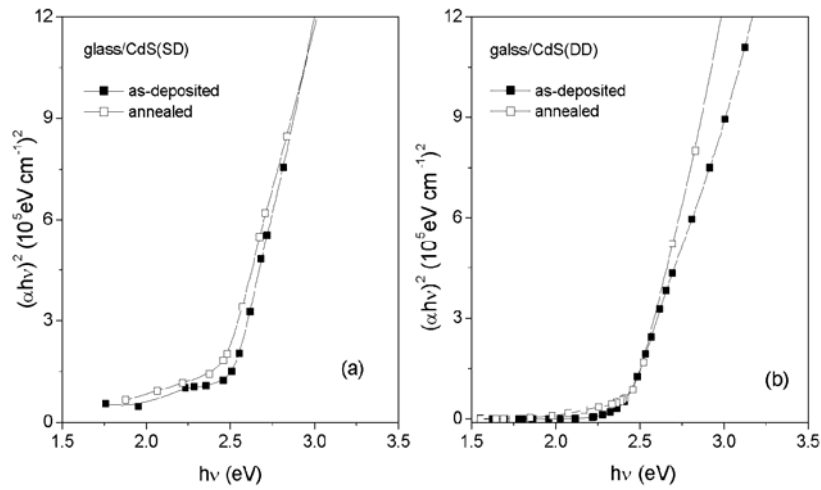
Fig. 3.5 $(\alpha h\nu)^2$ against $(h\nu)$ plots of the as-deposited and annealed CdS films deposited on glass substrates: (a) single dip film (67nm) (b) double dip film(167nm)
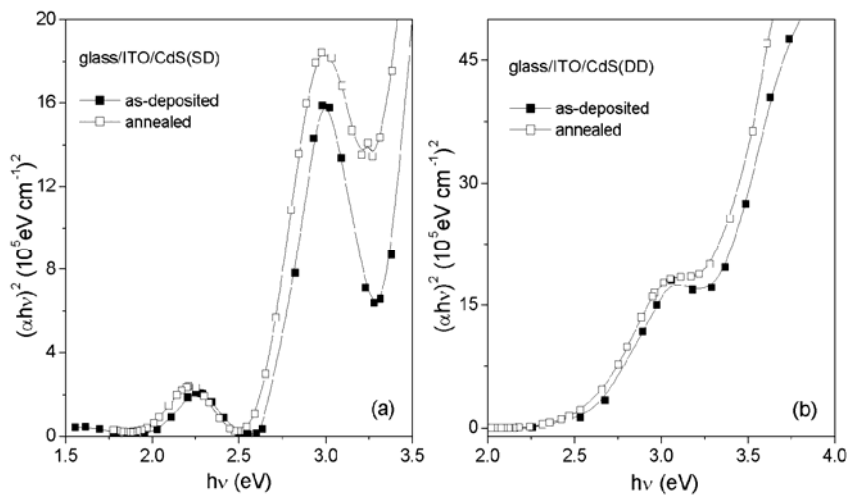
Fig. 3.6 $(\alpha h\nu)^2$ against $(h\nu)$ plots of the as-deposited and annealed CdS films deposited on ITO coated glass substrates: (a) single dip film (52nm) (b) double dip film (115nm)

The crystalline sizes of the CdS films are estimated from the blue shift using the above equation and are given in table 3.1. The crystalline size varies from 7.6 nm to 22 nm. These are in agreement with the average grain size obtained from X-ray diffraction. The single dipped films show low crystalline size indicating more quantum confinement at low thickness. The crystalline size increases due to the annealing.

3A.4.3 Electrical properties

The electrical resistivity of the as deposited and annealed CdS film on glass substrates was measured by the four-probe method. The resistivity values of the as-deposited single dip film (67 nm) and double dip film (167 nm) was 2.5×10^5 Ωcm and 1.1×10^2 Ωcm respectively. The double dipped films didn't show any change in the order of resistivity upon vacuum annealing. The high resistivity of the single dipped CdS films might be due to the grain boundary effects due to the roughness and non-uniformity in the film at low thickness. The carrier concentration of the as deposited double dipped CdS film was 1.97×10^{17} carriers/cm^3.

3A.5 Conclusion

CdS films were prepared by chemical bath deposition technique. The films deposited on ITO coated glass substrates were found to be nanocrystalline with a poly type structure. The optical band gaps of the as-deposited films were in the range 2.43eV to 2.67eV. The crystalline sizes of the films were estimated from the blue shift in the optical band gap. Vacuum annealing of the films caused a reduction in the band gap. The low resistivity ($\sim 10^2$ Ωcm), high transparency (above 80%), carrier concentration of $\sim 10^{17}$ carriers/cm^3 and the feasibility of band gap engineering by quantum confinement at low thickness suggest these films as suitable buffer layers in solar cells.

Part B

Chemical bath deposition of Zn$_x$Cd$_{1-x}$S thin films and the effect of indium doping

Zn$_x$Cd$_{1-x}$S thin films are prepared by chemical bath deposition. The band gap varies from 2.43 to 2.66 eV when the volume mixture ratio of Zn changes from x = 0 to 0.5. The resistivity of the films also increases with Zn incorporation. Resistivity of the Zn$_x$Cd$_{1-x}$S films decreases with In doping.

3B.1 Introduction

Cadmium sulphide continues to hold an important position in CdS/CdTe and CdS/CuInSe$_2$ solar Cells. The CIGS solar cell having the highest reported efficiency of 19.2% is based on chemical bath deposited CdS as the buffer layer. In order to decrease the optical absorption losses and to enhance the response in the short wavelength region, alternative, more transparent buffer materials have been looked for. A ternary derivative of CdS such as $Zn_xCd_{1-x}S$ is a promising material in this respect. CdS and ZnS form solid solutions in a wide compositional range so that the band gap tailoring of this ternary compound can be achieved by the variation in composition [62].

3B.2 (CdZn)S as a wide band gap buffer layer

Cadmium zinc sulphide thin films have been used as a wide band gap buffer layer in heterojunction solar cells [63,64] and in photoconducting devices [65]. Devaney et al. [63] deposited uniform (Cd,Zn)S buffer layers by the chemical bath deposition from ZnCl$_2$, CdCl$_2$, NH$_4$Cl, NH$_4$OH and thiourea at 85^{0}C. The Zn to (Zn+Cd) ratio in the best films was 15–20 %, resulting in a conversion efficiency of 12.5 % with absorbers prepared by co-evaporation. Basol et al. [64], in turn, prepared (Cd,Zn)S buffer layers with about 10 % Zn by CBD from Zn-acetate, Cd-acetate, triethanolamine, NH$_4$OH and thiourea at 55^{0}C, and achieved conversion efficiencies between 10 and 13 %.

Various methods have been used to deposit $Zn_xCd_{1-x}S$ thin films viz: screen printing [66,67], electrodeposition [62], spray pyrolysis [68,89], molecular beam epitaxy [70], sputtering [71] etc. There are a few reports on the chemical bath deposition of $Zn_xCd_{1-x}S$ thin films from alkaline [72–78] and acidic [79] solutions. A linear variation of band gap from 2.5eV for CdS to 3.6 eV for ZnS has reported by Padam et al. [74]. Along with the increase in the band gap, an increase in the resistivity of the $Zn_xCd_{1-x}S$ films has been observed due to the Zn incorporation in the film [74,78]. The resistivity was increased from 10^9 to 10^{12} Ωcm when the composition of Zn was varied in the range $0 \leq x \leq 1$ [74]. Dona et al.[78] have obtained films with three

mixed phases (CdS, ZnS and $Zn_xCd_{1-x}S$) and the electrical conductivity of $Zn_xCd_{1-x}S$ films was dominated by the conductivity of the pure ZnS phase in the film. Vacuum [62] and hydrogen annealing [74] of the $Zn_xCd_{1-x}S$ films decreases the resistivity.

The compositional dependence of resistivity is a basic property of the (Cd,Zn)S solid solution and its is not appreciably altered by the method of preparation. This high resistivity of the $Zn_xCd_{1-x}S$ films limits their utilization as a buffer material in heterojunction devices. Doping of indium and hydrogen annealing are suggested to be the suitable methods for getting low resistive $Zn_xCd_{1-x}S$ thin films [68,69,74,77]. Subbaramaiah et al. [68] have reported the fabrication of all spray-deposited $CuIn(S_{0.5}Se_{0.5})_2$ solar cell with In doped $Zn_{0.05}Cd_{0.95}S$ buffer layer. The conversion efficiency of the cell was only 1.1%. $InCl_3$ was used as the dopant during spray pyrolysis and its concentration was 6 at %. The as-deposited $Zn_{0.05}Cd_{0.95}S$:In films showed a resistivity of 170 Ωcm and an optical band gap of 2.41eV [68].

Lee et al. [77] have reported the thermal diffusion of In by the annealing of In/(Cd,Zn)S bilayers. Indium films of different thickness were evaporated over the chemical bath deposited (Cd,Zn)S films and the bilayers were annealed in air (150–550^{0}C) for 1 h. The as prepared (Cd,Zn)S films without the In doping showed a high resistivity of 2.4 x 10^5 Ωcm. A lowest resistivity of 0.25Ωcm was obtained for the (Cd,Zn)S film coated with 40nm In and annealed at 450^{0}C for 1 h in air. The decrease in resistivity at high annealing temperatures is due to the partial oxidation of (Cd,Zn)S films to CdO [77].

In this section of the thesis, studies on the chemical bath deposited $Zn_xCd_{1-x}S$ thin films are presented. The widening of the band gap and the increase in resisitivity of these films with the increase in Zn concentration are investigated. In order to decrease the high resistivity of these flms, the films are doped with In during chemical bath deposition.

3B.3 Experimental Details

$Zn_xCd_{1-x}S$ thin films were prepared from aqueous solution containing cadmium chloride (0.01M), zinc chloride (0.1M), thiourea (0.1M), 25% ammonia solution and triethanolamine (TEA). The pH of the solution was adjusted to be 10.8 by the addition of ammonium hydroxide solution. The chemical bath is prepared from 10ml of cation precursors (total volume of $CdCl_2$ + $ZnCl_2$ solutions) and 4ml (4% of the volume of the metal precursors) triethanolamine. The solution is stirred well and required amount of ammonia solution was added to get a pH value 10.8. After proper mixing of the solution, 10 ml of thiourea was added into it and the reaction mixture was kept in a water bath at 80^0C. The cleaned glass substrates (see section 3.3.1) were immersed vertically in the chemical bath and the deposition was carried out without any stirring for 45 minutes (single dip). After the deposition, the films were rinsed in distilled water and dried in hot air oven.

$Zn_xCd_{1-x}S$ thin films were prepared for various volume mixture ratios (x) of the $ZnCl_2$ and $CdCl_2$ solutions. The volume mixture ratio of the cation precursors, 'x' can be represented as,

$$x = \frac{V_{Zn}}{V_{Zn} + V_{Cd}} \qquad (3.9)$$

where, V_{Zn} and V_{Cd} are the volumes of $ZnCl_2$ and $CdCl_2$ solutions respectively. The total volume ($V_{Zn} + V_{Cd}$) of the cation precursors is always kept as 10ml and the value of x was varied from x = 0.1 to 0.5 by mixing different volumes of the cadmium and zinc solutions.

The deposition process is based on the controlled precipitation of zinc and cadmium sulphide in the chemical bath. The solubility products of the metal sulphides are very small (K_{sp} (ZnS) = 10^{-25}, K_{sp} (CdS) = 10^{-27}) and therefore formation of complex ions is essential to control the immediate precipitation of the cation precursors. Ammonia and triethanolamine acts as the complexing agents and binds the Zn^{2+} and Cd^{2+} ions in the chemical bath as described in section 3.3.2.

Indium doping in the $Zn_xCd_{1-x}S$ was achieved by adding high purity (99.99%) indium trichloride (0.001M) solution into the chemical bath used for $Zn_xCd_{1-x}S$ deposition. The doping volume ratio, 'y' can be expressed as,

$$y = \frac{V_{In}}{V_{Zn} + V_{Cd}}$$ (3.10)

where, V_{In} is the volume of $InCl_2$ solution. Doping was carried out for $y = 0.1$ and 0.2.

The thickness of the film was found out using Tolansky's multiple beam interferometry technique (see section 2.3.1). Since the thickness of the single dipped $Zn_xCd_{1-x}S$ films (deposition time 45 min) was less, multiple depositions were carried out with fresh reaction bath each time for getting thicker films. All the measurements were done on the films prepared by double dipping (total deposition time = 90 min.) in the chemical bath. The optical transmission spectra of the films were recorded using UV-Vis spectrophotometer. The electrical resistivity of the films were measured by the two-probe method with evaporated In electrodes.
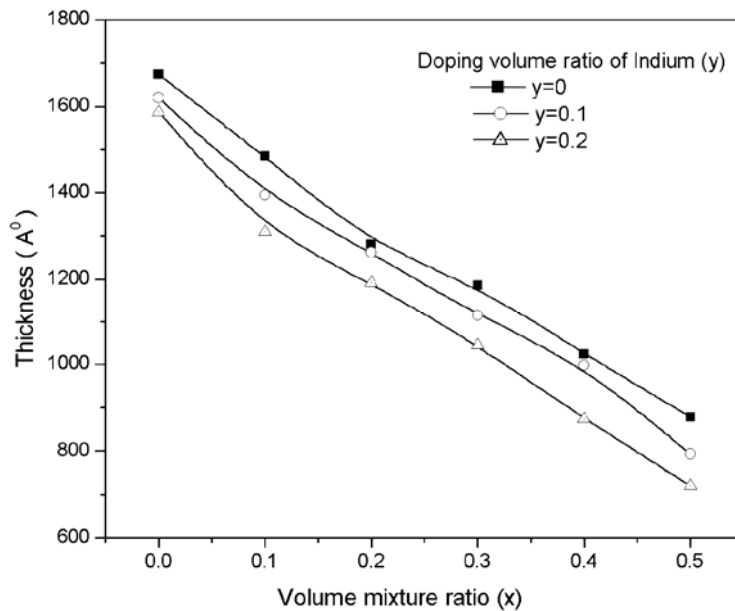
Fig. 3.7 Variation of thickness of $Zn_xCd_{1-x}S$ thin films with volume mixture ratio (x)

3B.4 Results and Discussion

The as-deposited $Zn_xCd_{1-x}S$ thin films were found to be smooth adherent and reflecting. As the Zn content in the solution increases the colour of the films changes from bright yellow to pale yellow. The film thickness for a constant deposition time of 90 min was found to decrease almost linearly with increase of Zn content in the solution (Fig. 3.7).
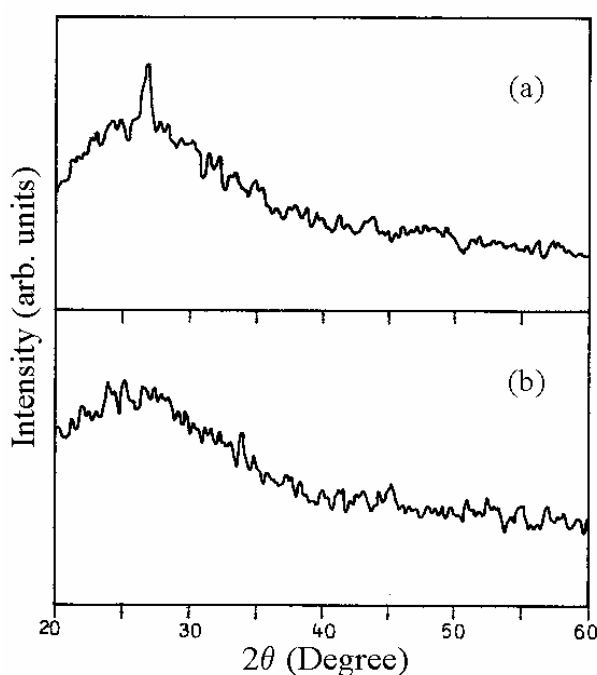
Fig. 3.8 The XRD patterns of the as-deposited (a) $Zn_{0.1}Cd_{0.9}S$ and (b) $Zn_{0.3}Cd_{0.7}S$ films

3B.4.1 Structural analysis

The X-ray diffraction studies on the $Zn_xCd_{1-x}S$ films showed crystalline nature for the films deposited with volume mixture ratio, $x \leq 0.2$. XRD spectra showed only a single peak at 26.6^0 (Fig.3.8). The single peak at 26.6^0 may be due to the cubic or wurtzite phase of the film. As the concentration

of Zn in the reaction bath increases (x > 0.2), the film growth is expected to be cluster-by-cluster deposition than ion-by-ion deposition and the film structure deviates from a solid solution, resulting in an amorphous nature of the film as shown in figure 3.8b.

3B.4.2 Optical properties

The optical transmission spectra of the as-deposisted $Zn_xCd_{1-x}S$ thin films for x = 0.1 to 0.5 are shown in figure 3.9. The $Zn_xCd_{1-x}S$ films show transparency above 75 % in the visible region of light. The transparency of the films decreases for x = 0.1 to 0.3 and then increases. The transmission edge shows a blue shift as the Zn content in the reaction mixture increases.
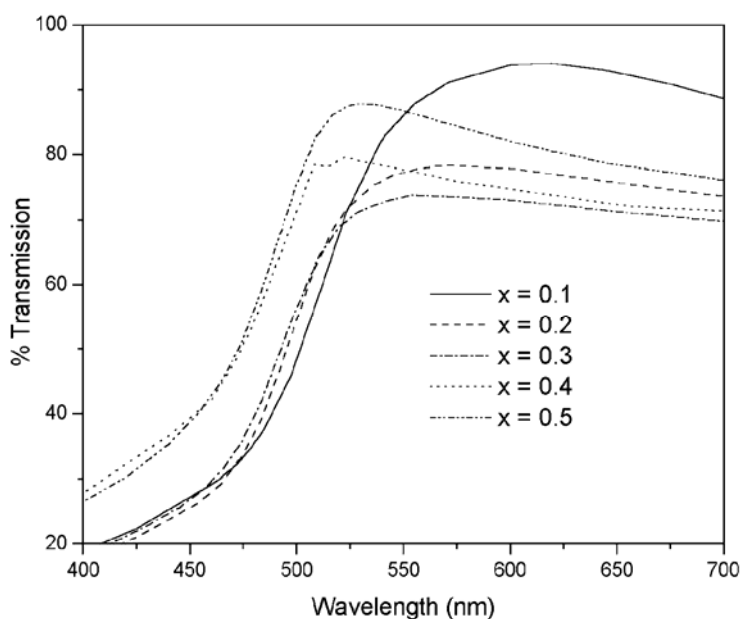

Fig. 3.9 Transmission spectra of $Zn_xCd_{1-x}S$ thin films

The band gap of the $Zn_xCd_{1-x}S$ thin films are calculated from the intercept of the $(\alpha h\nu)^2$ curves plotted against the photon energy, hν (Fig.3.10). The band gap of the films increases with the increase in volume mixture ratio 'x'. The as deposited CdS film is having a band gap of 2.43 eV. In the case of

$Zn_xCd_{1-x}S$ thin films, the band gap increases from 2.46 to 2.66 when the volume mixture ratio was increased from x = 0.1 to 0.5 (Fig. 3.11). For higher concentrations of x, ie. x ≥ 0.3, the $(\alpha h\nu)^2$ Vs (hν) plots show two distinct linear regions (Fig.3.10) which on extrapolation give rise to two band gap values. This can be interpreted as the presence of another direct optical transition. The films prepared with x ≥ 0.3 showed a lower band gap value around 2.45eV in addition to the wide band gap corresponding to the $Zn_xCd_{1-x}S$.
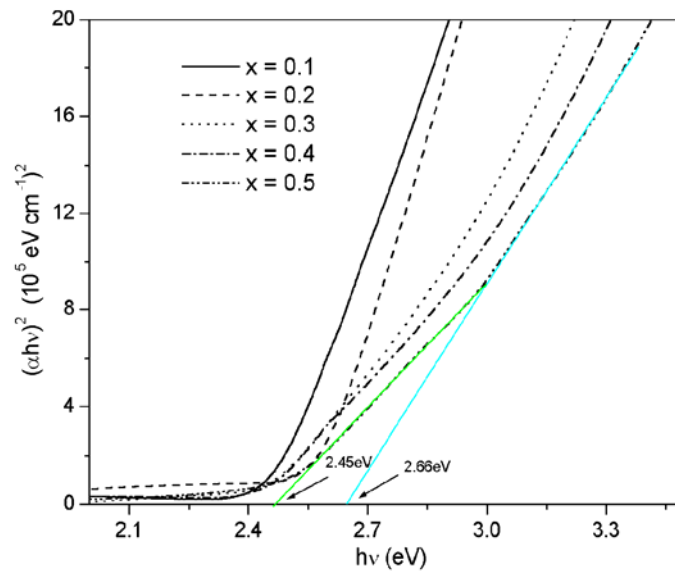
Fig.3.10 $(\alpha h\nu)^2$ against hν plots of $Zn_xCd_{1-x}S$ thin films

The 2.45eV band gap value indicates the presence of certain amount of pure CdS phase in these samples. Similar results have reported by Abrahams et al. [80] in the co-precipitation of ZnS–CdS colloidal particles and also by Dona et al. [78]. The presence of the pure CdS in the films gives an idea of the method of formation of $Zn_xCd_{1-x}S$ thin films. Probably the film formation starts with the formation of the pure CdS particles, which is the fastest process. The formation of ZnS starts immediately. The final structure can be understood as CdS particle surrounded by $Zn_xCd_{1-x}S$ cluster. This argument is supported by the results obtained in XRD and electrical resistivity

measurements. The films with $x \geq 0.3$ were showing amorphous nature and high resistivity.
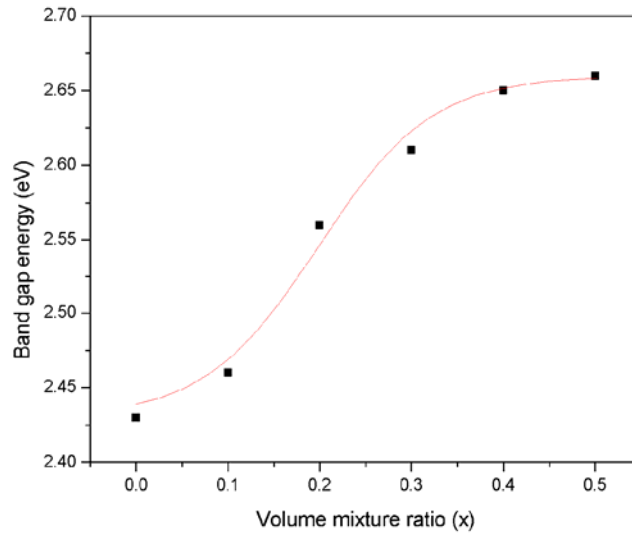
Fig. 3.11 The band gap energies of $Zn_xCd_{1-x}S$ thin films for $x = 0$ to 0.5

3B.4.3 Electrical properties

The resistivity of the $Zn_xCd_{1-x}S$ films increases with the increase in the volume mixture ratio 'x'. The zinc incorporation increases the resistivity. The as-deposited CdS films showed a resistivity of 1.1×10^2 Ωcm. In the case of $Zn_xCd_{1-x}S$ films, the resistivity was $\sim 10^2$ Ωcm for $x \leq 0.2$. The films become highly resistive at higher concentrations of Zn as shown in table 3.2. This high value of resistivity might be due to the presence of amorphous clustering of $Zn_xCd_{1-x}S$ around the CdS nuclei at higher Zn concentrations. The amorphous nature of the films by XRD for $x > 0.2$ confirms this conclusion.

3B.5 Effect of Indium doping

Indium doping is having significant effect on the growth, electrical and optical properties of the as deposited $Zn_xCd_{1-x}S$ thin films. The thickness of

the as-deposited $Zn_xCd_{1-x}S$ films was found to decrease with the indium doping concentration as shown in Fig 3.7. The In doped $Zn_xCd_{1-x}S$ films showed amorphous nature in the X-ray analysis whereas CdS films retained its crystalline nature.

An increase in band gap due to indium doping was observed for CdS and $Zn_{0.1}Cd_{0.9}S$ films. The band gap of the CdS film increases from 2.43 to 2.48eV (Fig. 3.12). The broadening of band gap due to Indium doping may be due to filling up of conduction band edge by the excessive carriers donated by the impurity atoms. This leads to blue shift in optical band-to-band transitions by blocking the low energy transitions, known as Burstein Moss effect. $Zn_xCd_{1-x}S$ thin films prepared from chemical baths with $x \geq 0.2$ showed decrease in band gap due to the In doping. But the resistivity is found to decrease. The electrical resistivity values of the as-deposited and the In doped films are summarized in table 3.2. The resistivity value of all the films

Table 3.2 Electrical resistivity of the as-deposited and indium doped $Zn_xCd_{1-x}S$ films for various doping volume ratios of $InCl_3$ (y).

Sample	Electrical resistivity (Ωcm)		
	y = 0	y = 0.1	y = 0.2
CdS	1.10×10^2	27.5	1.93
$Zn_{0.1}Cd_{0.9}S$	2.68×10^2	32.6	6.52
$Zn_{0.2}Cd_{0.8}S$	4.05×10^2	96.9	23.45
$Zn_{0.3}Cd_{0.7}S$	6.70×10^3	4.48×10^3	6.29×10^2
$Zn_{0.4}Cd_{0.6}S$	6.90×10^4	9.34×10^4	3.79×10^2
$Zn_{0.5}Cd_{0.5}S$	2.72×10^5	1.82×10^5	4.15×10^3

decreases by 2 orders on indium doping. The appreciable variation of resistivity of $Zn_xCd_{1-x}S$ films due to indium doping indicates the increase in carrier concentration. The increase in electrical conductivity of these films might be due to interstitially or substitutionally doped In atoms which acts as donor impurities. The enhanced carrier concentration due to the donor

atoms, result in band gap narrowing of $Zn_xCd_{1-x}S$ thin films with $x \geq 0.2$. This may be due to the band tailing by the impurity levels and also due to the many body effects. The band gaps of the indium doped films were calculated from the absorption spectra of the films by plotting $(\alpha h\nu)^2$ against $h\nu$ curves. Typical absorption spectra of the as-deposited and In doped $Zn_{0.2}Cd_{0.8}S$ films are shown in Fig.3.13. The inset of the figure shows the corresponding $(\alpha h\nu)^2$ against $h\nu$ plots. A red shift of the absorption edge occurs due to the In doping. The calculated values of the band gap of the as deposited and the In doped $Zn_xCd_{1-x}S$ films are summarized in table 3.3.

Table 3.3 Band gap values of the as-deposited and indium doped $Zn_xCd_{1-x}S$ films for various doping volume ratios of In (y).
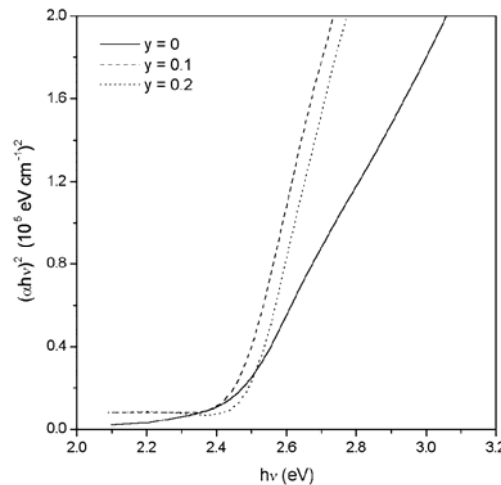
Sample	Optical band gap (eV)		
	$y = 0$	$y = 0.1$	$y = 0.2$
CdS	2.43	2.45	2.48
$Zn_{0.1}Cd_{0.9}S$	2.46	2.48	2.51
$Zn_{0.2}Cd_{0.8}S$	2.56	2.50	2.48
$Zn_{0.3}Cd_{0.7}S$	2.61	2.53	2.42
$Zn_{0.4}Cd_{0.6}S$	2.65	2.36	2.26
$Zn_{0.5}Cd_{0.5}S$	2.66	2.33	2.12

Fig.3.12 $(\alpha h\nu)^2$ against $h\nu$ plots of CdS films for different doping volume ratios (y) of Indium

77
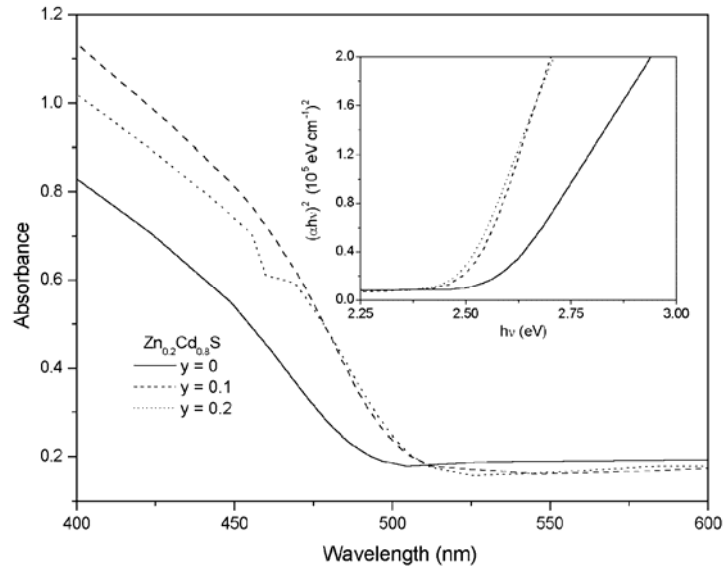
Fig. 3.13 Absorption spectra of the as-deposited and In doped $Zn_{0.2}Cd_{0.8}S$ films. Inset shows the the corresponding $(\alpha h\nu)^2$ against $h\nu$ plots.

3B.6 Conclusion

$Zn_xCd_{1-x}S$ thin films were deposited by chemical bath deposition for $x = 0$ to 0.5. The band gap of the films varied from 2.43 to 2.66 eV and the electrical resistivity of the films were found to increase with the increase in Zn content in the solution. Indium was doped into the $Zn_xCd_{1-x}S$ film by adding $InCl_3$ into the chemical bath during deposition and the electrical resistivity of the films was found to decrease by an order of two compared to the undoped $Zn_xCd_{1-x}S$ films. The low resistivity and the wide band gap of $Zn_xCd_{1-x}S$:In films suggest them as a better material for the buffer layer application for heterojunction solar cells. The wide band gap along with the reduced resistivity by indium doping suggest $Zn_xCd_{1-x}S$ films, as a better substitute for cadmium sulphide buffer layer in heterojunction solar cells.

Part C

Preparation and characterisation of ZnS thin films by chemical bath deposition

Zinc sulphide thin films were prepared by chemical bath deposition and the properties of these films are compared with those deposited by electron beam evaporation. The variation in the optical and electrical properties of the CBD grown ZnS films with the pH of the reaction mixture was investigated. The chemically deposited ZnS films showed a wide band gap of 3.93eV and a transparency of more than 80% in the visible region. The lowest resistivity of ~10^4 Ωcm was obtained for the films prepared from a chemical bath of pH 10.6. The refractive index, extinction coefficient and the dielectric constants of CBD ZnS films are also found out.

3C.1 Introduction

Due to the environmental concerns associated with Cd-containing materials, serious efforts have been directed towards completely Cd-free buffer materials. The materials studied include Zn and In-based materials such as sulphides, selenides, hydroxy sulphides and hydroxy selenides. The conversion efficiencies of Cd-free devices are approaching those of the devices with CdS buffer layer. Recently, a conversion efficiency of 18.1 %, close to those of the best CdS window layer based devices, was achieved using a CBD-ZnS buffer layer in combination with a CIGS absorber prepared by three-stage co-evaporation in a MBE system [81]. The CBD-ZnS was found to be sensitive to oxygen-induced damage during sputter deposition of undoped ZnO, and thus the device was prepared without the undoped ZnO layer [81]. The optimum thickness of the ZnS layer was 130 nm, indicating the need for reduction of shunt paths between CIGS and ZnO:Al. As expected on basis of the higher band gap of the buffer, the cell exhibited higher quantum efficiency at short wavelengths than a cell with CdS buffer.

3C.2 ZnS thin films by chemical bath deposition

Though CBD has been effectively used to deposit different chalcogenides such as CdS, PbS, Bi_2S_3 etc., the deposition of crystalline ZnS by CBD is a difficult one. Generally the ZnS films obtained by CBD are either amorphous or poorly crystallized. Therefore annealing at high temperatures was needed to improve the crystallinity of the films [82,83]. There are a few reports on the chemical bath deposition of ZnS thin films [82–92].

Cheng et al. [84] have deposited crystalline ZnS films with wurtzite structure from alkaline solutions using tri-sodium citrate as the complexing agent. The deposition was carried out at a bath temperature of 80^0C. The optical band gap of the as-deposited films was found to be 3.53eV. Though Johnson et al. [85] have used tri-sodium citrate as the complexing agent, discernable diffraction peaks was not seen. Therefore it is proposed that the

concentration of the tri-sodium citrate has a significant influence on the crystallization and orientation of the CBD-ZnS.

Ammonia and hydrazine are the popular choices as the complexing agent in the CBD of ZnS film. Vidal et al. [86] reported the influence of NH_3 concentrations on the properties of CBD-ZnS films. Dona et al. [83] have deposited ZnS films using hydrazine hydrate as a complexing agent. Oladeji and Chow [87] have reported that the presence of an ammonium salt in the chemical bath increases the thickness of the ZnS film. The importance of ternary complexes in the chemical bath deposition of ZnS has been studied and modeled by O' Brien et al. [88]. Thiourea [83,84,86,87,92] or thioacetamide [82,89] was often used as the chalcogen precursor, and acetate [84], chloride [86,92] or sulphate [82,83,87,89] solution of Zn was used as the cation precursor for the chemical bath deposition of ZnS thin films.

In this section, the preparation and characterization of ZnS thin films by chemical bath deposition is discussed. The properties of the CBD ZnS films are compared with the ZnS films deposited by electron beam evaporation. The effect of pH on the electrical and optical properties of these films prepared from two different zinc salts (zinc chloride and zinc nitrate) is investigated. Ammonia and hydrazine were used as the complexing agents, and the deposition was carried out in the presence of an ammonium salt. The growth mechanism of ZnS films during chemical bath deposition is also discussed.

3C.3 Experimental details

The chemical bath deposition of ZnS on glass and indium tin oxide (ITO) coated glass substrates were carried out from a chemical bath containing zinc nitrate [$Zn(NO_3)_2$] / zinc chloride ($ZnCl_2$) , thiourea [$CS(NH_2)_2$] , 25 % ammonia solution (NH_4OH) , 80 % hydrazine hydrate (N_2H_2OH) and ammonium nitrate (NH_4NO_3) / ammonium chloride (NH_4Cl) . All the reagents used were of analytical grade. The films were prepared separately from two sources of zinc, viz: zinc nitrate and zinc chloride. The electron

beam evaporation of the ZnS films were carried out at 2×10^{-5} mbar. Films were deposited on glass substrates at various substrate temperatures.

The transmission spectra of the as-deposited samples were recorded using an ultraviolet-visible spectrophotometer (Hitachi-Model U3410). The electrical resistivity of the as-deposited ZnS films were measured by a two-probe arrangement with the electrodes in planar geometry using a Keithley`s source measure unit (Model SMU236).

3C.3.1 Preparation and optimization of the chemical bath

The chemical bath contains 5 ml of 1 N solution of $Zn(NO_3)_2$ mixed with 2 ml of hydrazine hydrate and 2.5 ml of 0.5 N ammonium nitrate (buffer) solution. NH_4OH was added into this solution to adjust the pH at the desired value. Then 5 ml of 1 N solution of thiourea was added into this mixture and stirred well. This reaction mixture was transferred into a beaker in which the substrates were kept vertically. The deposition was carried out at a temperature of 80 ^{0}C by keeping the chemical bath in thermostated water bath. All the samples reported here are for the deposition time 2 h at a bath temperature of 80 ^{0}C. After the deposition, the samples were taken out, washed in distilled water and dried in a hot air oven. The film on one side of the substrate was removed by careful etching with dilute hydrochloric acid. The film deposition was carried out with the same bath composition for different pH values, ranging from 10 to 10.6.

ZnS films were also prepared under identical conditions from the reaction mixture containing 5 ml of 1 N solution of $ZnCl_2$, 2 ml of hydrazine hydrate, 2.5 ml of 0.5 N ammonium chloride (buffer) and 5 ml of 1 N thiourea. An ammonia solution was used to vary the pH value of the chemical bath from 10 to 10.6.

The addition of ammonium nitrate or ammonium chloride helps to control the pH value more easily [87]. In the presence of hydrazine and ammonia, the zinc complexes $[Zn(NH_3)_4]^{2+}$ and $[Zn(N_2H_4)_3]^{2+}$ were formed, resulting

in a slow release of Zn^{2+} ions. The thickness of the film was measured gravimetrically using a microgram balance. The thickness of the ZnS films increased from 0.18 to 0.25 µm when the pH value of the solution was varied from 10 to 10.6. Figure 3.14 shows the variation of thickness of the ZnS film prepared from zinc nitrate and zinc chloride with the pH of the reaction mixture for a constant dipping time of 2 h. The bath temperature in CBD technique can be effectively used to control the rate of ZnS formation. The hydrolysis of thiourea is greatly enhanced by the increase in bath temperature. The equilibrium constants of all reactions are temperature dependent. Films with good adhesion and morphology were obtained for a bath temperature of 80 ^{0}C.
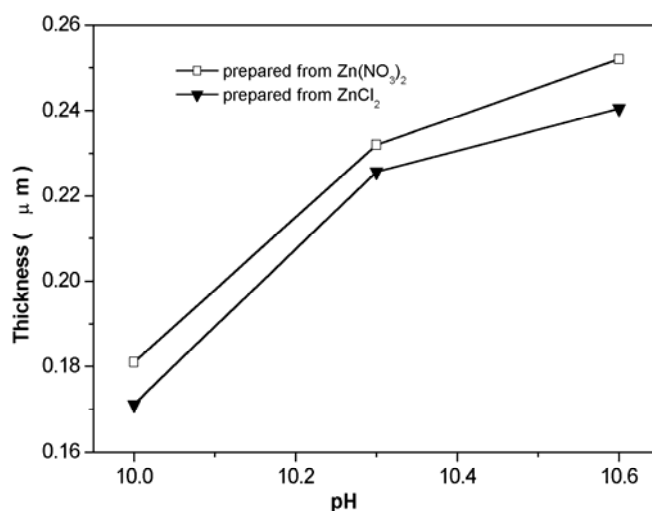
Fig.3.14 Thickness of CBD ZnS thin films deposited at different pH of the chemical bath for a constant dipping time of 2 h.

The deposition was carried out for different volume ratios of the zinc nitrate (or zinc chloride), thiourea and the buffer ammonium salt. It was observed that when the corresponding volume mixture ratio was 2:2:1, the films obtained were smooth and uniform. The films prepared under these optimized conditions showed a Zn-to-S ratio of 1:1 in the energy-dispersive X-ray measurement.

3C.3.2 Deposition mechanism

In chemical bath deposition, a complexing agent is used to bind the metallic ions to avoid the homogeneous precipitation of the corresponding compound. The formation of a complex ion is essential to control the rate of the reaction and to avoid the immediate precipitation of the compound in the solution. The metal complex hydrolyses slowly to generate the positive ions in the solution. A solution containing the metal complexes was mixed with a solution that produces negative ions by hydrolysis. The deposition of the compound occurs when the ionic product exceeds the solubility product of the compound to be deposited. Either homogeneous or heterogeneous deposition can occur. The homogeneous process is the faster one, resulting in the adsorption of powdery ZnS particles on the substrate due to the bulk precipitation. So, the formation of metal complexes is essential to minimize the homogeneous process. In the heterogeneous process, due to the slow release of ions by the metal complexes, the preferential adsorption of Zn^{2+} and S^{2-} ions will take place, leading to uniform nucleation and growth of the thin film.

In the growth of the ZnS thin film from a chemical bath, hydrazine hydrate and ammonia act as the complexing agents to bind the Zn ions. Thiourea furnishes the necessary S^{2-} ions by hydrolysis. The various reactions involved in this growth process are given in Eqs. (3.11) – (3.19):

$$NH_3 + H_2O \Leftrightarrow NH_4^+ + OH^- \tag{3.11}$$

$$N_2H_4 + H_2O \Leftrightarrow N_2H_5^+ + OH^- \tag{3.12}$$

$$ZnCl_2 \rightarrow Zn^{2+} + 2Cl^- \tag{3.13}$$

$$Zn(NO_3)_2 \rightarrow Zn^{2+} + 2NO_3^- \tag{3.14}$$
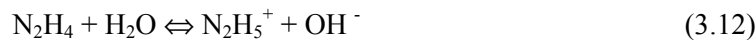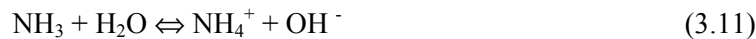
Zn^{2+} ions form the metal complexes with ammonia and hydrazine hydrate by the following reaction:

$$Zn^{2+} + 4NH_3 \Leftrightarrow Zn(NH_3)_4^{2+} \tag{3.15}$$

$$Zn^{2+} + 3(N_2H_4) \Leftrightarrow Zn(N_2H_4)_3^{2+} \tag{3.16}$$
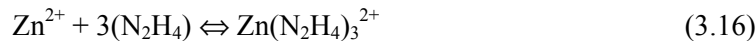
Hydrolysis of the thiourea can be represented by the chemical equation:

$$CS(NH_2)_2 + 2OH^- \Leftrightarrow S^{2-} + 2H_2O + CH_2N_2 \tag{3.17}$$

$$Zn^{2+} + S^{2-} \Leftrightarrow ZnS \tag{3.18}$$
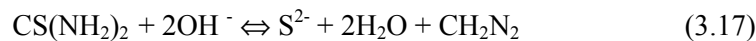
Assuming the metallic complex of the form ZnL_n^{2+}, where L is the complexing agent, the general reaction for the ZnS deposition can be represented as:

$$ZnL_n^{2+} + CS(NH_2)_2 + 2OH^- \rightarrow ZnS \text{ (substrate)}$$
$$+ nL + 2NH_3 + CH_2N_2 + 2H_2O \quad\quad (3.19)$$
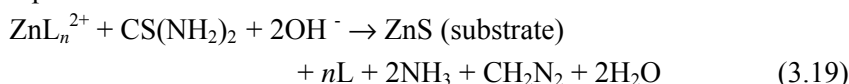
The presence of hydrazine hydrate during the deposition of ZnS improves the homogeneity and the film shows a smooth and reflecting surface [83]. In the presence of sufficient NH_3 and hydrazine hydrate, Zn^{2+} ions exist in the solution mainly as $Zn(NH_3)_4^{2+}$ and $Zn(N_2H_4)_3^{2+}$. The stability constant of the $Zn(NH_3)_4^{2+}$ complex is too high. But the presence of hydrazine in the solution helps part of this complex to exist as $Zn(NH_3)_3^{2+}$ which is having a low stability constant and will act as the major contributor of Zn^{2+} ions [87].

The pH value of the reaction mixture is controlled by the addition of NH_4OH. The addition of NH_4OH increases the presence of NH_3 in the solution and there by increases the concentration of metal complexes $Zn(NH_3)_4^{2+}$ and $Zn(N_2H_4)_3^{2+}$ (eqn 3.15). At the same time the addition of NH_4OH increases the OH^- ion concentration in the solution and thereby favours the hydrolysis (eqn 3.17) of the chalcogen precursor. The thickness of the as deposited ZnS thin film was found to increase when the pH value was varied from 10 to 10.6. The increase in thickness might be due to the increase in the concentration of Zn^{2+} and S^{2-} ions by the addition of NH_4OH, which favoured the heterogeneous growth of ZnS.

The addition of the ammonium salt increases the NH_4^+ concentration and thereby favours the backward reaction (eqn (3.11), resulting in more NH_3 and less OH^- ions in the chemical bath. The excess of ammonia will enhance the complex ion formation (eqn 3.15) where as the reduction in OH^- ion concentration will decrease the growth rate of ZnS formation (eqn 3.19). Therefore, the concentration of the ammonium salt has to be optimized for the heterogeneous and uniform growth of ZnS. In this work we have found that 0.5 N solution of the buffer salt gives more uniform and thicker films.

3C.4 Results and Discussion

3C.4.1 Structural analysis

The powder X-ray diffraction spectra of chemically deposited ZnS thin films showed no diffraction peaks corresponding to crystalline ZnS. The films deposited by the electron beam evaporation at different substrate temperatures showed only the peak corresponding to the (111) plane of cubic phase. This shows that the evaporated films are highly oriented with its (111) plane parallel to the substrate surface. Figure 3.15 shows the x-ray diffraction patterns of the chemically deposited and electron beam evaporated ZnS thin films together with that of ZnS powder. Considering the
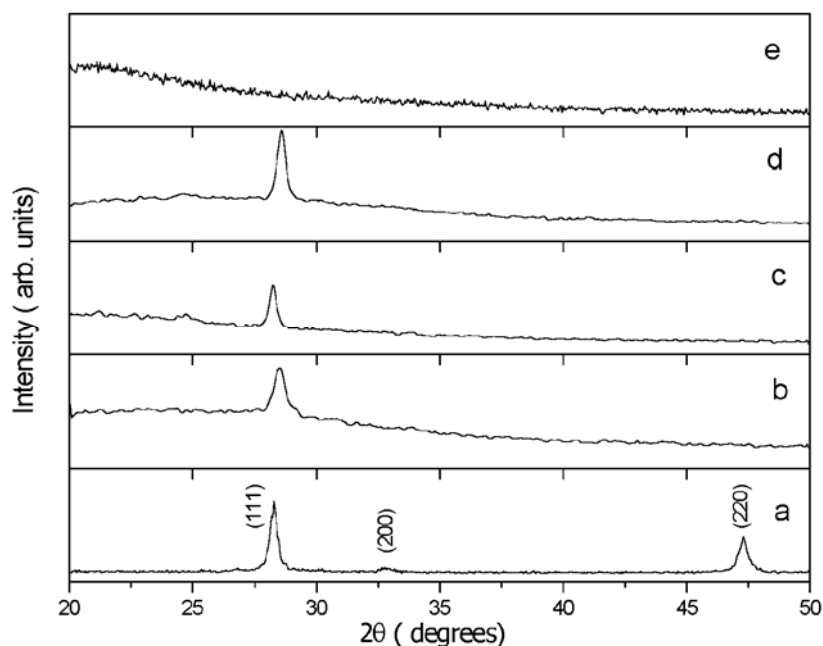
Fig.3.15 XRD patterns of the ZnS thin films (a) ZnS powder (b) ZnS by EBE at room temperature (c) EBE at substrate temperature 150^0 C (d) EBE at substrate temperature 300^0 C (e) ZnS by CBD

cubic structure of the ZnS, the lattice constant 'a' was determined from the X-ray diffraction data. The standard value of the lattice parameter 'a' of ZnS

86

is 5.406 A°. The grain sizes of the electron beam evaporated ZnS films were calculated from the XRD spectra using the Scherrer's formula. The lattice constant values and the average gain sizes of the ZnS prepared by the electron beam evaporation at various substrate temperatures are shown in table 3.4.

Table 3.4 The lattice constant and the grain sizes of the electron beam evaporated ZnS thin film

Substrate temperature	Plane (cubic)	Lattice constant (a) (A$^\circ$)	Grain size (nm)
28° C	111	5.42	17
150^0 C	111	5.47	27
300^0 C	111	5.40	24

3C.4.2 Optical properties

The transmission spectra of the ZnS thin films prepared from the zinc nitrate and zinc chloride solutions are shown in figure 3.16. The ZnS films prepared from the chemical bath containing nitrate solutions with pH = 10.6 showed transmission of more than 80 % in the visible region. Films were prepared for different pH values of the chemical bath keeping all other bath parameters same. The thickness of the ZnS film for constant dipping time was showing maximum value when the pH value of the bath was 10.6. The high transparency in the visible region is a consequence of the wide band gap of the film (3.86 eV). The low transparency of some samples as shown in figure3.16 might be due to adsorbed powdery colloids formed by homogeneous growth. Colloids degrade the quality of the films. Since ZnS is a direct band gap material, the band gaps of the ZnS films were calculated using the $(\alpha h\nu)^2$ against $h\nu$ plots (see section 2.3.5). The $(\alpha h\nu)^2$ against $h\nu$ plots of the ZnS films prepared from zinc nitrate and zinc chloride at different pH values are shown in figure 3.17. In the case of CBD films, band gap values varied
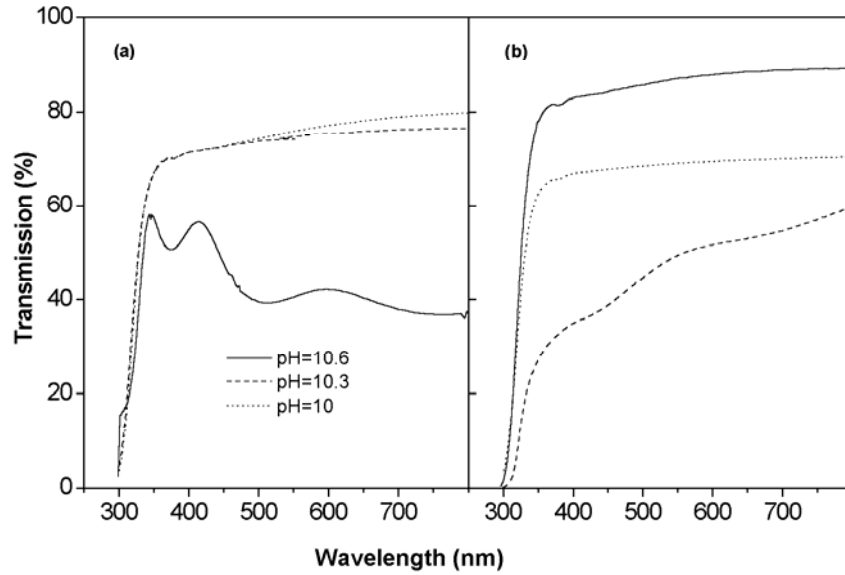
Fig.3.16 Transmission curves of CBD ZnS thin films deposited at different pH of the chemical bath: (a) Prepared from $ZnCl_2$, (b) prepared from $Zn(NO_3)_2$.
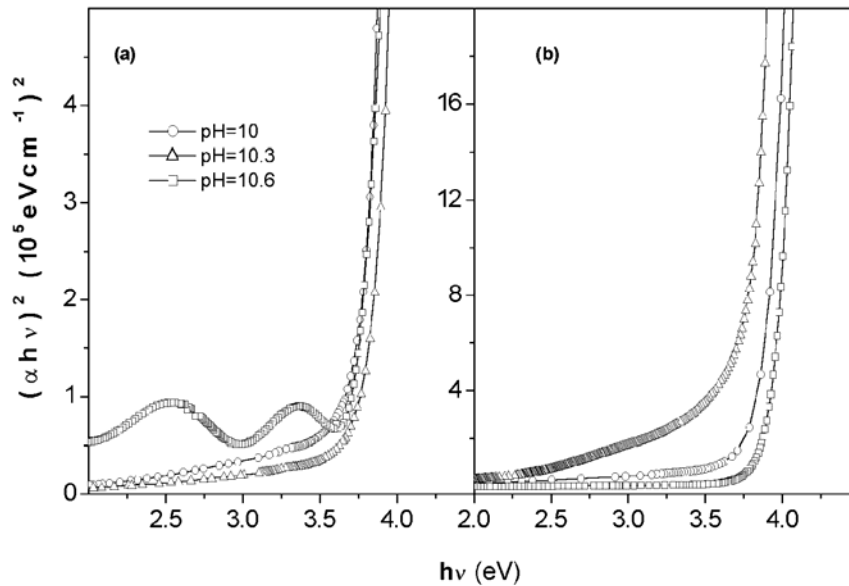
Fig.3.17 $(\alpha h\nu)^2$ against $h\nu$ plots of CBD ZnS thin films for different pH of the chemical bath: (a) Prepared from $ZnCl_2$, (b) prepared from $Zn(NO_3)_2$.

from 3.66 to 3.93 eV, which closely agree with the reported values [83,87].

The transmission spectra and the $(\alpha h\nu)^2$ against $h\nu$ plot of the electron beam evaporated ZnS film is shown in figure 3.18. The band gap of the electron beam evaporated film was found to be 3.42eV. The band gap values of the ZnS thin films with pH of the chemical bath are shown in table 3.5. The refractive index and the extinction coefficient of the as-deposited thin films were determined by the method described by Manificer et al. [93], assuming weak absorption by these films in the visible region (see section 2.3.5). The variation of the refractive index and the extinction coefficient of the as-deposited CBD ZnS films are shown in figure. 3.19. In the visible range of wavelength, the refractive index is 2.5.
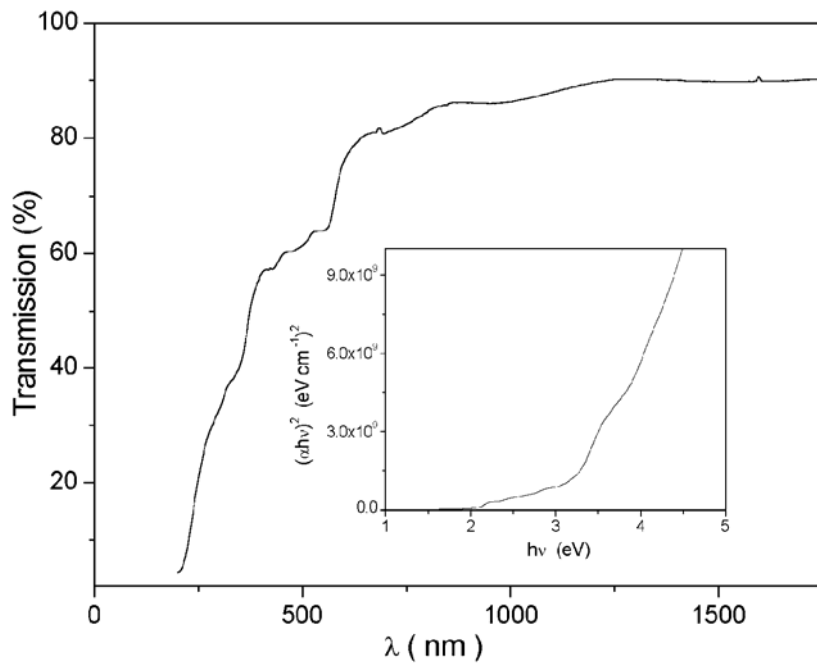
Fig.3.18 Transmission curve of electron beam evaporated ZnS thin film. The inset shows the $(\alpha h\nu)^2$ against $h\nu$ plot.

Table 3.5 Band gap values (in eV) of the CBD ZnS films

Prepared using	pH = 10	pH = 10.3	pH = 10.6
$ZnCl_2$	3.68	3.78	3.66
$Zn(NO_3)_2$	3.84	3.75	3.93
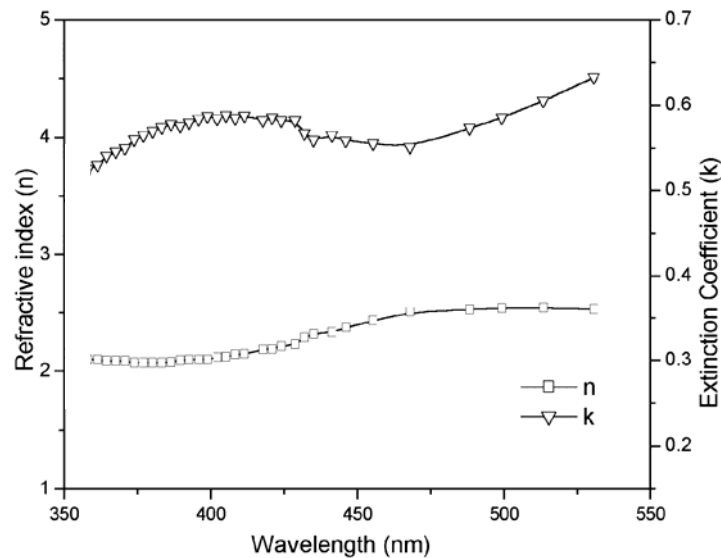
Fig.3.19 Variation of refractive index and extinction coefficient of CBD ZnS films deposited from a bath containing $ZnCl_2$ for a pH value of 10.6.

3C.4.3 Electrical properties

The resistivity of the ZnS films was found to vary considerably with the pH of the chemical bath, as shown in figure 3.20 a. The resistivity of the films reduced from ~10^6 to ~10^4 Ωcm; when the pH varied from 10 to 10.6. The addition of ammonia produces more zinc complexes in the bath and also favours the hydrolysis of thiourea, resulting in a more uniform growth of ZnS films of low resistivity. The variation of resisitivity of the electron beam evaporated ZnS films with the substrate temperature is shown in figure 3.20b.
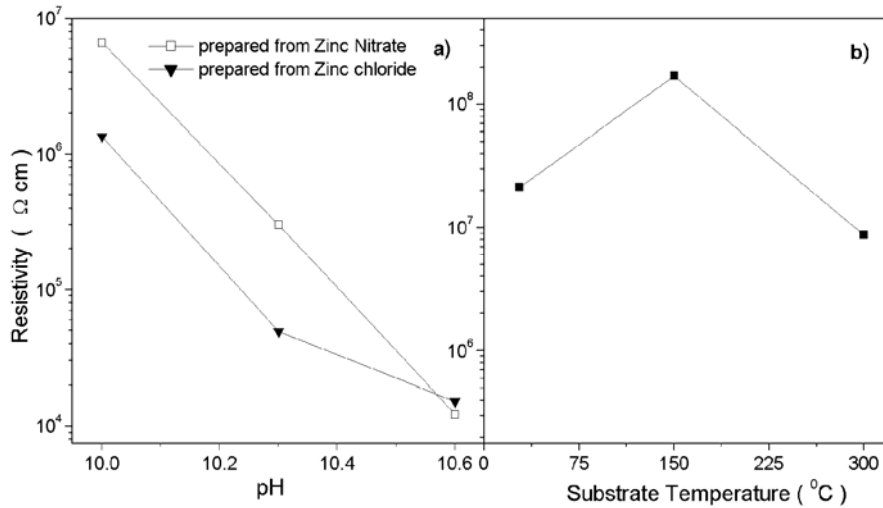
Fig.3.20 The Resistivity of the ZnS thin films (a) deposited under various pH of the chemical bath (b) prepared by electron beam evaporation at different substrate temperatures.

deposited by thermal evaporation on the ZnS films prepared by CBD over the ITO substrates. An impedance analyzer (model HP 4192A) was sued to measure the capacitance of the films at various frequencies. From the capacitance value, the dielectric constants of the films in the frequency range 1 – 9 MHz were found out. The dielectric constant was found to be around 6. Figure 3.21 shows the dependence of dielectric constant on frequency for the ZnS films prepared by chemical bath deposition. This value of dielectric constant closely agrees with that of evaporated [94] stoichiometric ZnS films.
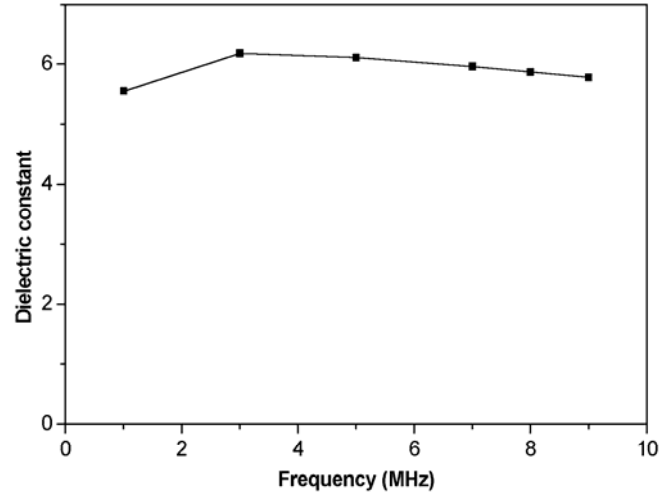
Fig.3.21 Dielectric constants of the chemical bath deposited ZnS thin films

3C.5 Conclusion

ZnS thin films were prepared by chemical bath deposition from two zinc salts, viz. zinc nitrate and zinc chloride. The optical and electrical properties of CBD ZnS films are in agreement with that of electron beam evaporated ZnS films. The optical and electrical properties of the as- deposited ZnS thin films were found to vary with the pH value of the reaction mixture. The films prepared from a chemical bath containing a zinc nitrate solution with pH = 10.6 showed a transmission of more than 80 % in the visible region. The ZnS films produced from the zinc nitrate precursor have found to be more transparent and smooth compared to the films grown from the zinc chloride precursor. The presence of the buffer ammonium salt in the solution along with hydrazine increases the ZnS deposition rate. The refractive index of the film was around 2.5 in the visible region. The ZnS films deposited at a pH = 10.6 showed a resistivity of $\sim 10^4$ Ωcm. The band gap of the films varied from 3.66 to 3.93 eV. The wide band gap of these films makes it possible to use them as buffer layer for solar cells.

Part D

ZnO thin films prepared by the thermal oxidation of chemical bath deposited ZnS films

ZnS thin films prepared by the chemical bath deposition were thermally oxidized into ZnO films by annealing in air at 800^0 for one hour. The thermal conversion of the ZnS to ZnO is analysed using XRD. The oxidized films show an optical band gap of 3.23 eV and an electrical resistivity of $10^4 \Omega cm$.

3D.1 Introduction

The high efficiency heterojunction solar cell devices nowadays utilize an oxide bilayer (see Chapter1, Fig 1.6) that consists usually of a thin (50-100 nm) high-resistivity layer, and a thicker (100-1500 nm) low-resistivity layer. The high resistivity layer is most often undoped ZnO. The conducting part of the oxide bilayer is most often ZnO doped with either Al, B or Ga. Tin doped indium oxide (In_2O_3:Sn, ITO) is also widely used. The purpose of this high resistive ZnO layer is to increase the open circuit voltage (V_{OC}) by decreasing the dark saturation current [95]. The transparent conducting oxide layer serve as low resistance contact to the cell and also as an antireflection coating for the active region.

In this section a simple and low cost technique for the preparation of ZnO films from the chemical bath deposited ZnS films is discussed. The chemical bath deposited ZnS thin films were thermally oxidized to ZnO films by annealing in air and oxygen ambient.

3D.2 ZnO thin films

ZnO thin films with their wide band gap (3.37 eV) at room temperature are of great interest due to the applications such as ultraviolet emitting devices, transparent conductors and ultra fast nonlinear optical devices in optoelectronics [96]. In the last few years zinc oxide has gained increasing attention as a transparent conducting oxide (TCO) material because of its higher abundance compared to the other TCO materials. Another advantage of the zinc oxide is its better stability in hydrogen plasma than that of Indium Tin oxide, which makes it useful in the fabrication of hydrogenated amorphous silicon solar cells [97]. The ZnO thin films have been grown by different techniques such as magnetron sputtering [98], chemical vapour deposition [99], sol-gel method [100], pulsed laser deposition [101], spray pyrolysis [102] etc.

In the case of solar cells, the ZnO resistive layer is usually prepared by sputtering in Ar/O$_2$ (about a partial pressure of 0.1–2 %) ambient [95,33,34]. Besides sputtering intrinsic ZnO, the resistive layer may also be made from a doped target (ZnO:2 wt.% Al$_2$O$_3$), provided that the sputtering ambient contains enough oxygen. The films are usually sputtered in pure Ar ambient and in some cases relatively small amount of O$_2$ is also introduced for better crystallinity.

Preparation of ZnO thin films by the thermal conversion of the crystalline ZnS thin films deposited by MOCVD [103] and PLD [104] has been reported earlier. The formation of ZnO thin films with high photoconductivity [82,89] and waveguiding applications [92] was reported by the thermal oxidation of chemical bath deposited ZnS films. The possibility of doping Ga during thermal oxidation of ZnS to increase the electrical conductivity was also reported by Jayatissa [105]. The ZnO films formed by the thermal oxidation of ZnS were always showing wurtzite structure.

3D.3 Experimental details

ZnS thin films were deposited on quartz substrates by chemical bath deposition (as described in Section 3C.3) using the zinc nitrate solution at a pH = 10.3. The thermal oxidation of the ZnS thin films was investigated by annealing the ZnS films at different temperatures in air and under oxygen ambient. The annealing temperature was varied from 400 to 800^{0}C.

The structure of the films was investigated using X-ray diffraction. The optical properties of the as-deposited ZnS and the annealed samples were compared using the transmission spectra. The transmission spectra of the samples were recorded using UV-Vis-NIR spectrophotometer (Hitachi 3410). The electrical resistivity of the samples was calculated from the current voltage measurements using the Keithley source measure unit (SMU 236). Two probe measurements were made in the planar electrode configuration with highly conducting silver paint as the electrodes.

3D.4 Results and discussion

The XRD spectra of the films annealed at different temperatures show that the thermal conversion to ZnO was not complete below 800^0C. It has been reported earlier that in the case of thermal oxidation of crystalline ZnS films prepared by the MOCVD, annealing in oxygen ambient below 700^0C showed mixed phases with reflections corresponding to the cubic ZnS and hexagonal ZnO [103]. In the present study, the annealing of ZnS films at 800^0C was the optimum temperature for the complete conversion of the ZnS to ZnO (Fig.3.22). This was confirmed by the absence of sulphur atoms in the EDX analysis of converted ZnO films. The electron beam evaporated crystalline ZnS films and the powder samples were also annealed in the same conditions to find out the exact processes behind the thermal oxidation.
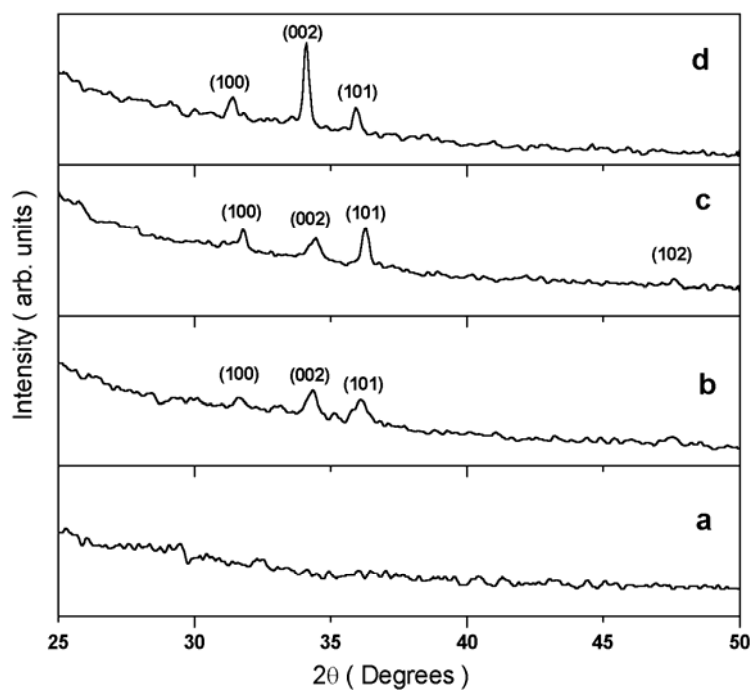
Fig.3.22 The XRD spectra of the ZnO films prepared by the thermal oxidation of CBD ZnS at 800^0C. (a) as-deposited CBD ZnS thin film (b) annealed in air for 1 hour (c) annealed in O_2 for 1 hour (d) annealed in air for 3 hours.

3D.4.1 Structural changes during thermal oxidation

The as deposited ZnS films by CBD were found to be amorphous by X-ray. The film annealed in air at 800^0C for one hour shows peaks corresponding to (100), (002) and (101) planes of the hexagonal ZnO phase. The crystallinity of the films improved, when the annealing was carried out in oxygen flow. The films annealed in air at 800^0C for longer duration (3hrs) show polycrystalline nature of the films with a relatively strong textured orientation along the (002) plane. Figure 3.22 shows the XRD spectra of the films annealed at various conditions. The lattice constants of the thermally converted ZnO films (Table 3.6) were found to be consistent with the standard values; a $=3.2539A^0$ and c $= 5.2098A^0$ [95].
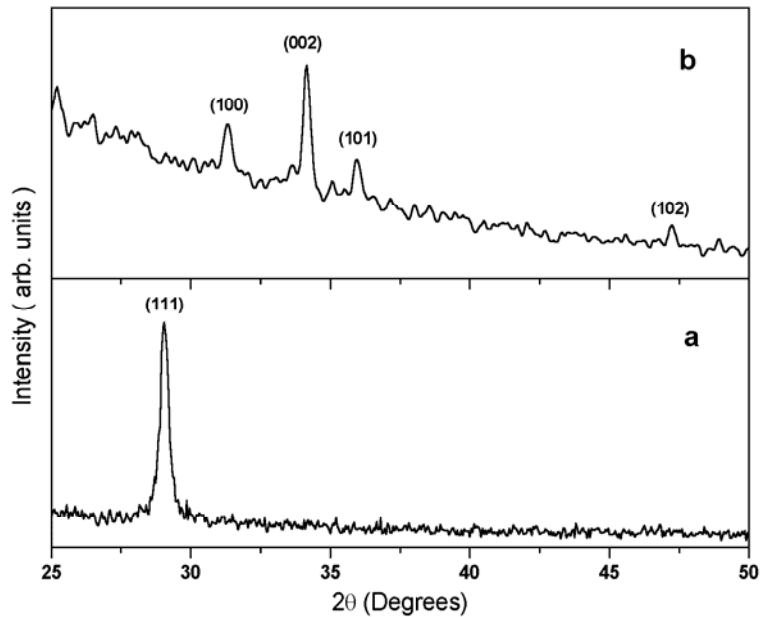
Fig.3.23 XRD spectra of EBE ZnS (a) as deposited (b) after annealing in O_2 for 1hour at 800^0C

ZnS powder and crystalline ZnS films prepared by electron beam evaporation were also annealed in oxygen ambient at 800^0C for one hour.

The electron beam evaporated ZnS films showed only a strong reflection corresponding to the (111) plane of the cubic zinc blend structure. After the oxidation, the converted films showed the peaks corresponding to the (100), (002), (101) and (102) reflection of the hexagonal wurtzite structure of the ZnO (Fig.3.23). These films showed a preferred orientation along the (002) plane just like in the case of the thermally converted CBD ZnS (Fig. 3.22 and 3.23). The XRD patterns of the ZnS powder before and after oxidation are shown in figure 3.24. The XRD spectrum of the thermally oxidised ZnS powder is similar to that of the ZnO powder as shown in figure 3.24.

Table 3.6 Lattice constants and the grain sizes of ZnO prepared by the oxidation of various precursors

Precursor	Annealing at 800^0C	a (A^0)	c (A^0)	Grain size (nm)
CBD ZnS	Air ,1 hr	3.26	5.23	14
CBD ZnS	O_2 ,1 hr	3.25	5.20	15
CBD ZnS	Air , 3 hrs	3.28	5.25	31
EBE ZnS	O_2 ,1 hr	3.28	5.25	25
ZnS powder	O_2 ,1 hr	3.27	5.25	26

The XRD pattern of the converted ZnO in the Fig 3.22d indicates hexagonal wurtzite structure with a preferential (002) orientation. When the duration of annealing increased, the diffraction peaks became sharper and more intense due to the increased particle size as well as the enhanced crystallinity. The mean grain sizes of the films (Table 3.6) were calculated by the Scherrer's formula. The average grain sizes of the thermally oxidized EBE-ZnS and ZnS powder were around 25 nm. In the case of CBD-ZnS, the films after oxidation showed an average grain size of 14 nm for air-annealed sample and 16 nm for those annealed in oxygen flow. The grain size increased to 31nm when the duration of the annealing increased to 3hrs indicating better crystallinity
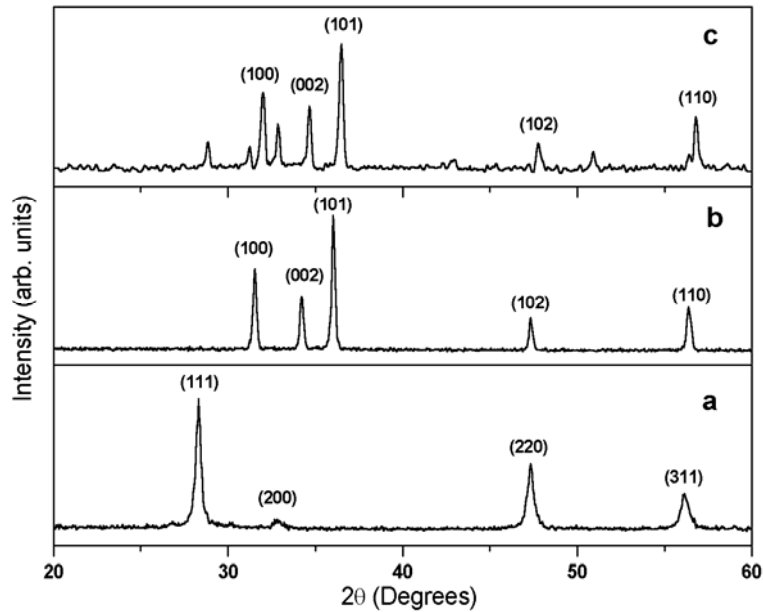
Fig. 3.24 XRD spectra of (a) ZnS powder (b) ZnS powder annealed in O_2 at 800^0C for 1h (c) ZnO powder

3D.4.2 Physical process of thermal oxidation

The possible oxidation process of the ZnS might be due the diffusion of the oxygen atoms into the ZnS matrix via interstitial sites and bond to Zn, forcing the sulphur atoms to occupy the interstitial sites and get oxidized to escape as SO_2. This will transform the unitcell and it recrystallises to the stable wurtzite structure. The possibility of the direct occupation of the sulphur sites of the cubic ZnS by the oxygen atoms can be ruled out since that can form only a zinc blend ZnO, which was not observed in the present study by XRD analysis. In our experiment both the amorphous and the crystalline ZnS were oxidized in the same manner resulting in the wurtzite ZnO structure. Since the unit cell volume of the hexagonal ZnO is less than that of cubic ZnS, the relaxation of the structure will be favored to attain the more stable wurtzite structure.

3D.4.3 Optical and Electrical Properties

The optical transmission spectra of the as-deposited and oxidized films are shown in figure 3.25. The band gap values of the films were calculated from the extrapolated intercept of the straight-line portion of $(\alpha h\nu)^2$ against hν plot on to the energy axis (see section 2.3.5) as shown in the inset of Fig. 3.25. The chemical bath deposited ZnS films have a band gap of 3.75eV and EBE-ZnS has a band gap of 3.42eV. The ZnS film shows a band gap of 3.23eV after the thermal oxidation.
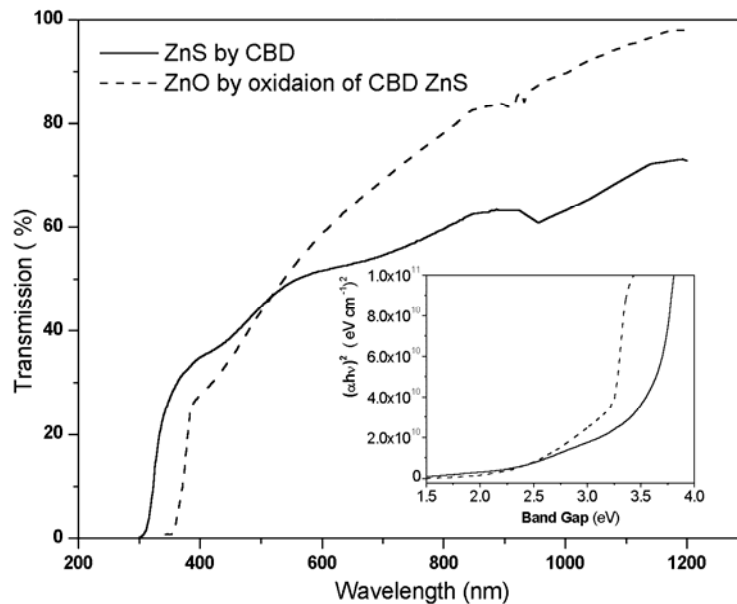
Fig.3.25 Transmission spectra of the CBD ZnS as deposited and after oxidation. The inset shows the respective $(\alpha h\nu)^2$ against hν curves

The CBD ZnS films in the present study showed an average transmission less than 50% in the visible region, which is less compared to the EBE ZnS (see section 3.15.2). The ZnO films obtained by the thermal oxidation of these ZnS films showed an average transmission above 55% in the visible region indicating that the thermally converted ZnO is more transparent compared to the as-deposited films. Better transparent ZnO film may be

obtained if more transparent ZnS films are used for oxidation. The SEM micrograph of the ZnO film prepared by the thermal oxidation technique was rather rough and has micro pores (Fig. 3.26). The roughness may be the reason for the reduced transmission of ZnO films prepared by the thermal oxidation of CBD ZnS films.

The chemical bath deposited ZnS films show a high resistivity of 6.6×10^6 Ωcm. The resistivity of these films reduced considerably to 1.05×10^4 Ωcm after the thermal oxidation to ZnO. The high resistivity of the thermally converted ZnO films implies that films are nearly stoichiometric. The ZnO films prepared without any intrinsic or extrinsic dopants will show a very high resistivity [107]. The ZnO films prepared by the thermal oxidation of CBD ZnS films might be having very low lattice defects such as oxygen vacancies or zinc interstitials, which accounts for the high resistivity of these films.
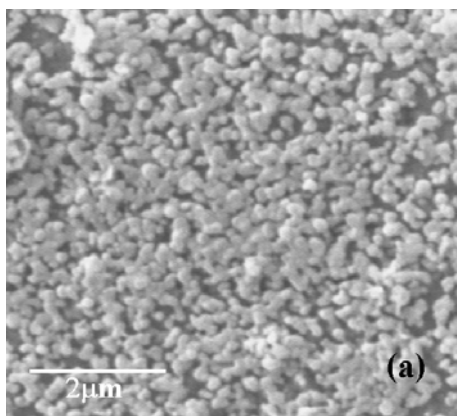
Fig.3.26 SEM micrographs of ZnO thin film prepared by the thermal oxidation of CBD ZnS.

3D.5 Conclusion

ZnO thin films with hexagonal wurtzite structure was prepared by the thermal oxidation of the chemical bath deposited ZnS thin films. The air annealing of the samples at 800^0C for one hour resulted in the complete

conversion of the ZnS to ZnO, which was confirmed by the XRD and EDX measurements. The physical process of oxidation of the CBD ZnS was compared with that of EBE ZnS and ZnS powder using the XRD studies. The high electrical resistivity (1.05 x 10^4 Ωcm) of the converted ZnO indicates an intrinsic growth of the ZnO film. The ZnO films showed an average transmission above 55% in the visible region and an optical band gap of 3.23eV.

References

[1] U. Rau and M. Scmidt, Thin Solid Films 387 (2001) 141

[2] U. Rau, A. Jasenek, H.W. Schock, F. Engelhardt and Th. Meyer, Thin Solid Films 361-362 (2000) 298

[3] U. Rau, M. Schmidt, A. Jasenek, G. Hanna and H.W. Schock, Sol. Energy Mater. Sol. Cells 67 (2001) 137

[4] D. Schmid, M. Ruckh and H.W. Schock, Sol. Energy Mater. Sol. Cells 41-42 (1996) 281

[5] M.A. Contreras, M.J. Romero, B. To, F. Hasoon, R. Noufi, S. Ward and K. Ramanathan, Thin Solid Films 403-404 (2002) 204

[6] K.B. Ozanyan, J.E. Nicholls, L.Mary, J.H.C. Hogg, W.E. Hagston, B.Lunn and D.E. Ashenford, Solid State Commun. 99 (1996) 407

[7] H.C. Chou and A.R. Ohatgi, J. of Electron. Mater. 23 (1994) 31

[8] A.I. Olivia, R.C. Rodriguez, O.S. Canto, Victor Sosa, P.Quintana and J.L. Pena, Appl. Surf. Sci. 205 (2003) 56

[9] H.R. Moutinho, D. Albin, Y.Yan, R.G. Dhere, X. Li, C.Perkins, C.S. Jiang, B.To and M.M. Al-Jassim, Thin Solid films 436 (2003) 175

[10] S.A. Al Kuhaimi, Vacuum 51 (1998) 349

[11] P.J. Sebastian and M.E. Calixto, Thin Solid Films 360 (2000) 128

[12] U. Pal, R.S. Gonzalez, G. M. Montez, G.G. Jimenez, M.A. Vidal and Sh. Torres, Thin Solid films 305 (1997) 345

[13] S.A. Mahaoud, A,A. Ibrahim and A.S. Riad, Thin Solid Films 372 (2000)144

[14] K.E. Assali, M. Boustani, A. Khiara, T. Bekkay, A. Outzourthit, E.L. Ameziane, J.C.Bernard and J.Pouzet, Phys.Stat.Solid.(a) 178 (2000) 701

[15] H. Sakai, T. Tamaru, T. Sumomogi, H. Ezumi and B. Ullrich, Jpn. J. Appl. Phys., 37 (1998) 4149

[16] K.P. Varkey and K.P. Vijayakumar, Jpn. J. Appl. Phys. 36 (1997) L394

[17] N.A. Zeenath, K.P. Varkey and K.P. Vijayakumar, J. Phys.: Condens. Matter. 10 (1998) 2053

[18] J.N. Ximello-Quiebras, G. Contreras-Puente, J.Aguilar-Hernandez, G,Santana-Rodriguez and Arias Carbajal Readigos, Sol. Energy Mater. Sol. Cells 82(2004) 263

[19] H. Zhang, X. Ma and D. Yang, Mater. Lett. 58(2003) 5

[20] J.P. Enriquez and X.Mathew, Sol.Energy Mater.Sol.Cells 76 (2003) 313

[21] H. Metin and R. Esen, Semicond. Sci.Technol. 18 (2003) 647

[22] J.Herrero, M.T.Gutierrez, C.Guillen, J.M. Dona, M.A. Martinez, A.M. Chaparro and R. Bayon, Thin Solid Films 361-362 (2000) 28

[23] P. O`Brien and T. Saeed, J. Cryst. Growth 158 (1996) 497

[24] K.S. Ramaiah, R.D. Pilkington, A. E.Hill, R.D. Tomlinson and A.K. Bhatnagar, Mater. Chem. and Phys. 68 (2001) 22

[25] G. Sasikala, R. Dhanasekaran, C. Subramanian, Thin solid films 302 (1997) 71

[26] R.C. Rodriguez, A.I. Oliva, Victor Sosa, F.C. Briones and J.L. Pena, Appl. Surf. Sci. 161 (2000) 340

[27] P. Garg, A. Garg, A.C. Rastogi and J.C. Garg, J. Phys. D: Appl. Phys. 24 (1991) 2026

[28] C.X. Qiu and I. Shih, Can. J. Phys. 65 (1987) 1011

[29] S.N. Sahu, R.D.L. Kristensen and D. Haneman, Sol. Energy Mater. 18 (1989) 385

[30] L. Stolt, J. Hedstrom, J. Kessler, M. Ruckh, K-O. Velthaus and H.W. Schock, Appl. Phys. Lett. 62 (1993) 597

[31] V.K. Kapur, B.M. Basol and E.S. Tseng, Sol. Cells 21 (1987) 65

[32] S.N. Qiu, L. Li, C.X. Qiu, I. Shih and C.H. Champness, Sol. Energy Mater. Sol. Cells 37 (1995) 389

[33] J. Hedstrom, H. Ohlsen, M. Bodegard, A. Kylner, L. Stolt, D. Hariskos, M. Ruckh and H.W. Schock, in Proc. 23rd IEEE Photovolt. Spec. Conf. (Louisville, KY, 1993) p364

[34] D. Schmid, M. Ruckh, F. Grunwald and H.W. Schock, J. Appl. Phys., 73 (1993) 2902

[35] A.Rockett and R.W. Birkmire, J. Appl. Phys. 70 (1991) R81

[36] Y. Sudo, S. Endo and T. Irie, Jpn. J. Appl. Phys. 32 (1993) 1562

[37] H.W. Schock and R. Noufi, Prog. Photovolt.: Res. Appl. 8 (2000) 151

[38] R.W. Birkmire and E. Eser, Annu. Rev. Mater. Sci. 27 (1997) 625

[39] K. Ramanathan K, M.A. Contreras, C.L. Perkins, S. Asher, F.S. Hasoon, J. Keane, D. Young, M. Roberto, W. Metzger, R. Noufi, J. Ward, A. Duda, Prog. Photovolt.: Res. App., 11 (2003) 225

[40] L. Kronik, U. Rau, J.-F Guillemoles, D. Braunger, H.W. Schock and D. Cahen, Thin Solid Films 361-362 (2000) 353

[41] C. Heske et al., Appl. Phys. Lett. 74 (1999) 1451

[42] T. Nakada and A. Kunioka, Appl. Phys. Lett., 74 (1999) 2444

[43] S. Chaisitsak, A. Yamada and M. Konagai, Jpn. J. Appl. Phys. 41 (2002) 507

[44] P. Nemec, I. Nemec, P. Nahalkova,Y. Nemcova, F. Trojanek and P. Maly, Thin Solid Films 403-404 (2002) 9

[45] C.M. Lampert, Sol. Energy Mater. Sol. Cells 32 (1994) 307

[46] T. J. Bukowski and J.H. Simmonson, Critical Rev. in Solid State and Mater. Sci., 27(2002)119

[47] H. Mathieu, T. Richard, J. Allegre, P. Lefebvre and G. Arnaud, J. Appl. Phys. 77 (1995) 287

[48] K.K. Nanda, S.N. Sarangi, S. Mohanty and S.N. Sahu, Thin Solid Films 322 (1998) 21

[49] K.B.Jinesh, C.Sudha kartha and K.P.Vijayakumar, Appl. Surf. Sci. 207 (2003) 26

[50] A.Cortes, H.Gomez, R.E. Marotti, G.Reveros and E.A. Dalchiele, Sol.Energy Mater. Sol.Cells 82 (2004) 21

[51] B.K. Patel, K.K. Nanda and S.N. sahu, J.Appl. Phys. 85 (1999) 3666

[52] O.V. Salata, P.J. Dobson, P.J. Hull and J.L. Hutchinson, Thin Solid Films 251 (1994) 1

[53] T.L.Chu, ShirleyS.Chu, N.Schultz, C.Wang and C.Q.Wu, J.Electrochem.Soc. 139 (1992) 2443

[54] R.Ramirez-Bon, N.C. Sandoval-Inda, F.J. Espinoza-Beltran, M.Sotelo-Lerma, O Zelaya_Angel and C.Falcon, J.Phys.Condens.Matter 9 (1997) 10051

[55] D.Lincot, M. Froment, H. Catchet, in: (Eds) R.C. Alkair, D.M. Kolb, Advances in Electrichemical Science and Engineering, 6 (Wiley-VCH, Weinheim, 1999) 165

[56] P.N.Gibson, M.E. Ozsan, D.Lincot, P.Cowache, D.Summa, Thin Solid Films 361-362 (2000) 34

[57] M.A. Martinez, C.Guillen and J.Herrero, Applied Surface Science 140 (1999) 182

[58] J. Touskova, D.Kindl, L.Dobiasova, J. Tousek, Solar Energy Mater.& Sol. Cells 53 (1998) 177

[59] S.Gosh, A.Mukherjee, Hyunsoo Kim and Chongmu Lee, Materials Chemistry and Physics 78 (2003) 726

[60] G.C.De, A.M.Roy, S.Saha and Sukumar Aditya, J.Indian Chem.Soc., 80 (2003) 551

[61] Y.Wang and N.Herron, J.Phys.chem. 95 (1991) 525

[62] G.C. Morris and R. Vanderveen, Sol. Energy Mater. Sol. Cells 26 (1992) 217

[63] W.E. Devaney, W.S. Chen, J.M. Stewart and R.A. Mickelsen, IEEE Trans. Electron. Dev. 37 (1990) 428

[64] B.M. Basol, V.K. Kapur, G. Norsworthy, A. Halani, C.R. Leidholm and R.Roe, Electrochem. Solid-State Lett. 1 (1998) 252

[65] J. Torres, G. Gordillo, Thin Solid Films 207 (1992) 231

[66] P.J. Sebastian, O. G. Dasa and P.K. Nair, J. Phys. D: Appl. Phys. 25 (1992) 1848

[67] A.Olea and P.J. Sebastian, Sol. Energy Mater. Sol. Cells 55 (1998) 149

[68] K. Subbbaramaiah and V.S. Raja, Sol. Energy Mater. Sol. Cells 32 (1994) 1

[69] K.T.R. Reddy and P.J. Reddy, Thin Solid Films 253 (1994) 238

[70] S.A. Telfer, C. Morhain, B. Urbaszek, C. O'Donnell, P. Tomasini, A. Balocchi, K.A. Prior and B.C. Cavenett, J. Cryst. Growth 214/215 (2000) 197

[71] M. A. Naby, A. Zekry, F.E. Akkad and H.F. Ragaie, Sol. Energy Mater. Sol. Cells 29 (1993) 97

[72] R. L. Call, N.K. Jaber, K. Seshan, J.R. Whyte, Sol Energy Mater. 21 (1990) 373

[73] L.P. Deshmukh, C.B. Rotti, K.M. Garadkar, G.S. Shahane, Ind. J. Pure Appl. Phys. 36 (1998) 322

[74] G.K. Padam, G.L. Malhotra, S.U.M. Rao, J. Appl. Phys. 63 (1988) 770

[75] M.R.Rajebhonsale and S.H.Pawar, Ind. J.Pure Appl.Phys. 20 (1982) 652

[76] N.C. Sharma, R.C. Kainthala, D.K. Pandya and K.L. Chopra, Thin Solid Films 60 (1979) 55

[77] J.-H. Lee, W.-C. Song, K.-J. Yang and Y.-S. Yoo, Thin Solid Films 416 (2002) 184

[78] J.M. Dona and J. Herrero, Thin Solid Films 268 (1995) 5

[79] D.S. Boyle, O. Robbe, D.P. Halliday, M.R. Heinrich, A. Bayer, P. O'brien, D.J.Otway and M.D.G. Potter, J. Mater. Chem. 10 (2000) 2439

[80] M.S.Abrahams and C.J. Buiocchi, J. Electrochem. Soc. 135 (1988) 1578

[81] M.A. Contreras, B. Egaas, D. King, A. Schwartzlander and T. Dullweber, Thin Solid Films 361-362 (2000)

[82] O.L.Arenas,M.T.S.Nair,P.K.Nair,Semicond.Sci.Technol.12 (1997)1323.

[83] J.M. Dona, J. Herrero, J. Electrochem. Soc. 141 (1994) 205

[84] J. Cheng, D.Fan, H. Wang, B. W. Liu, Y. C. Zhang and H. Yan, Semicond. Sci. Technol. 18 (2003) 676

[85] D.A. Johnson, M.H. Carletto, K.T.R. Reddy, I. Forbes and R.W. Miles, Thin Solid films 403-404 (2002) 102

[86] J.Vidal, O.de.Melo, O.Vigil, N.Lopez, G. Contreras-Puente, O.Zelaya-Angel, Thin Solid Films 419 (2002) 118

[87] I.O. Oladeji, L. Chow, Thin Solid Films 339 (1990) 148

[88] P. O`Brien, D. J. Otway, D. Smyth-Boyle, Thin Solid Films 361-362 (2000) 17

[89] A.M. Fernandez, P.J. Sebastian, J. Phys. D 26 (1993) 2001

[90] T. Nakada, M. Mizutani, Y. Hagiwara, A. Kunioka, Solar Energy Mater. Solar Cells 67 (2001) 255

[91] T. Nakada and M. Mizutani, in: Proc. 28th IEEE Photovolt. Spec. Conf. (Anchorage, AK, 2000) p529

[92] E.J.Ibanga, C.Le Luyer and J.Mugnier,Mater.Chem. Phys.30 (2003) 490

[93] J.C.Manifacier, J.Gasiot, J.P.Fallard, J.Phys. E **9** (1976) 1002

[94] A. Goswami and Amit P Goswami, Thin Solid Films **16** (1973) 175

[95] W.N. Shafarman, R. Klenk and B.E. McCandless, J. Appl. Phys. 79 (1996) 7324

[96] G.H. Lee, T. Kawazoe, M. Ohtsu, Solid State Communications 124 (2002) 163

[97] C. Beneking et. al., Thin Solid Films, 351 (1999) 241

[98] A.Moustaghfir, E. Tomasella, S. Ben Amor, M. Jacquet, J. Cellier and T. Sauvage, Surf. Coat. Technol. 174-175 (2003) 193

[99] M. Purica, E. Budianu, E. Rusu, M. Danila and R. Gavrila, Thin Solid films 403-404 (2002) 485

[100] D. Bao, H. Gu and A. Kuang, Thin Solid Films 312(1998) 37

[101] J.F. Muth, R.M. Kolbas, A.K. Sharma, S. Okytyabrsky and J. Narayan, J. Appl. Phys. 85(1999) 7884

[102] Y. Chen, D.M. Bagnall, Z. Zhu, T. Sekiuchi, K. Park, K. Hiraga, T. Yao,S.Koyama, M.Y.Shen and T.J.Goto, J.Cryst.Growth 181(1997) 165

[103] X.T.Zhang, Y.C.Liu, L.G.Zhang, J.Y.Zhang, Y.M.Lu, D.Z.Shen,W. Xu, G.Z. Zhong, X.W. Fan and X.G. Kong, J. Appl. Phys. 92 (2002) 3293

[104] Y.Z.Yoo, M.Kawasaki, H.Koinuma et.al.,Appl.Phys.Lett. 78 (2001) 616

[105] A.H. Jayatissa, Semicond. Sci. Technol. 18 (2003) L27

[106] JCPDS-ICDD 80-0075

[107] K. Ellmer, J. Phys. D: Appl. Phys 34 (2001) 3097

CHAPTER 4

I-III-VI$_2$ Chalcopyrite thin films for solar cells

Part A

Preparation and characterisation of CuInSe₂ thin films by flash evaporation

Polycrystalline CuInSe₂ thin films were prepared by flash evaporation followed by the selenisation at 350⁰ C. The films showed chalcopyrite structure with a strong preferred orientation along (112) plane. The electrical and optical properties of the as deposited and the annealed CuInSe₂ films with various Cu/In ratios in the starting material were studied. The flash evaporated CIS films were found to be p-type. The selenisation improve the stoichiometry of the films by compensating the selenium loss during flash evaporation thereby modifying the electrical and optical properties of the films.

4A.1 Introduction

The efficiency of a solar cell is strongly dependent on the amount of incident light absorbed by the material. It is desirable for a material to absorb as much light as possible over a wide energy range. Secondly the material properties should be such that the photo excited electrons and holes can be collected by the internal field and pass into the external circuit before they recombine. The crystal structure of $CuInSe_2$ and the defect physics are determinant of the above mentioned device characteristics. An understanding of the reaction kinetics is also crucial for the fabrication of absorber films that will meet the above-mentioned requirements. Growth of undesirable secondary phases during the formation of the absorber layer is known to adversely affect the solar cell device. The crystallographic structure, the phase diagram and the material properties of the $CuInSe_2$ thin films are precisely explained and the different deposition techniques for the $CuInSe_2$ thin films are reviewed. Preparation of $CuInSe_2$ thin films by the flash evaporation, followed by the selenisation is discussed in this part of the thesis.

4A.2 Crystallography of CuInSe₂

$CuInSe_2$ belong to the semiconducting I-III-VI₂ materials family that crystallize in the tetragonal chalcopyrite. The tetragonal structure of $CuInSe_2$ (Fig. 4.1) results from the stacking of two cubic zinc blend structures along the z-axis. The primitive cell for this structure is made up of eight tetrahedrons with shared vertices, so that the whole cell is just two stacked cubic structures. By convention, the short edge is labeled *a* and the long edge is labeled *c*. This gives rise to the condition that, given perfect tetragonal symmetry, c/a =2.

A chalcopyrite primitive cell contains three different atoms, two cations (A and B) and one anion (C). If these are arranged so that each C anion has two A cations and two B cations as nearest neighbours, the resulting structure is chalcopyrite. In $CuInSe_2$, each group I (Cu) or group III (In) atom has four

bonds to the group VI atom (Se). In turn each Se atom has two bonds to Cu and two to In. The tetrahedral structure becomes distorted due to differing bond strength between I-VI and III-VI atoms, so the value of c changes relative to a. The measure of this distortion can be described by the quantity, $(2-c/a)$. For CuInSe$_2$, the lattice parameters are, $a = 0.5789$ nm and $c = 1.162$ nm.
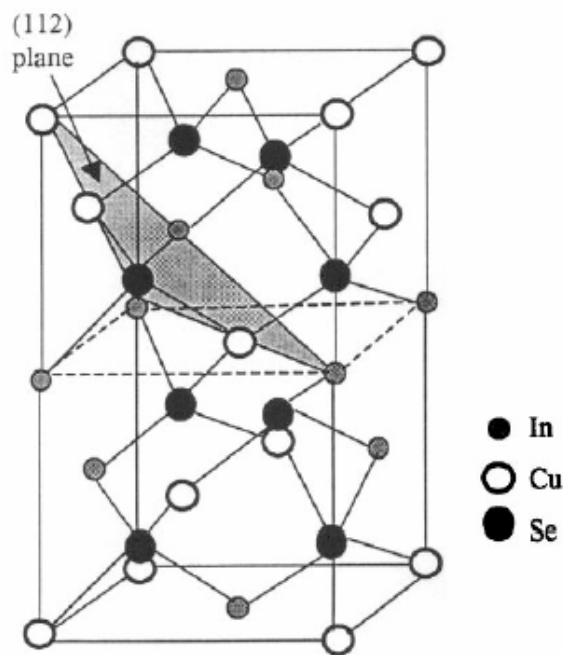
Fig. 4.1 Chalcopyrite crystal structure

The materials based on CuInSe$_2$ that are of interest for photovoltaic applications include several elements from groups I, III and VI in the periodic table. These different combinations can be generalised as I-III-VI$_2$ materials. I-III-VI$_2$ and II-IV-V$_2$ materials both exhibit the chalcopyrite structure at room temperature, but II-IV-V$_2$ materials have generally very low electron mobilities, and are thus not of interest for photovoltaic applications.

4A.3 CuInSe₂ phase diagram

The structural, optical and electrical properties of chalcopyrite thin films are critically influenced by the presence of secondary phases in the bulk of the material. In most cases, Cu and In rich secondary phases manifest themselves as electrically active defects in the compound layers and are therefore detrimental to device performance. It is believed that non-uniformities in the compound layers may either originate from micro-scale stoichiometric non-uniformities during the deposition processes.
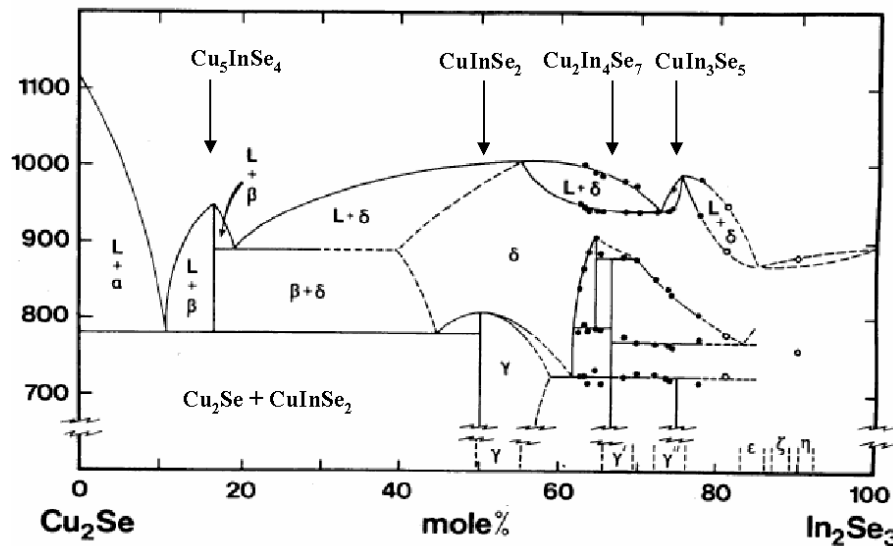
Fig.4.2 Cu_2Se-In_2Se_3 pseudobinary phase diagram

The phases for the Cu-In-Se system are represented either by ternary phase diagrams or pseudobinary phase diagrams. Pseudobinary representations were chosen to simplify presentation, since the system in question tends to exist along pseudobinary tie lines. The pseudobinary phase diagram for the Cu-In-Se system is shown in figure 4.2. According to this phase diagram various compounds (e.g. $Cu_2In_4Se_7$, $Cu_3In_5Se_9$, $CuIn_3Se_5$, Cu_5InSe_4 and $CuIn_5Se_8$) are likely to occur in this ternary system [1]. The homogeneity

113

region ranges deduced from X-ray diffraction studies at room temperature are indicated below the break in the temperature axis. The γ, γ' and γ'' regions represent distinct phases associated with the compounds $CuInSe_2$, $Cu_2In_4Se_7$ and $CuIn_3Se_5$, respectively. The chalcopyrite single phase $CuInSe_2$ extends from a stoichiometric composition of 50 mol % In_2Se_3 to In rich composition of about 55 mol % In_2Se_3. The corresponding Cu/In atomic ratios for this single phase material lie between 0.82 and 1. For the case, where the Cu/In atomic ratios are grater than 1.0, the materials are expected to contain secondary phases of Cu_2Se and for Cu/In atomic ratio less than 0.82, the materials are expected to contain secondary phases of the type $Cu_2In_4Se_7$ and $CuIn_3Se_5$. Although it is known that growth from the Cu-rich side of the In_2Se_3-Cu_2Se phase diagram leads to large grain sizes necessary for high conversion efficiencies, the growth of Cu-rich polycrystalline $CuInSe_2$ leads to a formation of the $Cu_{2-x}Se$ phase at the grain boundary surfaces. Optical and electrical analysis of this phase depicts semi-metallic behavior with bulk resistivity of 10^{-3} Ωcm [2]. The presence of these Cu-rich secondary phases affects the device operation.

4A.4 Deposition methods for $CuInSe_2$ thin films

The key component of the CIS/CdS/ZnO thin film solar cell device is the polycrystalline absorber film. The $CuInSe_2$ / $CuInS_2$ absorber formation process can proceed via a variety of chemical pathways, which are directly influenced by process parameters during deposition. The choice of the processing method is therefore important for obtaining compound films that can yield high efficiency solar cells. Regardless of the deposition technique considered, the following important criteria should be satisfied:

- An overall Cu/In stoichiometric ratio of the CIS layer should be in the 0.9–1.0 range and this should be maintained across the entire substrate. Stoichiometry controls the resistivity of the CIS layer. Films with a stoichiometric ratio above 1.0 are expected to contain secondary phases of $Cu_{2-x}Se$, which are highly conductive and lead to the formation of shunting paths. Such paths deteriorate the performance of the device.

114

- The microstructure of the film should consist of columnar grains. Grain radius must be large compared to the absorbing material thickness. This requirement influences the electrical properties of the film in terms of the lifetime of carriers diffusing through the film.
- Grain sizes should be >1μm for high performance devices.
- Films should be mechanically strong and adhere well to the Mo substrate.

A wide range of preparation methods exists for the thin film materials used in the CIS-based solar cells. The deposition method has generally a large impact on the resulting film properties as well as on the production cost. In this section, the most important deposition methods are reviewed, with the main focus on those used for the absorber deposition.

Although various techniques can be used to obtain stoichiometric CIS and CIGS films, only a few of them have resulted in high efficiency (over 15 %) solar cells so far. The absorber films for the high efficiency solar cells are usually prepared either by co-evaporation from elemental sources or by reactive annealing of precursor films (elemental or compound layers) under selenium containing atmospheres [3].

Regardless of the deposition method, the absorber films of CIS-based high-efficiency devices have smooth surface morphologies and consist of large, densely packed grains. The films are crystalline with the chalcopyrite structure [4], and their overall compositions are slightly Cu deficient, in order to favour the growth of the In-rich ordered vacancy compound (OVC) on the surface [5,6]. Also, the additional phases in the films like copper selenide and indium selenide phases affect the performance of solar cells. The presence of degenerate semiconductor like $Cu_{2-x}Se$ which is very conductive, results in high dark currents.

4A.4.1 Co-evaporation from elemental sources

The most successful absorber deposition method for high-efficiency small-area devices seems to be the three-stage co-evaporation of CIGS from

115

elemental sources in the presence of excess Se vapor [11,12]. Deposition is often performed under ultra high vacuum conditions using a molecular beam epitaxy (MBE) system. The three-stage process, developed at the US National Renewable Energy Laboratory (NREL), is based on the bilayer process of Boeing [10] that involves the co-evaporation of Cu-rich CIGS layer at a lower substrate temperature (450^0C), followed by In-rich layer at a higher temperature (550^0C). The layers intermix, forming a homogeneous film with a slightly Cu-deficient overall composition. The Ga/(Ga+In) ratio is usually varied as a function of depth. Since the band gap of CGS is higher than that of CIS, the graded Ga content results in a graded band gap of about 1.1 to 1.2 eV which in turn improves the separation of the photogenerated charge carries and reduces recombination at the back contact [11]. For example in the 18.8% efficiency cell by NREL, the Ga/(Ga+In) ratio is about 30 % near the Mo back contact and about 25 % on the top surface [13].

CIGS films prepared by the three-stage co-evaporation process have resulted in solar cell efficiencies of near 19 % by many groups. A world record efficiency of 19.2% was achieved by NREL [16], 18.5 % by Matsushita [14], 18.0 % by Aoyama Gakuin University of Tokyo [15] and the best Cd-free device with a CBD-ZnS buffer having an efficiency 18.1 % was reported by Nakada et al.[17].

A remarkable feature of the CIGS films by NREL [13] was that, they were (220/204) oriented – the typical orientation of chalcopyrite CIGS films is either random or (112). The orientations of $CuInSe_2$ and CIGS thin films were shown to depend on the orientation of the underlying $(In,Ga)_2Se_3$ precursor layer which in turn was a function of the properties of the Mo layer such as morphology, grain size and stress. The (220/204) oriented $CuInSe_2$ thin films were achieved only on dense, almost pinhole-free, large-grained Mo films with low tensile stress and a low Na content on the surface [18]. The (220/204) oriented films were found to be more resistive than the (112) oriented films, and their apparent band gaps were lower than those of the (112) oriented films.

116

In order to gain information about the material properties such as defects, high-quality CIS and CGS films have been deposited on GaAs and InGaAs [19] and on Si [20] by MBE. The use of epitaxial films in these studies eliminates the effects of grain boundaries and other non-idealities, and allows thus to get reliable and reproducible information of the intrinsic properties of the materials [19, 20].

The effect of grain boundaries on the electron transport properties of co-evaporated $CuInSe_2$ thin films has been reported by Snayal et al.[21]. It was found that grain boundaries is a predominant factor controlling the electron transport properties at lower temperatures while complex scattering mechanisms become operative at higher temperatures [21]. Cu-rich $CuInSe_2$ films have been prepared by co-evaporating the constituent elements from three independently controlled sources on to glass slides and the effects of the surface morphology and Cu_2Se sub phase with etching on the grain boundary parameters are reported by R. Pal et al.[22]. The optical properties of the co evaporated films near the fundamental absorption edge and the carried detrapping effect of these films are also reported [23].

Despite its unquestionable power in preparing high-quality material on small areas, co-evaporation exhibits some problems related to upscaling. This is due to the fact that co-evaporation requires a strict control of the evaporation fluxes to achieve the desired film properties such as composition, texture, and electrical properties. This is particularly difficult with large substrate areas. As an inevitable consequence, the conversion efficiencies of large area cells and modules are considerably lower than those of the smaller-area devices, for example the efficiency reported by Matsushita laboratories was 12.6 % for a 81.54 cm^2 submodule [24] as compared to 18 % for a small-area cell [14]. Moreover, in addition to the sophisticated and expensive equipment, the high deposition temperatures and incomplete utilization of source materials add to the complexity and cost of the co-evaporation method.

4A.4.2 Selenisation of metallic precursor layers

Although the difficulties in upscaling are somewhat similar for all the deposition methods, the alternative multistep approach where the absorber layer is prepared by a combination of simple and well established deposition techniques. This offers certain advantages such as compositional uniformity over large areas and the high throughput compared to the co-evaporation. Moreover, the processes are often very cost-effective because of the low deposition temperatures.

The most common multistep method is the selenisation of stacked metal or alloy layers. The metals or alloys can be deposited by a variety of methods, viz., sputtering [8,25–27], evaporation [7,26,28–39], and electrodeposition [27,33,38,40–47].

Selenisation is most often carried out under a selenium-containing atmosphere at high temperatures, typically above 400^0C. Selenium may be present either as H_2Se [8,26,28,33,34,39,41,44,47], most often diluted by Ar, or elemental Se [7,25,27,30–32,34,38,40,45]. Selenisation time depends on thickness, structure, and composition of the film, as well as on the reaction temperature and the source of selenium. Generally, the formation of CIS by Selenisation is faster and occurs at lower temperatures than for CGS [7,9]. CIGS films may contain CIS and CGS as separate phases if the reaction temperature is too low or the time is too short [8]. High reaction temperatures also facilitate the formation of $MoSe_2$ on the surface of Mo back contact [34]. The chalcogenisation method offers also a possibility of forming $CuIn(S,Se)_2$ thin films by introducing both Se and S precursors into an annealing atmosphere

Influence of the chalcogenide source in selenisation of evaporated Cu-In alloys at different temperatures (between 250 and 600^0C) has been studied in detail [34]. Three selenisation methods were compared: (i) H_2Se/Ar at atmospheric pressure, (ii) solid Se source under Ar flow at atmospheric pressure, (iii) elemental Se vapor in vacuum. In all cases the samples were

heated for 10 min to the reaction temperature, and the reaction time was 40 min. The H_2Se method was found to be most efficient, resulting in single-phase films at 400^0C. The use of Se vapor for selenisation was the least efficient. Selenium content of about 46–52 % was achieved by all methods. The use of H_2Se as the source for selenium, resulted in the best compositional uniformity and largest grain sizes. The formation of $MoSe_2$ was detected only when the selenisation was carried out in H_2Se at 600^0C [34]. Eventhough H_2Se is the most efficient selenisation source, its toxicity is a serious drawback. Recently, diethylselenide was introduced as selenium source, which is less toxic. Promising results were obtained from the selenisation experiments with Cu-In and Cu-In-O precursors [35].

Chalcogenisation can also be done by depositing the chalcogen film on or between the metallic layers, which was deposited by evaporation [29,30,39,42,48] or electrodeposition [36,37,43,46] and then annealing the stack under an inert atmosphere [29,37,39,42,43], thus forming the desired compound and avoiding the use of toxic vapors such as Se and especially H_2Se. Sometimes, however, a chalcogen-containing annealing atmosphere [30,39,46,48] is required in order to compensate for the chalcogen loss at high temperatures. Alberts et al. [39] observed significant Se losses upon annealing of stacked In/Se/Cu/In/Se layers above 200^0C, irrespective of whether the annealing was performed in vacuum with Se vapor or under an Ar flow without Se. No In loss was detected until above 650^0C [39].

The metal precursors are most often deposited at or near room temperature, but higher temperatures have been used as well. In order to facilitate the interdiffusion of the metal precursors and alloy formation between them, the metal precursors can be pre-annealed at a lower temperature [7,26,28,32,37,43,52] prior to Selenisation. Another approach is the deposition of Cu/In/Cu/In/Cu/In... multilayers instead of a bilayer [30,31]. The multiplayer approach has been reported to result in smoother surfaces and better crystallinity [31].

The process of Showa Shell [49,50] involves sputtering of stacked precursor layers (Cu-Ga alloy and In) followed by Selenisation with dilute H_2Se and surface sulphurization with dilute H_2S at high temperatures. The thin (about 50 nm) $Cu(In,Ga)(S,Se)_2$ surface layer is thought to improve the surface quality and thus the fill factor via the passivation of shallow defects such as selenium vacancies and Se_{Cu} antisites [50]. Module efficiency of 12.5 % was achieved for an area of 859.5 cm^2 [49]. A remarkable feature is that the device was Cd-free, with $Zn(O,S,OH)_x$ as the buffer layer [49,50].

The process of Siemens AG [51], in turn, eliminates the use of toxic H_2Se gas since the absorber is prepared by depositing the constituent elements at room temperature, followed by rapid annealing under a sulphur-containing atmosphere at 550^0C or lower temperatures to yield $Cu(In,Ga)(S,Se)_2$. Cu,Ga and In layers were sputtered, and Se was evaporated thermally. The amount of Se exceeded the stoichiometric one by about 40 % in order to compensate for the Se loss that occurs during annealing [48,51]. Moreover, the process involves a controlled Na incorporation as a Na compound deposited on Mo before the absorber deposition [48]. Module efficiency of 14.7 % (average 13.2%) for 18.9 cm^2 aperture area was achieved by this process, as compared to 11.8 % (average 11%) when the annealing was performed without sulphur [51]. This increase in efficiency was due to an increase of band gap and open circuit voltage of the absorber material [51]. The depth distributions of sulphur and gallium were nonuniform – their amounts were highest close to the Mo back contact where the absorber consisted of smaller grains than closer to the top surface. Thus, sulphur was thought to incorporate preferentially at grain boundaries [48].

The incorporation of sulphur in CIS and CIGS thin films prepared by Selenisation of evaporated metal precursors [53] or by co-evaporation [54] has been studied. The sulphur distribution in the chalcopyrite films was found to depend strongly on the composition and microstructure of the original film. The distribution was nearly uniform in copper-rich films, whereas in near stoichiometric and indium-rich films most of the sulphur was on the surface. In indium-rich films, sulphur was found also close to the

Mo/absorber interface. The sulphurization of CIS films resulted in the formation of sulpho-selenides below the $CuInS_2$ surface layer, and improved cell performance. In CIGS films, a phase separation to $Cu(In,Ga)Se_2$ and $Cu(In,Ga)S_2$ occurred, and the resulting cell performance was poor [54].

The in-line process of Lockheed Martin Astronautics involves sequential sputtering of Cu, Ga, and In from elemental targets at room temperature, followed by Selenisation in a Se vapor at higher temperatures [55,56]. Compound formation occurs via reactions of binary selenides [55,56]. Homogeneous CIS [55] and CIGS [56] films with uniform compositions are formed over 900 cm^2 substrates. Small-area efficiencies of over 10 % have been achieved on soda lime glass by using optimized post-annealing conditions [57].

4A.4.3 Evaporation from compound sources

Binary [58–60], ternary [9,32,61–65], and even quaternary [62] compounds can be used as evaporation sources for the deposition of CIS and CGS. This approach is potentially simpler and easier to control than the co-evaporation from elemental sources, provided that the compound does not decompose during heating, thus resulting in a film composition that differs from the source material. Very often Se is lost during deposition, in that case a Se atmosphere is required during deposition and/or post deposition annealing. Decomposition may be avoided by a very fast heating to sufficiently high temperatures so that the material evaporates before it decomposes [65]. This approach is utilized for example in flash evaporation [61–65] and related methods [60] as well as in pulsed laser deposition [66,67].

Park et al. [58] evaporated In_2Se_3 / Cu_2Se bilayers at room temperature and annealed them in a Se atmosphere at 550^0C to yield crystalline single phase Cu and Se rich $CuInSe_2$ films. After annealing, small amounts of In_2Se_3 and Se were deposited on the film surface at the same temperature in order to form a thin $CuIn_3Se_5$ layer. A solar cell efficiency of 5.4 % was achieved with the Ag/n-ZnO/i-ZnO/CdS/$CuIn_3Se_5$/$CuInSe_2$/Mo structure [58]. The

efficiency increased to 9.6 % when the process was slightly modified: Se was co-evaporated with In_2Se_3 during the initial stage at substrate temperature of 150^0C, and in the Cu_2Se evaporation stage, the substrate temperature was increased to 440^0C followed by the subsequent Se annealing (10 min) at that temperature. The Cu-poor surface layer was formed again by evaporating small amounts of In_2Se_3 and Se. An efficiency of 9.3 % was achieved with no OVC layer but a slightly Cu-poor surface [59].

The sequential "quasi-flash evaporation" of In_2Se_3 and Cu_2Se onto unheated substrates and a subsequent anneal at 500^0C under Ar for 1 h resulted in single-phase chalcopyrite CIS films with random orientation and p-type conductivity. The evaporation of In_2Se_3-Cu_2Se mixtures by the same method led to the formation of (112) oriented single-phase CIS after annealing at 400^0C. The control of the film composition in the latter method was difficult, however, because In_2Se_3 melted earlier than Cu_2Se, and the evaporating In_2Se_3 vapor caused some loss of the unmelted Cu_2Se powder. That is why the films evaporated from mixture of In_2Se_3 and Cu_2Se were very Cu-deficient and thus n-type [60].

Thermal evaporation of p-type $CuInSe_2$ thin films from a single CIS source at substrate temperatures ranging from 200 to 600^0C was reported by Sadigov et al. [32]. Because of difficulties in achieving stoichiometric, crystalline and binary phase free films with good surface morphology, additional Cu and In were evaporated on the films at room temperature, and the films were subsequently selenized in a Se containing atmosphere [32].

Klenk et al. prepared CIS, CGS and CIGS films from CIS and CGS powders and their mixtures at substrate temperatures between room temperature and 350^0C both by thermal [9] and flash [61] evaporation. In both cases, the resulting films were Se-deficient unless the evaporation was done in the presence of additional Se vapor. The films were annealed in the presence of Se vapor at high temperatures of up to 550^0C. Thermal evaporation resulted in uniform and dense films when the substrate temperature was between 200

and 300^{0}C; film thickness (1.5 μm) and composition were nearly constant over an area of 10 cm x 10 cm. Film formation was found to proceed via the formation of binary selenides – probably because the relatively slow heating rate of the precursor powders caused their decomposition. A significant difference between the formation kinetics of CIS and CGS was observed: the formation of single-phase CuGaSe$_2$ required reaction temperatures above 500^{0}C, whereas single-phase chalcopyrite CuInSe$_2$ was obtained already at temperatures as low as 350^{0}C, with no significant improvement of crystallinity at higher temperatures. Moreover, single-phase CIGS was obtained only when the Ga content of the film was below 6 at.% [9]. Substrate temperature did not affect the composition of flash evaporated films significantly [61].

Often, the compositions of flash evaporated films have been found to depend on substrate temperature. Merino et al. [62] studied the flash evaporation of CIS and CIGS from two types of crucibles and at different substrate temperatures. About 10 wt.% of Se powder was added to the crucible along with the compound source, in order to prevent the formation of Se-poor films. The deviations of the film stoichiometry from the source material were minimized by, carefully choosing the temperatures of crucible and substrate and keeping the deposition rate low enough. Solar cells with CdS and ZnO buffer layers were made, by co-evaporating a thin CuIn$_2$Se$_{3.5}$ layer on the absorber. The best efficiencies were 5.1 % for CIS and 6 % for CIGS [62].

Amorphous CIS films have been deposited by flash evaporation onto unheated substrates [63,64]. XRD peaks of CIS and Cu$_7$In$_4$ together with some unidentified peaks appeared when the substrate temperature was 200^{0}C or above. Also post-annealing at 350^{0}C resulted in the formation of CIS, Cu$_7$In$_4$ and In$_2$Se$_3$. The optimum conditions for the formation of CIS were determined to be the substrate temperature of 250^{0}C and post-annealing at 350^{0}C for 3–4 h. [64]. On the other hand, Joseph and Menon [65] prepared crystalline p-type CIS films by flash evaporation from a single CIS source

onto unheated substrates. Single-phase chalcopyrite films were obtained after annealing in vacuum at 50^0C for 1 h [65].

Victor et al. [66] prepared (112) oriented CIS thin films by pulsed laser deposition at a substrate temperature of 150^0C. The chalcopyrite phase was present already in the as-deposited films, and the crystallinity was further increased by annealing in Ar at 500^0C for 10 or 20 s. Kuranouchi et al. [67] deposited CIS films on unheated substrates and at a substrate temperature of 500^0C. The films were post-annealed at 500^0C in vacuum. The films deposited at room temperature exhibited (112) orientation after annealing [67].

4A.4.4 Other deposition techniques

Chemical gas phase deposition techniques such as metal organic chemical vapor deposition (MOCVD) [68–71] and close-spaced vapor transport [72,73] have also been used for the preparation of CIS and CIGS thin films. A possible advantage is lower deposition temperatures than in evaporation processes. A plasma-enhanced CVD process was also reported [69] where hexafluoro-acetylacetonate complexes $Cu(hfac)_2$ and $In(hfac)_3$ were used as the metal precursors and 4-methyl-1,2,3-selenadiazole as the Se source. H_2 was used as the carrier gas for the metal precursors. Deposition temperatures ranged from 150 to 400^0C. The resulting films were Se deficient probably due to a Se loss during post-deposition cool-down in vacuum [69]. Solar cells fabricated from the CVD grown films were not very efficient; the maximum open circuit voltage was 0.26 V [71]. For comparison, the open circuit voltages of high-efficiency devices are generally above 0.6 V [13,16, 14–17].

CIS, CGS, and CIGS thin films have been deposited by close-spaced vapor transport using iodine as a transport agent [72,73]. $CuIn_{1-x}Ga_xSe_2$ films with compositions identical to those of the source materials were obtained within the whole composition range (x from 0 to 1). Moreover, the films exhibited

chalcopyrite structure, good surface morphology and p-type conductivity [73].

CIS and CIGS thin films have been prepared by chemical bath deposition using sodium selenosulphate (Na$_2$SeSO$_3$) as the selenium precursor [74-76]. Garg et al. [76] have deposited CIS films at 40^{0}C using Cu(NH3)$_4^{2+}$, and In^{3+} complexed by citrate as the metal precursors. After post annealing at 520^{0}C in air, V$_{OC}$ about 0.3 V was measured for a n-Si/p-CIS heterojunction.

Single-phase chalcopyrite CIS and CIGS thin films with strong (112) orientation and p-type conductivity have been prepared by spray pyrolysis from acidic aqueous [77] and aqueous ethanolic [78] solutions of CuCl$_2$, InCl$_3$, GaCl$_3$ and N,N-dimethyl selenourea. Films deposited from aqueous solutions at 400^{0}C [77] were reported to be uniform and adherent to the substrate, with compositions close to those of the deposition solutions, whereas films deposited from aqueous ethanolic solutions [78] at the same temperature were slightly (In+Ga) rich, with a higher Ga/(In+Ga) ratio than in the deposition solution. Solar cell efficiencies of spray pyrolysed absorbers were low.

One-step electrodeposition of CIS is usually carried out from an aqueous acidic solution containing simple compounds of Cu^{2+} or Cu$^+$ and In^{3+}, most often sulphates [29, 79–82] or chlorides [83–91]. Generally, the CIS-based absorbers prepared by one-step electrodeposition have not resulted in high-efficiency devices. Electrodeposited CIGS films can anyhow be used as precursors for the preparation of high-efficiency devices (15.4 %) [83,84], if the film composition is adjusted by evaporation of In, Ga and Se afterwards. The highest conversion efficiencies achieved by one-step electrodeposited CuInSe$_2$ absorber films without subsequent annealing under Se-containing atmospheres are those of Qiu and Shih [92,93]. Their CIS films were deposited from a single solution that contained ions and complexes of Cu, In, and Se [94]. The films were post-deposition annealed at temperatures between 300 and 420^{0}C for 20 min under Ar or in vacuum, and resulted in

conversion efficiencies of 7 % [92] with a Mo/CIS/CdS structure and 6.3 % with a Mo/CIS/CdS/ZnO structure [93].

4A.5 Experimental details

In this section the preparation of $CuInSe_2$ thin films by the flash evaporation is discussed. The potential advantages of flash evaporation are its speed, ready application to large areas and low cost. The flash evaporation involves the preparation of the basic material and then the deposition of this material to the substrates. Bulk copper indium selenides with Cu/In ratios 0.861 to 1.1 were prepared from 99.99% pure Cu, In and Se by the solid state fusion technique. The elements were taken in the desired composition in an evacuated quartz ampoule. The solid-state reaction was carried out at a temperature 700^0C for one hour. The bulk compound thus obtained was powdered to fine grains, mixed thoroughly and again subjected to solid-state reaction as described earlier. The chalcopyrite structure of the compound was confirmed by the X-ray diffraction studies (Fig.4.3).
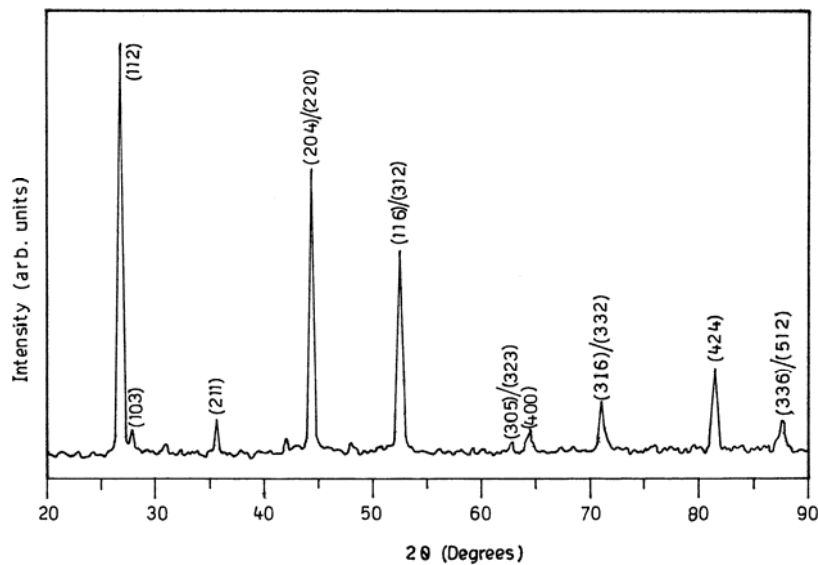

Fig.4.3 Typical XRD pattern of the bulk $CuInSe_2$ powder (Cu/In = 0.974)

The fine CuInSe$_2$ chalcopyrite powder samples thus synthesized were used for the flash evaporation. The flash evaporation was carried out in a vacuum chamber at a base pressure of $2x10^{-5}$ mbar. The powder was taken in a specially designed stainless steel crucible, which was connected to a vibrator. The frequency of the vibrator was controlled externally. The CuInSe$_2$ powder coming out of the groove of the crucible was channelled to fall on to the hot molybdenum boat using a glass chute. The outgassing occurred during the flash evaporation resulted in the variation of vacuum in the range $2x10^{-5}$ – $5x10^{-5}$ mbar. The films were deposited on cleaned glass substrates, which were kept at 10cm above the evaporation source. The deposition was carried out without any intentional heating of the substrate. The evaporation itself has raised the temperature of the substrate to around 100^0C. The thickness of the films during deposition was monitored using a digital thickness monitor. The as deposited films showed thickness the range 0.2 to 3 μm.

The as deposited CuInSe$_2$ thin films were found to be selenium deficient and hence they were subjected to different annealing processes. The samples were selenised at 350^0C for 2 hours under N$_2$ gas flow with selenium vapour source kept close to the samples. The set up used for selenisation is given in section 2.2.7. The selenised samples were again subjected to annealing in Argon atmosphere at 400^0C for 2 hours.

The structural studies of the bulk, as deposited and annealed thin films were performed using the X-ray diffractometer and the optical transmission was recorded using the UV-VIS-NIR spectrophotometer (Hitachi-Model U3410). The electrical resistivity of the films was measured using a Keithley source measure unit (Model SMU 236) by two-probe method in planar configuration with highly conducting silver paint as the electrodes.
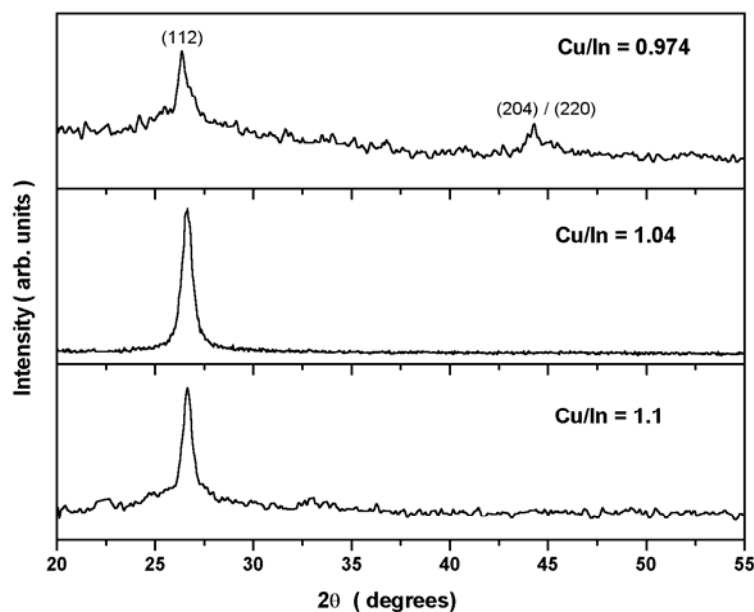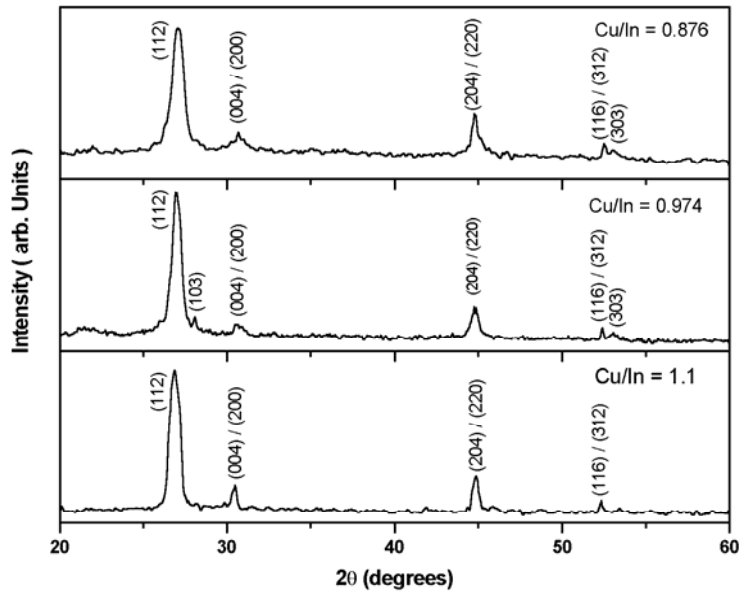
Fig. 4.4 XRD pattern of the as deposited $CuInSe_2$ thin films prepared by flash evaporation of $CuInSe_2$ powder with various Cu/In ratios

4A.6 Results and Discussion

4A.6.1   X-ray analysis

The XRD spectra of the as deposited $CuInSe_2$ (CIS) films exhibit only a major single diffraction peak indicating a strong preferred orientation along the (112) plane. Some groups have reported the formation of amorphous $CuInSe_2$ thin films by flash evaporation [63,65] when the deposition was carried out at room temperature. This apparent contradiction can be understood by considering the effect of radiant heat during evaporation, which increased the substrate temperature up to 100^0C. This rise in substrate temperature might be the cause for the strongly observed (112) orientation. The substrate temperature has a significant effect on the crystallinity and the preferred orientation of the film. Some of the samples showed an additional peak (220) as shown in figure 4.4. The secondary phases that might be present in the films were not able to detect by the XRD spectra.

Fig. 4.5 XRD pattern of the flash evaporated CuInSe₂ thin films annealed in selenium vapour

To compensate the loss of selenium during the flash evaporation of CIS, the as deposited samples were annealed in selenium atmosphere followed by the annealing in inert gas. Figure 4.5 shows the XRD spectra of the CuInSe₂ films with different Cu/In ratios of the starting precursor after the post deposition annealing in selenium. It shows reflections from other planes in addition to the strong (112) peak indicating the formation of chalcopyrite structure. These peaks confirm the relaxation in the preferred orientation of the film structure and changes in the film composition shifting to the initial chalcopyrite bulk material. In these CIS films the relative intensities of the peaks did not match with the corresponding JCPDS values. Similar observation has been made for the CIS films prepared by the selenisation of Cu-In alloys [95]. The intensity of the reflections from the (112) plane was very high in all cases showing high degree of preferred orientation along this plane. The orientation of CIS film in the (112) plane is highly preferred for good lattice matching with CdS buffer layer [95]. The lattice constant values

of the as deposited and the annealed samples are given in Table 4.1. The tetragonal distortion values ($\nabla=2$-c/a) of all the annealed films were found to be +ve indicating the built in dilation.

Table 4.1 The lattice constants of the flash evaporated CuInSe$_2$ thinfilms after annealing in selenium vapour

| Cu/In Ratio	a (A^0)	c (A^0)	c/a
1.1	5.69	11.76	2.0671
1.09	5.68	11.88	2.0910
0.974	5.69	11.69	2.0533
0.861	5.64	11.72	2.0795

4A.6.2   Electrical Properties

The electrical resistivity of the as deposited and the annealed films were found to vary with the Cu/In ratio of the starting precursor. The copper rich CIS films showed low conductivity compared to the indium rich films. The resistivity was found to be ~10^4 Ωcm for the as deposited films with Cu/In ratio greater than 1. The resistivity varied from 2.6×10^4 to 1.24 Ωcm for the as deposited films and 7 to 0.2 Ωcm for the annealed films, when the Cu/In ratio of the starting precursor varied from 1.1 to 0.86. This is consistent with the reported resistivity values of CuInSe$_2$ films [65,97]. There was a considerable decrease in the resistivity of the films after the post deposition heat treatments (Fig.4.6). The nature of the conductivity can be explained on the basis of the valence stoichiometry relation,

$$\Delta z = \frac{2[Se]}{[Cu]+3[In]} - 1 \tag{4.1}$$

The positive value of the ideal valence stoichiometry Δz results in p-type films, via. the presence of metal vacancies (acceptors), and the negative values imply Se vacancies resulting in intrinsic, or slightly n-type films [102]. The type of conductivity of the films was determined by the thermal probe technique. All the as deposited CuInSe$_2$ samples were found to be p-type. It has been reported that flash evaporated CIS films showed n-type

conductivity only when an elevated substrate temperature was used [97]. The n-type film formation was interpreted by the re-evaporation of selenides from the films deposited on hot substrates.
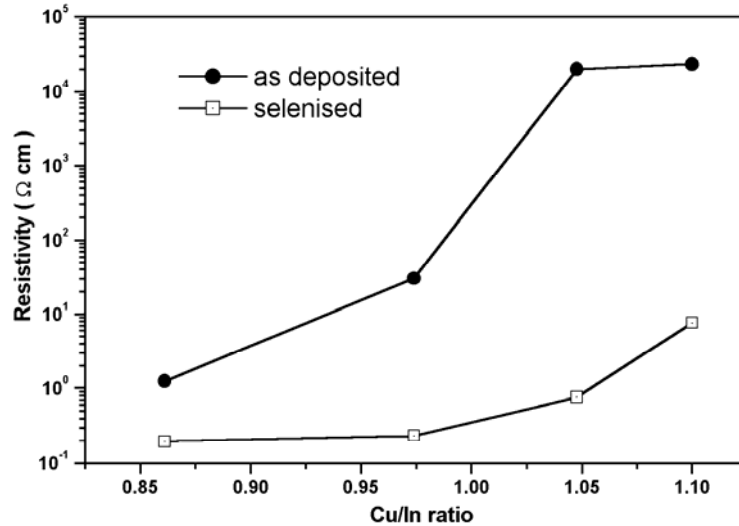

Fig 4.6 The variation of resistivity of the flash evaporated CuInSe₂ thin films with the Cu/In ratio in the precursor

4A.6.3   Optical analysis

The transmission spectra of the films were recorded using UV-Vis-NIR spectrophotometer. The intrinsic absorption edge of CIS was examined using the relation given by Bardeen et al [98]. Since CuInSe₂ is a direct band gap material, the absorption coefficient α is related to the incident photon energy $h\nu$ as, $\alpha h\nu = \beta\, (h\nu – E_g)^{1/2}$ where E_g is the energy gap. The band gap of the films was determined as described in section 2.3.5.

Typical transmission spectra of the as deposited and the annealed CIS films are given in figure 4.7. The inset of the figure shows the $(\alpha h\nu)^2$ against $h\nu$ curves of the as deposited and the annealed CIS films. The variation of the band gap of CIS films with the Cu/In ratios in the starting precursor is shown in figure 4.8.
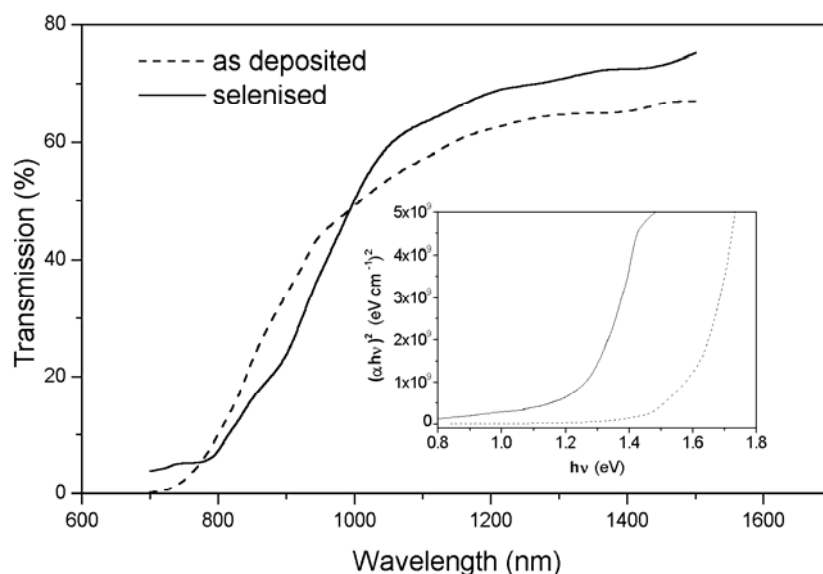
Fig. 4.7 The transmission spectra of the flash evaporated CuInSe$_2$ thin films. Inset shows the $(\alpha h\nu)^2$ against $h\nu$ curves of the as deposited and the annealed CIS films (Cu/In = 0.974)

The variation of the band gap with Cu/In ratio shows a similar behaviour in the case of as deposited and the samples annealed in selenium vapour. The band gap of the as deposited CIS films varied from 1.35 to 1.58 eV as Cu/In ratio was varied from 0.86 to 1.1. The higher value of the band gap of the as deposited films compared to that for single crystal (1.04 eV) [99] might be due to the presence of the binary phases existing in the film, though no such secondary phases were detected by XRD. The selenisation of the samples resulted in the reduction of band gap. The annealed samples have a band gap in the range 1.18 to 1.28 eV. The band gap of 1.2eV has been reported earlier for the flash evaporated CuInSe$_2$ films [62,100]. It can be concluded that the selenisation has resulted in the incorporation of more selenium into the films there by modifying the electrical and optical properties of the films. The reduction in the band gap of the as deposited films on annealing can be attributed to the following factor. It has been reported that the surface of slightly In rich CuInSe$_2$ films corresponds to an ordered vacancy compound

(OVC). This OVC has been identified with a dominant $CuInSe_2$ phase with a band gap of 1.3 eV, higher that the $CuInSe_2$ [5,101]. The presence of other phases in the as deposited CIS result in higher band gap. The as deposited films which may have binary phases and amorphous phases, on annealing in selenium atmosphere crystallize into CIS phase and the binary phases are also converted into CIS and the resulting band gap in match with the band gap values reported for flash evaporated CIS [62,100].
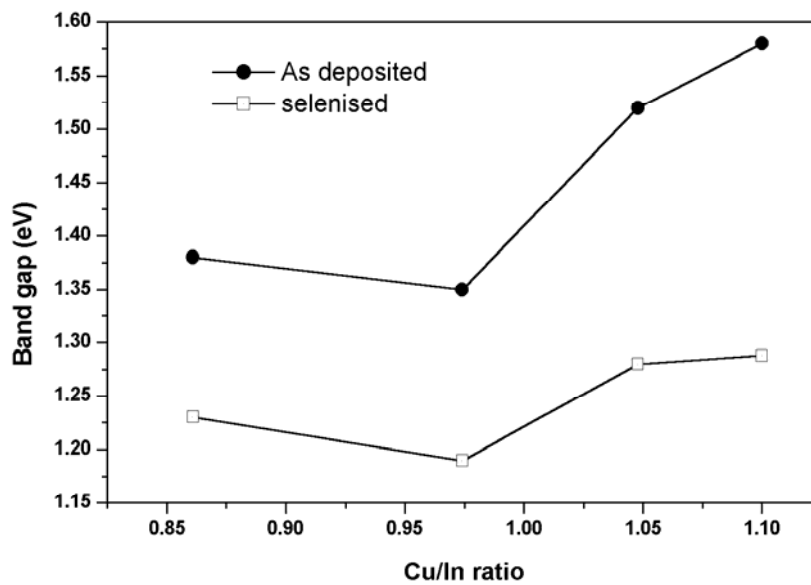
Fig. 4.8 The variation of band gap of the flash evaporated $CuInSe_2$ thin films with the Cu/In ratio in the precursor

4A.7 Conclusion

Chalcopyrite, polycrystalline $CuInSe_2$ thin films were successfully prepared by the flash evaporation of the bulk material with different Cu/In ratios. The as-deposited films showed higher band gap energies due to the presence of the binary phases, which might have formed due to the selenium deficiency in the films during flash evaporation. The as deposited films were found to be p-type. The selenisation of the as deposited films resulted in

stoichiometric films with a chalcopyrite structure showing a strong preferred orientation along the (112) plane. The films showed electrical resistivity in the range 7 to 0.2 Ωcm and an optical band gap energy of 1.18eV.

Part B

Preparation and characterisation of CuInS$_2$ thin films by two-stage processes

The structural, electrical and optical properties of copper-indium alloys sulphurised in H$_2$S atmosphere have been studied by varying the thermal cycle of the sulphurisation process. Cu-In alloy prepared by elemental evaporation of copper and indium was used as the precursor for sulphurisation. The chalcopyrite CuInS$_2$ phase was found at sulphurisation temperature as low as 250^{0}C and single phase at sulphurisation temperature 350^{0}C. At low sulphurisation temperature, different binary phases like CuS Cu$_2$S, InS and In$_6$S$_7$ were found. Short sulphurisation time also results in secondary binary phases. The optimum sulphurisation temperature was 350^{0}C for three hours which resulted in single phase p-type chalcopyrite CuInS$_2$ films with a band gap of 1.45eV. The dependence of processing parameters and the Cu/In ratio of the starting precursors on the electrical, optical and structural properties of the films are studied.

4B.1 Introduction

CuInS$_2$ is an important compound from the chalcopyrite family suitable for solar cells due to its high optical absorption and the direct band gap at 1.5 eV. In principle, solar cells based on sulphur chalcopyrites like CuInS$_2$ have the same potential for high efficiencies as those based on selenium chalcopyrites. The development of CuInS$_2$ is attractive, because the non-toxic sulphur substitutes the toxic selenium. Moreover, this material can be made both n and p-type, enabling the fabrication of homojunction and heterojunction solar cells. The open circuit voltage of CuInS$_2$ solar cells can theoretically be higher (1.2 V) than the voltage of Cu(In,Ga)Se$_2$ cells. At the same time photo current is lower. This is advantageous for the serial connection of multiple cells in a module. CuInS$_2$ films can be fabricated in a fast and robust process granting high throughput in an industrial process. However, the open circuit voltage up to now limits the efficiency of CuInS$_2$ solar cells, which is far below the theoretical value. Efficiencies more than 12% have been reached with Mo/CuInS$_2$/CdS/ZnO cell structure [103–105]. Based on the fundamental considerations CuInS$_2$ solar cells are expected to show efficiencies superior to those of Cu(In,Ga)Se$_2$ solar cells (Table 4.2) , sulphide has reached only approximately 60% of the efficiency of the selenides so far.

Table 4.2 Theoretical efficiencies for the common Cu chalcopyrite solar cells [106].

| Material	Band gap	Theoretical efficiency
CuInSe$_2$	1.04	25%
Cu(In,Ga)Se$_2$	1.21	27.5%
CuInS$_2$	1.53	28.5%
CuGaSe$_2$	1.68	26%

4B.2 Crystallography of CuInS$_2$

CuInS$_2$ belongs to the family of I-III-VI$_2$ chalcopyrite compounds. The members of this family are related to each other by their chalcopyrite crystal

structure. The tetragonal chalcopyrite crystal structure of $CuInS_2$ is the same as that of $CuInSe_2$ shown in Fig 4.1. The conductivity type of the chalcopyrite Cu-ternaries are usually determined by the composition of the crystal rather than doping by shallow level impurities.

4B.3 CuInS₂ phase diagram

The knowledge of the phase formations is essential in the preparation of the ternary compounds. The presence of secondary phases will affect the microstructure and the properties of the film and hence is to be avoided in the solar cell devices for achieving better efficiency. A schematic ternary (Cu-In-S)-phase diagram is given in figure 4.9. For the sake of clarity only binary phases on the Cu_2S-In_2S_3 and CuS-InS intersections are marked. Besides $CuInS_2$ only one more ternary phase $CuIn_5S_8$ in spinel structure was observed in the (Cu-In-S)-system [107].
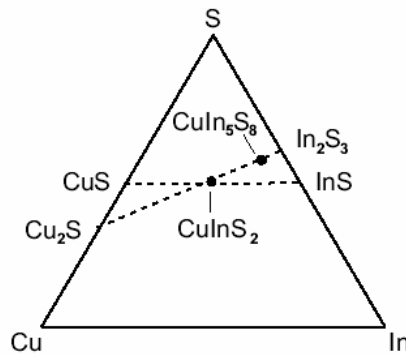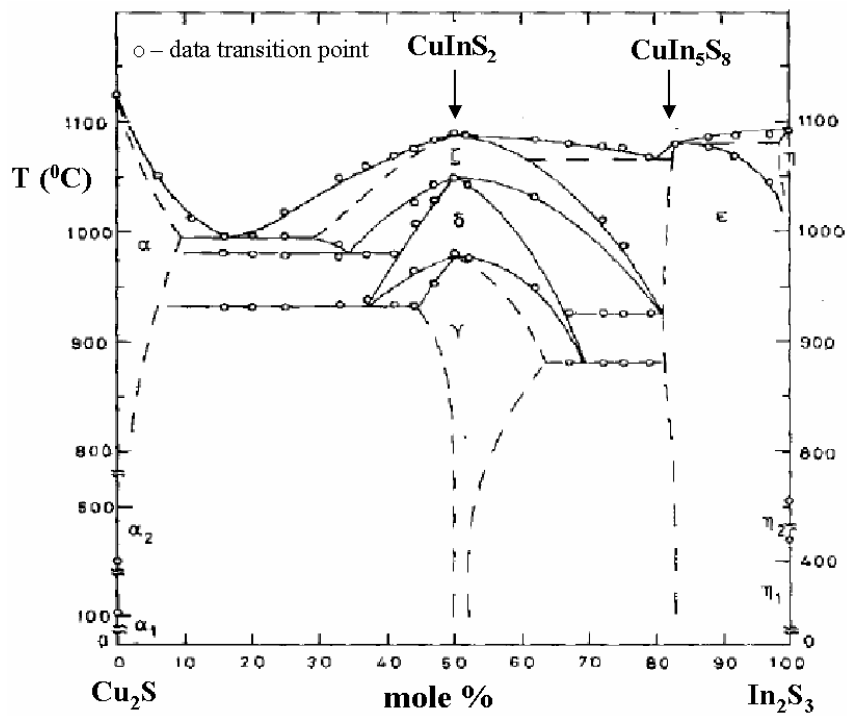

Fig 4.9 Ternary phase diagram of Cu–In–S system

The phase diagram of the binary system Cu_2S-In_2S_3 is given in figure 4.10. All compounds occurring in this system are summarized in table 4.3. Two semiconducting phases $CuInS_2$ and $CuIn_5S_8$ appear in the diagram. $CuInS_2$ exists in three modifications, up to 980^0C in the chalcopyrite structure, between 980^0C and 1045^0C in the zinc blende structure and above 1045^0C up to the melting point at 1090^0C in a still unknown structure, possibly wurtzite [107]. The second semiconductor, $CuIn_5S_8$ has the spinel structure over the whole temperature range of 20^0C to the melting point at 1085^0C.

137

Table 4.3 Compounds occurring in the system Cu_2S–In_2S_3 with their different modifications and transition temperatures

Compound		Modification	Transition temperature (^0C)
Cu_2S	α_1	tetragonal	104
	α_2	hexagonal	450
	α	cubic	1125 (mp)
$CuInS_2$	γ	chalcopyrite	980
	δ	zincblende	1045
	ζ	wurtzite	1090 (mp)
$CuIn_5S_8$	ε	spinel	1085 (mp)
In_2S_3	η_1	defect-spinel-superstructure	420
	η_2	defect-spinel-structure	755
	η	layered structure	1090 (mp)

Fig 4.10 Pseudobinary phase diagram of Cu_2S–In_2S_3

138

4B.4 Deposition methods for CuInS$_2$ thin films

Several preparation methods, in different states of development, are used for a systematic investigation of the material properties relevant for photovoltaic applications. The suitable preparation methods for the stable CuInS$_2$ films are the following:

1. Co-evaporation of the elements.
2. Sequential sputtering/evaporation of metal films/binary components followed by the annealing in sulphur vapour/H$_2$S (two stage process).
3. Sequential sputtering/evaporation of metal layers followed by the preparation of metal alloy precursor and the subsequent sulphurisation of the precursor.
4. Sequential deposition of oxide precursors by PLD/ sputtering followed by sulphurisation.
5. Chemical methods such as spray pyrolysis, chemical vapour deposition etc.

At the present stage, CuInS$_2$ films prepared by co-evaporation or sequential processes exhibit comparable opto-electronic properties. In co-evaporation the exact control of stoichiometry is difficult and homogeneity on large area require complicated system layout. Sequential processes are well scalable and can be applied to large areas. Stoichiometry and homogeneity can be easily controlled. But this method has a limited influence on the growth and multinary alloys are not always possible. Different deposition methods used for the preparation of CuInS$_2$ thin films are briefly reviewed in the next sections.

4B.4.1 Thermal evaporation

A variety of vacuum evaporation techniques have been used to deposit chalcopyrite CuInS$_2$ thin films such as; single [108,109], dual [109–111] and three-source co-evaporation [112–116]. Kanzari et al. [108] have deposited CuInS$_2$ thin films on Mo coated glass substrates by vacuum evaporation of CuInS$_2$ powder from the resistively heated tungsten boats. Depositions were

carried out at substrate temperature in the range 65–295^{0}C. The films grown at temperatures below 200^{0}C were practically stoichiometric and had a high amorphous content. For temperature above 200^{0}C minor phases of the binary compounds In, Cu_7In_4 were formed. The optimal substrate temperatures for good quality films were 140^{0}C and 240^{0}C, which correspond to low roughness and high grain size [108]. Kazmerski et al. [109] have reported that the single source method is not the best deposition technique for the single phase $CuInS_2$ thin films. The films deposited by the single source evaporation were found to be n-type and multi phased. Elemental In and Cu were also detected in these films. The amount of single phase $CuInS_2$ was increased for substrate temperatures above 250^{0}C and for higher deposition rates [109]. In order to overcome the disadvantages during the single source evaporation dual source evaporation was employed [109,110]. In this method one resistively heated alumina crucible was used to evaporate $CuInS_2$ powder and a second sulphur source (Ta crucible) was utilised to vary the amount of sulphur in the chamber. Both n-type and p-type films have been deposited varying the sulphur concentration. For higher sulphur concentrations, the films showed p-type nature due to the decrease in the sulphur vacancies. Efficiency below 4% was achieved using this dual source evaporated $CuInS_2$/CdS solar cell [110,111].

The solar cells with Mo/$CuInS_2$/CdS/ZnO structure using co-evaporated $CuInS_2$ have shown 10.2% efficiency [112]. Here tenfold excess of sulphur vapour and a substrate temperature of 550^{0}C was used during the evaporation. Both Cu-rich and In-rich $CuInS_2$ films were used as absorber layers. The binary phases in the Cu-rich films were removed by the KCN treatment. The cell efficiencies were limited to 1.5% when In-rich absorber layers are used. This may be due to the insufficient p-type doping in the In-rich layers. Cells prepared from Cu-rich compositions showed improved performances [112]. Scheer et al. [113] have studied the effect of cooling rate during the co-evaporation of $CuInS_2$ films. The room temperature conductivity is strongly affected by the cooling rate. A maximum conductivity of 10^{-3}Scm^{-1} was obtained for a cooling rate 2 K/min. The effect of slow cooling rate on the conductivity might be due to the saturation of S

vacancies during the cool-down period. Conductivity enhancement was also observed for films annealed in an oxidizing environment [113]. Co-evaporated CuInS$_2$ solar cells with a Cd free buffer layer have been reported by Braunger et al.[115]. The device with CBD grown In$_x$(OH,S)$_y$ buffer layer showed an efficiency of 11.4%. This is the highest efficiency reported for a Cd free and Se free chalcopyrite based thin film solar cell. Epitaxial growth of Cu(In,Ga)S$_2$ on Si (111) substrates by co-evaporation using MBE system has been reported by Metzner et al.[114].

Flash evaporation has been effectively used for depositing CuInS$_2$ thin films [117,118]. Since CuInS$_2$ dissociates incongruently, it is very difficult to deposit single-phase thin films by flash evaporation. Agarwal et al. [118] investigated the flash evaporation technique for growing CuInS$_2$ thin films and amorphous films were obtained at room temperature. The films deposited at room temperature exhibited a high dc electrical resistivity. The resistivity decreased with an increase in substrate temperature owing to the improvement in grain size and crystallinity of the films. The optical band gap of the material was found to be less than the reported value for CuInS$_2$ single crystals. The band gap of the films increased from 1.16 to 1.31eV when the substrate temperature was varied from 303 to 523K. The presence of localized states leads to lower band gap values at lower substrate temperatures. The as deposited film showed n-type conductivity. A Molybdenum source temperature of 1873 K and a substrate temperature of 523K were found to be the upper limits for obtaining reproducible results and single phase n-type CuInS$_2$ films in flash evaporation [118].

4B.4.2 Two stage process

A promising approach for the preparation of CuInS$_2$ films is the so-called two-stage or reactive sulphurisation process, which involves the preparation of Cu-In precursor film and subsequent annealing in hydrogen sulphide or sulphur atmosphere. The precursors for the sulphurisation are usually stacked elemental layers of In and Cu or Cu-In alloys. The precursor layers can be deposited by a variety of methods, the most common of which are co-

evaporation of the Cu-In layers [119,120], bi-layer (In/Cu) or multi layer deposition by thermal evaporation [121–126], electron beam evaporation [129], sputtering [128] and electrodeposition [129]. The deposition of the Cu-In layers by vacuum evaporation followed by the annealing to form Cu-In alloy has been reported by Dzionk et al. [130]. A minimum temperature of 375^0C was required for the complete conversion of Cu-In precursor to $CuInS_2$ when sulphur vapour was used, but for H_2S flux a temperature of 250^0C was reported to be sufficient due to high reactivity of H_2S.

Sulphurisation is most often carried out at temperatures above 200^0C using H_2S [119,123,124,129], diluted H_2S gas with Ar [120–122, 127,126,130], or in the presence of sulphur [125,126]. The process of Bandyopadhya et al.[125] involves the deposition of stacked elemental layers (SEL) of In/Cu over Mo coated glass substrates followed by the annealing at temperatures 620–880K in a graphite box. The graphite box is placed inside a quartz chamber in partial argon atmosphere and required amount of sulphur was also placed inside the chamber as sulphurisation agent. The quartz chamber was heated in an electronically controlled furnace. Both p-type and n-type films were prepared and the films showed a preferred orientation along the (112) orientation with c/a values varied between 2.03 and 2.08. Best films were obtained by annealing the SEL at 820K for 45 min.

Some groups have reported the preparation of $CuInS_2$ thin films by the sulphurisation of oxide precursors [131,132]. Cu-In-O thin films were prepared by the sputtering of $Cu_2In_2O_5$ powder target in Ar atmosphere containing 5% O_2. $CuInS_2$ films were prepared by the sulphurisation of the Cu-In-O films at 550^0C for 1 hr in $H_2S + H_2$ atmosphere [131]. Wada et al. [132] prepared the Cu-In-O film by the pulsed laser ablation of $Cu_2In_2O_5$ target. These Cu-In-O films were converted into single phase $CuInS_2$ film by annealing above 400^0C in H_2S diluted with N_2 for 4hrs. Cu-In-O film deposited at room temperature was found to be the best precursor for preparing $CuInS_2$ films. Films sulphurised at about 500^0C show well-developed large grains at the vicinity of the substrate, while the films

sulphurised at a higher temperatures show homogeneously distributed large grains.

4B.4.3 Other deposition techniques

Reactive sputtering of $CuInS_2$ thin films has been reported by He et al. [133], which involves the reactive rf sputtering of Cu-In alloy target in H_2S. $Cu_{11}In_9$ secondary phase was observed in the sputtered films, indicating that H_2S flow during the sputtering is insufficient. Spray pyrolysis is a simple, inexpensive and low energy technique to produce low cost films of ternary compounds. The ratio of the constituents can be determined by controlling their concentration in the spray solution. Spray pyrolysis has been used to deposit $CuInS_2$ thin films [134–137]. The films deposited by spray pyrolysis in [134] showed a sphalerite structure, which transformed to the chalcopyrite structure on annealing at 670K. Spray pyrolysis produced multiphase films with poor crystallinity when In-rich and Cu-rich solutions were used [136]. Gonzalez et al. [137] have reported that the conductivity type and the specific resistivity of the $CuInS_2$ thin films can be controlled by changing the molar ratio of [Cu]/[In] and [S]/[Cu] during spray pyrolysis. Bini et al.[138] has reported the preparation of $CuInS_2$ thin films from the chemical bath deposited Cu_xS films by the vacuum annealing of the evaporated indium layer over the CBD grown Cu_xS thin films.

4B.5 Experimental Details

4B.5.1 Precursor preparation

Metallic precursors with In-Cu bilayer structure were prepared on glass substrates by vacuum thermal evaporation of Indium (99.999%) and Copper (99.99%) in a sequential mode. The base pressure of the vacuum system was $2x10^{-5}$ mbar. To achieve various Cu/In ratio in the precursors and consequently in the sulphurised films, the thickness of the Indium layer was kept at $4000A^0$ and the thickness of the copper layer was varied from sample to sample. All the results (except for figure 4.21) presented in this part of the

thesis, the Cu/In ratio is specified for the starting precursor estimated from the thickness of individual copper and indium layers. The thickness of the films during the deposition was monitored using a digital quartz thickness controller. The average thickness of the final copper indium sulphide films was about 2 Ωm. The precursors with copper layer followed by Indium (glass/Cu/In) structure were found to be less adhesive to the substrates. Hence all the studies reported here are on the precursors with glass/In/Cu bilayer films. The deposition of Indium was carried out at a substrate temperature 75^0C, while copper layer was deposited without any intentional heating of the substrates (30^0C). After the deposition of the metal layers, the samples were annealed at 153^0C for two hours in order to stabilize the $Cu_{11}In_9$ phase [139].
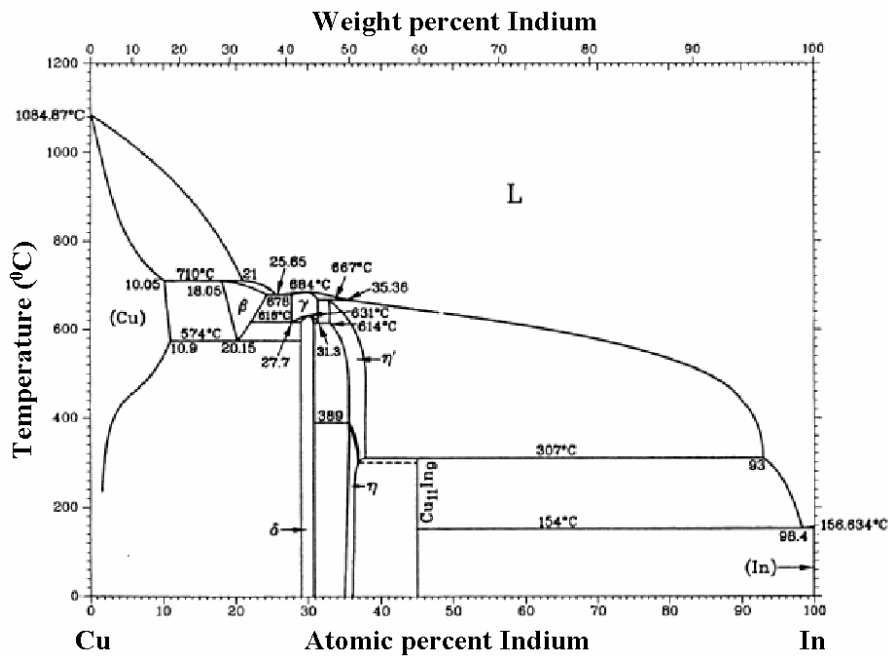

Fig. 4.11 Cu-In binary phase diagram [140]

Cu-In phase diagram is shown in figure 4.11. The melting points of In and Cu are 156.6^0C and 1085^0C, respectively. The copper indium alloy is

144

designated as $Cu_{11}In_9$ in the temperature range of approximately 157^0C to 310^0C and as "η" phase at temperatures between 310^0C to 440^0C. This phase is not clearly defined, and stoichiometric formulae of Cu_2In, Cu_7In_4 or $Cu_{2-x}In$ and $Cu_{16}In_9$ have been proposed. Most available literature on the deposition of Cu-In precursors attribute the high quality of Cu-In layers to the occurrence of a homogeneous single phase $Cu_{11}In_9$, which is used as a measure of the degree of alloying between copper and indium. Reexamination of several portions of the Cu-In phase diagram [141] revealed that the $Cu_{11}In_9$ phase is stable at low temperatures rather than decomposing at 157^0C.
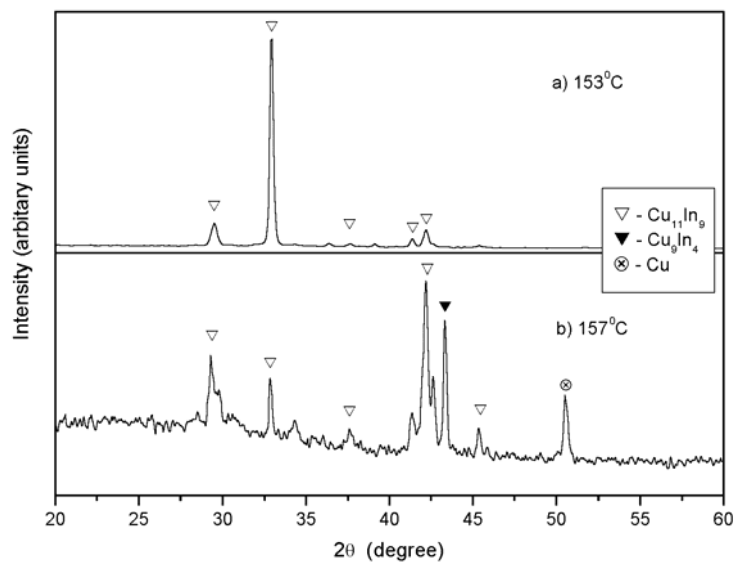

Fig. 4. 12 XRD patterns of $Cu_{11}In_9$ alloys prepared by annealing the In-Cu bilayers at 153^0C for 2hours (a) and at 157^0C for 2 hours (b)

The annealing time and temperature were optimized by various trials. It has been found that annealing temperature 153^0C for two hours result in $Cu_{11}In_9$ alloy. All the Cu rich as well as In rich precursors (Cu/In = 0.90 to 1.33) annealed at 153^0C for two hours in vacuum (2×10^{-5} mbar) showed X-ray diffraction peaks corresponding to $Cu_{11}In_9$ phases (Fig. 4.12). There are

some secondary phases of $Cu_{16}In_9$ also present in the precursor alloys. However no crystalline phases of metallic copper or indium was detected by x-ray diffraction. The annealing temperature above 153^0C showed the presence of metallic copper in the X-ray diffraction (XRD) spectra. This may be due to the loss of indium during the annealing which results in excess of copper. The reaction was not complete as evident from the XRD, when the annealing was done at a lower temperature ($<153^0C$) indicating the presence of metallic indium and copper in the precursors. The scanning electron micrograph (SEM) pictures show that all the precursor films have uniform surface. The surfaces are found to be more closely and orderly packed for indium rich precursors and near stoichiometric precursors. Where as the Cu rich precursors are found to be globular granules spreading uniformly over the surface (Fig. 4.13).
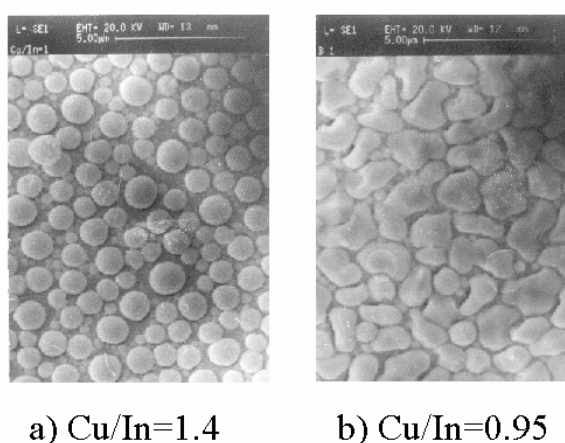
a) Cu/In=1.4   b) Cu/In=0.95

Fig. 4.13 SEM images of $Cu_{11}In_9$ alloys a) Cu/In =1.4 (copper rich) b) Cu/In=0.95 (indium rich)

4B.5.2 Sulphurisation processes

The sulphurisation was carried out by annealing the Cu-In precursors in H_2S atmosphere. The sulphurisation temperature (T_{sulph}) was varied from 250^0C to 400^0C. Duration of sulphurisation was also varied up to three hours.

During the entire thermal cycle the H_2S was passed through the reaction vessel. The sulphurisation set up is as shown in figure 2.4 in Chapter 2.

4B.6 Results and Discussion

4B.6.1 XRD phases

A set of identical samples were sulphurised at different temperatures. The Cu/In ratios in all these precursors were adjusted to be 0.99 and the duration of sulphurisation was kept as two hours. The sulphurisation temperature was varied from 250^0C–400^0C. The detected phases by XRD are reported in figure 4.14. The samples sulphursied at 250^0C show major peaks corresponding to InS phase together with $CuInS_2$, Cu_2S, In_6S_7 and CuS. As the annealing temperature is increased to 300^0C, XRD spectra indicate the beginning of the formation of copper indium sulphide phases. The binary InS and CuS phases were not present in these samples. The studies on sulphurisation of metallic indium layers shows that the formation of InS phases is favoured at lower sulphurisation temperatures, whereas the sulphurisation of metallic indium above 350^0C leads to the formation of In_2S_3 [142].

The sulphurisation of Cu-In alloys at 300^0C and above resulted in the CIS phase. But the presence of Cu_2S binary was also identified by XRD spectra for films sulphurised for two hours. The annealing of Cu-In alloys at 350^0C for three hours under H_2S atmosphere is found to be optimal for obtaining pure chalcopyrite CIS phase. The precursor with Cu/In ratio 0.9 (indium rich) and 1.2 (copper rich) also showed only diffraction peaks corresponding to the chalcopyrite CIS phase under this optimized annealing conditions. No secondary binary phases viz., CuS, Cu_2S or InS were detected by XRD in these films (Fig. 4.15). The grain size of the CIS films were calculated from the XRD spectra using the Scherrer's formula $D=0.9\lambda/\beta Cos\theta$, where $\lambda = 1.5418A^0$, β is the full width at half maximum intensity in radians. It has been found that the grain size is larger for the CIS films with Cu/In ratio close to unity or near stoichiometric films (Fig.4.16).
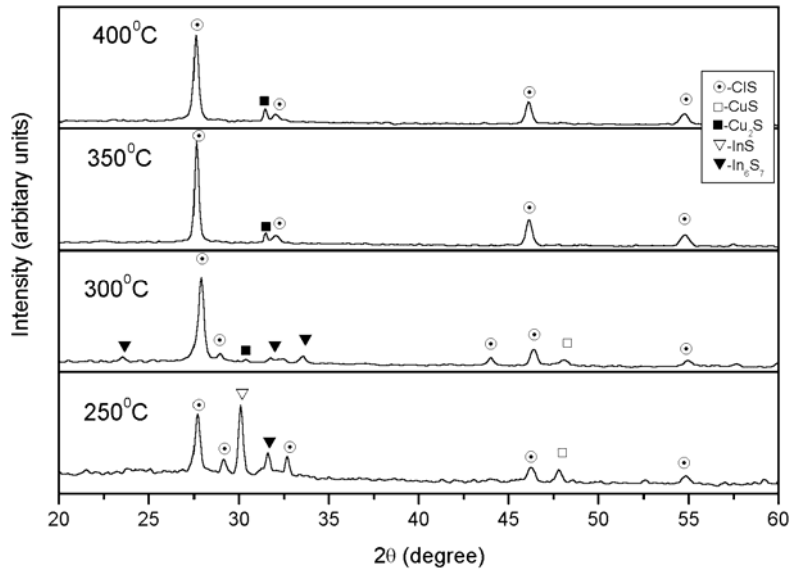
Fig.4.14 XRD patterns of CuInS$_2$ films prepared by sulphurisation of precursors with Cu/In = 0.99 for 2hours at different (T$_{sulph}$) temperatures.
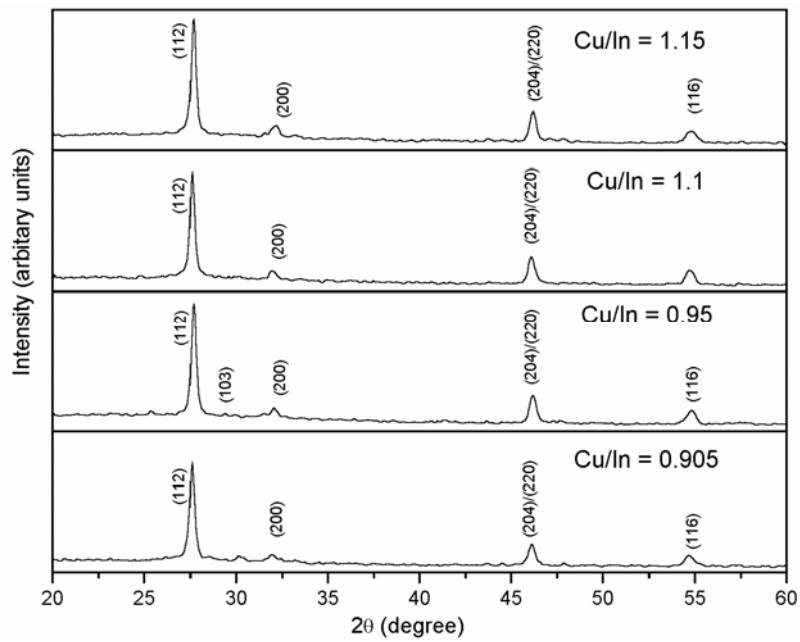

Fig.4.15. XRD patterns of single phase CuInS$_2$ films prepared by sulphurisation at 350^{0}C for 3 hrs using precursors with various Cu/In ratio

148

The grain size is also found to depend on the sulphurisation temperature. The inset of figure 4.16 shows the variation of grain size for the precursor with Cu/In ratio 0.99 with sulphurisation temperature, keeping the annealing time for 2hrs. The highest grain size is obtained for the sulphurisation condition of 350^0C for three hours and this suggests that the completion of reaction and formation of CIS. The grain size decreases as the sulphurisation temperature is increased beyond 350^0C. This may be due to the fact that the chemical path to CIS at sulphurisation temperature above and below 350^0C is different. The presence of Cu_2S is also observed in films sulphurised for short duration above 350^0C, where as InS, Cu_2S, CuS and In_6S_7 are detected at lower sulphurisation temperature, which is converted to $CuInS_2$ as described below (equations 1 and 2). Lattice constants c and a are determined from the XRD data and the ratio c/a is found to vary with the Cu/In ratio in the precursor. The value of c/a varied from 2.03 to 2.07.The c/a value was found to be maximum for Cu/In ratio near unity as shown in figure 4.17.
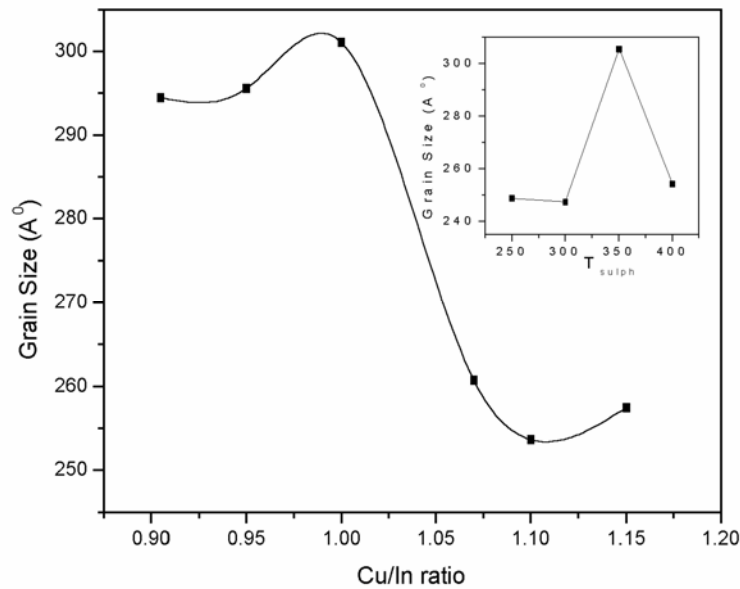
Fig.4.16 Variation of grain size of $CuInS_2$ films with Cu/In ratio in the precursor (T_{sulph}=350^0C for 3 hours). Inset shows the grain size variation of the CIS films with sulphurisation temperature (Cu/In=0.99)

149
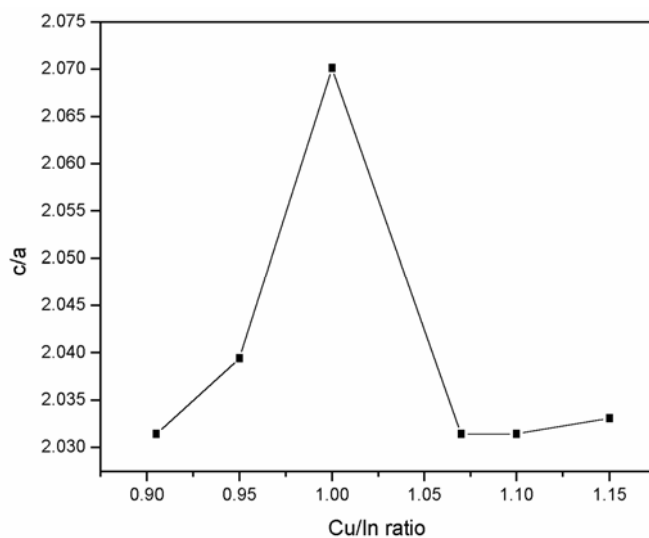
Fig.4.17 The variation of lattice constant ratio c/a of CuInS$_2$ films with Cu/In ratio

a) Cu/In=1.1   b) Cu/In=0.98
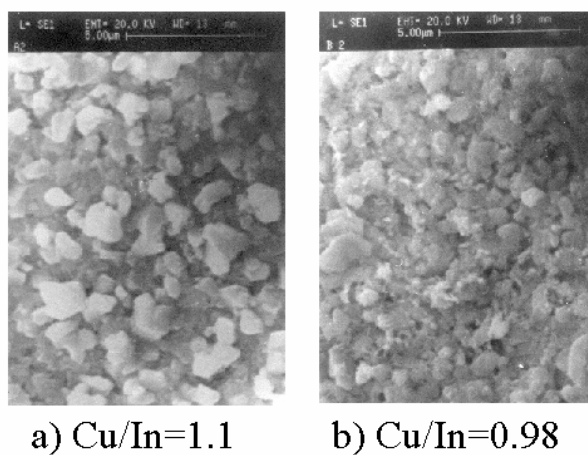
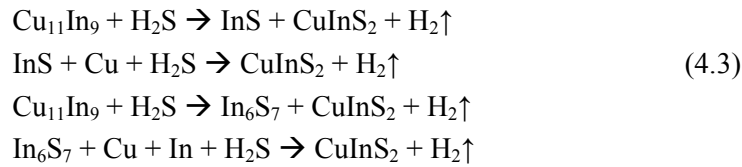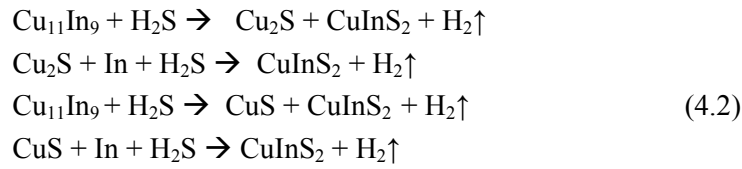**Fig.4.18** SEM images of CuInS$_2$ films prepared from precursors with Cu/In =1.1 (a) and 0.98(b)

4B.6.2 Morphology

The SEM micrographs of the CuInS$_2$ films with Cu/In ratio in the precursor 1.1and 0.98 sulphurised at 350^{0}C for three hours is shown in figure 4.18a

and figure 4.18b respectively. Generally the indium rich films are more densely packed than copper rich $CuInS_2$ films. There is no evidence for the presence of any secondary phase, which could be identified from the different crystal habits of the binary sulphides.

4B.6.3 Chemical path to CuInS₂

On sulphurisation, the copper rich precursors could be converted to CIS and the excess copper bound in the form CuS and Cu_2S while the Indium rich precursors it may be converted to CIS, In_6S_7 and InS. The possible reaction chains for the formation of stoichiometric $CuInS_2$ may be as given in equations (4.2) and (4.3).

$$Cu_{11}In_9 + H_2S \rightarrow Cu_2S + CuInS_2 + H_2\uparrow$$
$$Cu_2S + In + H_2S \rightarrow CuInS_2 + H_2\uparrow$$
$$Cu_{11}In_9 + H_2S \rightarrow CuS + CuInS_2 + H_2\uparrow \qquad (4.2)$$
$$CuS + In + H_2S \rightarrow CuInS_2 + H_2\uparrow$$

$$Cu_{11}In_9 + H_2S \rightarrow InS + CuInS_2 + H_2\uparrow$$
$$InS + Cu + H_2S \rightarrow CuInS_2 + H_2\uparrow \qquad (4.3)$$
$$Cu_{11}In_9 + H_2S \rightarrow In_6S_7 + CuInS_2 + H_2\uparrow$$
$$In_6S_7 + Cu + In + H_2S \rightarrow CuInS_2 + H_2\uparrow$$

4B.6.4 Electrical properties

The electrical conductivity was measured by two-probe method with evaporated indium as electrode in planar geometry using a Keithley source measure unit (Model SMU236). The nature of carriers was confirmed by the thermo power measurements. The CIS films prepared from the precursors with different Cu/In ratios show p-type conductivity as evident from the positive sign of the thermo power. The variation of resistivity of the CIS films having different Cu/In ratios in the precursor is shown in figure 4.19.
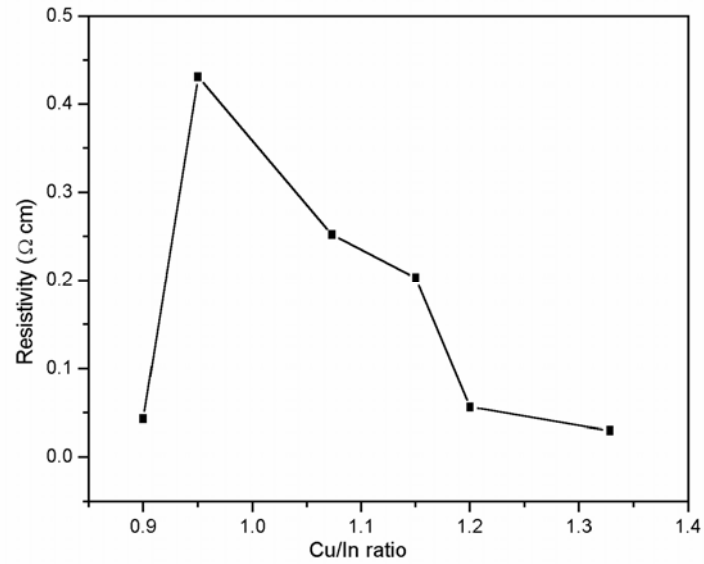
Fig.4.19. Variation of resistivity of $CuInS_2$ films with Cu/In ratio in the precursor
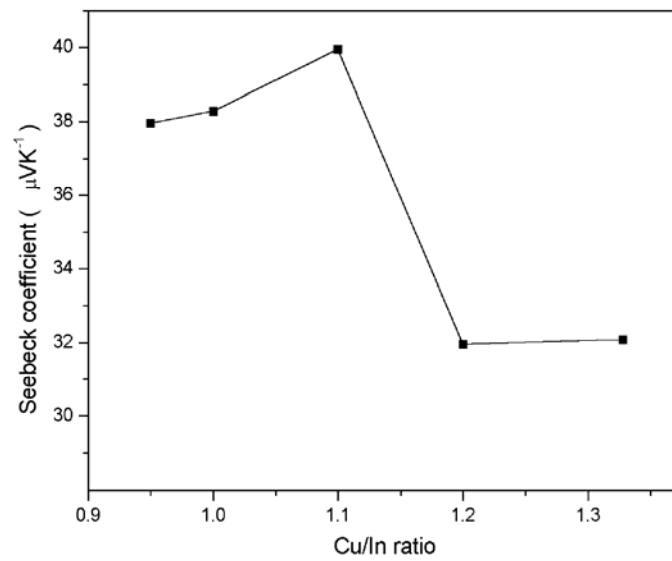
Fig.4.20. Variation of Seebeck coefficient of $CuInS_2$ films with Cu/In ratio

The compositional deviations of $CuInS_2$ prepared by the two-stage process from the ideal chemical formula can be expressed by non-stoichiometry,

$$\Delta z = \frac{2[S]}{[Cu]+3[In]}-1 \qquad\qquad (4.4)$$

The parameter Δz is related to electronic defects and would determine the type of majority charge carriers. Films with $\Delta z >0$ will behave as p-type material while $\Delta z<0$ will show n-type conductivity [143]. A set of CIS samples were analyzed for their composition using the energy dispersive X-ray. All the films with $\Delta z >0$ were p-type, as determined by thermoelectric measurement [see chapter 2 section 2.3.6] with a Seebeck coefficient around $+40\mu VK^{-1}$ for the stoichiometric CIS film. The variation of the Seebeck coefficient with the Cu/In ratio is shown in figure 4.20.
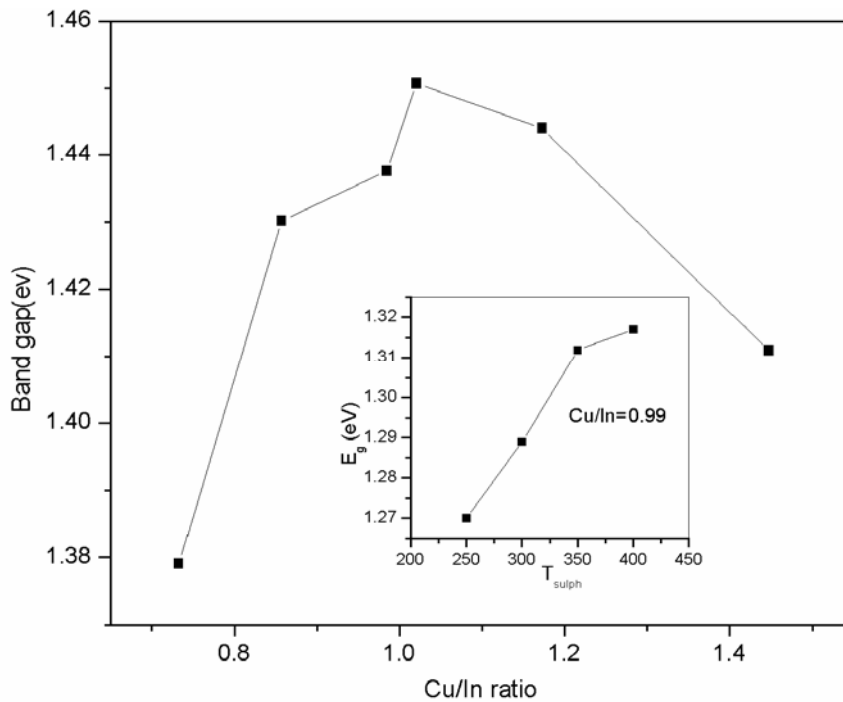
Fig.4.21 The band gap variation of CuInS$_2$ films with Cu/In ratio in the CIS films estimated from the EDAX spectra (T$_{sulph}$=350^{0}C for 3 hours). The inset shows the variation in band gap of CIS films with sulphurisation temperature for Cu/In=0.99 in the precursor, sulphurised for 2 hours.

4B.6.5 Optical properties

The transmission spectra of the films were recorded using uv-vis-nir spectrophotometer. Since $CuInS_2$ is a direct band gap material the band gap of the films were found out from the $(\alpha h\nu)^2$ against $h\nu$ plots as described in section 2.3.5. The optical band gap is found to depend on sulphurisation temperature, time and also on the Cu/In ratio in the CIS films (Fig 4.21). The composition of the CIS films and hence Cu/In ratio was found out by energy dispersive X-ray (EDAX) spectra. The band gap is found to increase with sulphurisation temperature and also with annealing duration. There is not much variation in the value of band gap when the sulphurisation temperature is 350^0C and above, and annealing duration is more than three hours. The inset of figure 4.21 shows the variation of optical band gap with sulphurisation temperate but keeping the duration for two hours and Cu/In ratio in the precursors equal to 0.99. The optical band gap increases with increase of Cu/In ratio and shows a maximum value of 1.45eV for the CIS films prepared from precursors with Cu/In ratio ~1 which is ideal for soar cell application.

The band gap decreases further on increasing the Cu/In ratio. The band gap 1.45eV is slightly less than that reported for single crystal value of 1.53 eV [144] but it closely matches with values reported for thin films [119,137] This also suggests that the optimised sulphurisation process for obtaining good chalcopyrite single phase CIS is sulphurising the near stoichiometric Cu/In precursors at 350^0C for 3 hrs.

4B.7 Conclusion

Single phase $CuInS_2$ thin films with chalcopyrite structure could be successfully grown by the two stage processes which involves the preparation of $Cu_{11}In_9$ alloy by annealing the evaporated copper and indium bilayers followed by the sulphurisation. The $Cu_{11}In_9$ precursor films are formed by the annealing of Cu-In bilayers at 153^0C in vacuum. The optimal sulphurisation conditions for the CIS formation are found to be the annealing

of Cu-In alloy at 350^0C in the presence of H$_2$S for three hours. Under these conditions, the sulphurisation of precursor with Cu/In ratio ~1 resulted in larger grain single phase CIS with a band gap 1.45 eV, ideal for the application as absorber layer in solar cells. The two stage process thus optimised for the growth of CuInS$_2$ films has now been utilised for the fabrication of Mo/CuInS$_2$/CdS solar cell which has an efficiency of 5.6% [145].

References

[1] M.L. Fairgeiley, Solar cells 16 (1986) 91

[2] J.R. Tuttle, D. S. Albin, R. Noufi, Solar Cells 30(1991) 21

[3] R.W. Birkmire and E. Eser, Annu. Rev. Mater. Sci. 27 (1997) 625

[4] Powder Diffraction Files, Card 40-1487, International Centre for Diffraction Data

[5] D. Schmid, M. Ruckh, F. Grunwald and H.W. Schock, J. Appl. Phys., 73 (1993) 2902

[6] H.W. Schock and U. Rau, Physica B 308-310 (2001) 1081

[7] R. Caballero and C. Guillen, Thin Solid Films 403-404 (2002) 107

[8] M. Marudachalam, H. Hichri, R. Klenk, R.W. Birkmire, W.N. Shafarman and J.M. Schultz, Appl. Phys. Lett. 67 (1995) 3978

[9] M. Klenk, O. Schenker, V. Alberts and E. Bucher, Semicond. Sci. Technol. 17 (2002) 435

[10] W.E. Devaney, W.S. Chen, J.M. Stewart and R.A. Mickelsen, IEEE Trans. Electron Dev. 37 (1990) 428

[11] M.A. Contreras, J. Tuttle, A. Gabor, A. Tennant, K. Ramanathan, S. Asher, A. Franz, J. Keane, L. Wang, J. Scofield and R. Noufi, in: Proc. 1st World Conf. Photovolt. Energy Conv., Waikoloa, Hawaii (1994) p68

[12] A.M. Gabor, J.R. Tuttle, D.S. Albin, M.A. Contreras and R. Noufi, Appl. Phys. Lett. 65 (1994) 198

[13] M.A. Contreras, B. Egaas, K. Ramanathan, J. Hiltner, A. Swartzlander, F. Hasoon, and R. Noufi, Prog. Photovolt.: Res. Appl. 7 (1999) 311

[14] T. Negami, Y. Hashimoto and S. Nishiwaki, Sol. Energy Mater. Sol. Cells 67 (2001) 331

[15] [85] Y. Hagiwara, T. Nakada and A. Kunioka, Sol. Energy Mater. Sol. Cells 67 (2001) 267

[16] K. Ramanathan K, M.A. Contreras, C.L. Perkins, S. Asher, F.S. Hasoon, J. Keane, D. Young, M. Roberto, W. Metzger, R. Noufi, J. Ward, A. Duda, Prog. Photovolt: Res. App., 11 (2003) 225

[17] T. Nakada and M. Mizutani, Jpn. J. Appl. Phys., 41 (2002) L165

[18] M.A. Contreras, B. Egaas, D. King, A. Schwartzlander and T. Dullweber, Thin Solid Films 361-362 (2000) 167

[19] S. Niki, A. Yamada, R. Hunger, P.J. Fons, K. Iwata, K. Matsubara, A. Nishio and H. Nakanishi, J. Cryst. Growth 237-240 (2002) 1993

[20] A.N. Tiwari, S. Blunier, K. Kessler, V. Zelezny and H. Zogg, Appl. Phys. Lett. 65 (1994) 2299

[21] I.Sanayal, K.K. Chattopadyay, S. Chaudhuri and A.K. Pal, J.Appl. Phys. 70 (1991) 841

[22] R.Pal, K.K. Chattopadyay, S.Chaudhuri and A.K. Pal, Thin Solid Films 254(1995) 111

[23] R.Pal, K.K. Chattopadyay, S.Chaudhuri and A.K. Pal, Sol.Energy Mater. Sol.Cells 33(1994) 241

[24] T. Negami, T. Satoh, Y. Hashimoto, S. Shimakawa, S. Hayashi, M. Muro, H. Inoue and M. Kitagawa, Thin Solid Films 403-404 (2002) 197

[25] F.O. Adurodija, J. Song, S.D. Kim, S.H. Kwon, S.K. Kim, K.H. Yoon and B.T. Ahn, Thin Solid Films 338 (1999) 13

[26] M. Marudachalam, R.W. Birkmire, H. Hichri, J.M. Schultz, A. Swartzlander and M.M. Al-Jassim, J. Appl. Phys., 82 (1997) 2896

[27] C. Guillen, M.A. Martinez and J. Herrero, Vacuum 58 (2000) 594

[28] O.F. Yuksel, B.M. Basol, H. Safak and H. Karabiyik, Appl. Phys. A, 73 (2001) 387

[29] A.G. Chowles, J.H. Neethling, H. van Niekerk, J.A.A.Engelbrecht and V.J. Watters, Renew. Energy 6 (1995) 613

[30] S. Bandyopadhyaya, S. Roy, S. Chaudhuri and A.K. Pal, Vacuum 62 (2001) 61

[31] C. Guillen and J. Herrero, Sol. Energy Mater. Sol. Cells 73 (2002) 141

[32] M.S. Sadigov, M. Ozkan, E. Bakacsiz, M. Altunba and A.I. Kopya, J. Mater. Sci.34 (1999) 4579

[33] T.L. Chu, S.S. Chu, S.C. Lin and J. Yue, J. Electrochem. Soc. 131 (1984) 2182

[34] J. Bekker, V.Alberts and M.J. Witcomb, Thin Solid Films 387 (2001) 40

[35] S.F. Chichibu, M. Sugiyama, M. Ohbasami, A. Hayakawa, T. Mizutani, H. Nakanishi, T. Negami and T. Wada, J. Cryst. Growth 243 (2002) 404

[36] A. Garg, K.S. Balakrisnan and A.C. Rastogi, J. Electrochem. Soc. 141 (1994) 1566

[37] A.C. Rastogi, K.S. Balakrisnan, R.K. Sharma and K. Jain, Thin Solid Films 357 (1999) 179

[38] C. Guillen and J. Herrero, Thin Solid Films 323 (1998) 93

[39] V. Alberts, M. Klenk and E. Bucher, Thin Solid Films 387 (2001) 44

[40] M.E. Calixto and P.J. Sebastian, J. Mater. Sci. 33 (1998) 339

[41] G.Hodes, T.Engelhardt, D. Cahen, L.L. Kazmerski and C.R. Herrington, Thin Solid Films 128 (1985) 93

[42] S.R.Kumar, R.B.Gore and R.K.Pandey,Thin Solid Films 223 (1993) 109

[43] H.P. Fritz and P. Chatziagorastou, Thin Solid Films 247 (1994) 129

[44] V.K. Kapur, B.M. Basol and E.S. Tseng, Sol. Cells 21 (1987) 65

[45] P.P. Prosini, M.L. Addonizio, A. Antonaia and S. Loreti, Thin Solid Films, 288 (1996) 90

[46] M. Altosaar, E. Mellikov, J. Kois, Y. Guo and D. Meissner, in: Proceedings of Joint International Meeting of The Electrochemical Society, Inc. and The International Society of Electrochemistry, Paris, France (1997) p1314

[47] C.D. Lokhande, Bull. Electrochem. 4 (1988) 131

[48] V. Probst, W. Stetter, W. Riedl, H. Vogt, M. Wendl, H. Calwer, S. Zweigart, K.-D. Ufert, B. Freienstein, H. Cerva and F. Karg, Thin Solid Films 387 (2001) 262

[49] K. Kushiya, Thin Solid Films, 387 (2001) 257

[50] K. Kushiya, M. Tachiyuki, Y. Nagoya, A. Fujimaki, B. Sang, D. Okumura, M. Satoh and O. Yamase, Sol. Energy Mater. Sol. Cells, 67 (2001) 11

[51] F.H. Karg, Sol. Energy Mater. Sol. Cells, 66 (2001) 645

[52] A.Parretta, M.L. Addonizio, S.Loreti, Quercia and M.K. Jayaraj, Journal of Crystal Growth 183, 196 (1998).

[53] B.M. Basol, A. Halani, C. Leidholm, G. Norsworthy, V.K. Kapur, A. Swartzlander and R.Matson in: Prog. Photovolt.:Res.Appl.,8 (2000) 227

[54] J. Keranen, J. Lu, J. Barnard, J. Sterner, J. Kessler, L. Stolt, T.W. Matthes and E. Olsson, Thin Solid Films, 387 (2001) 80

[55] T.J. Gillespie, C.H. Marshall, M.Contreras and J. Keane, Sol. Energy Mater. Sol. Cells 59 (1999) 27

[56] A.M. Hermann, M. Mansour, V. Badri, B. Pinkhasov, C. Gonzales, C., F. Fickett, M.E. Calixto, P.J. Sebastian, C.H. Marshall and T.J. Gillespie, Thin Solid Films, 361-362 (2000) 74

[57] A.M. Hermann, C. Gonzalez, P.A. Ramakrishnan, D. Balzar, C.H. Marshall, J.N. Hilfiker and T. Tiwald, Thin Solid Films 387 (2001) 54

[58] S.C. Park, D.Y. Lee, B.T. Ahn, K.H. Yoon and J. Song, Sol. Energy Mater. Sol. Cells 69 (2001) 99

[59] D.Y. Lee, J.H. Yun, B.T. Ahn, K.H. Yoon and J. Song, in: Proc. Mater. Res. Soc. Symp. 668 (2001) H8.8.1-6

[60] A.Ashida, Y. Hachiuma, N. Yamamoto, T. Ito and Y. Cho, J. Mater. Sci. Lett. 13 (1994) 1181

[61] M. Klenk, O. Schenker, V. Alberts and E. Bucher, Thin Solid Films 387 (2001) 47

[62] J.M. Merino, M. Leon, F. Rueda and R. Diaz, Thin Solid Films 361-362 (2000) 22

[63] H. Sakata and H. Ogawa, Sol. Energy Mater. Sol. Cells 63 (2000) 259

[64] A.A.S. Akl, A. Ashour, A.A. Ramadan and K.A. El-Hady, Vacuum, 61 (2001) 75

[65] C.M. Joseph and C.S. Menon, J. Phys. D: Appl. Phys., 34 (2001) 1143

[66] P. Victor, J. Nagaraju and S.B. Krupanidhi, Solid State Comm. 116 (2000) 649

[67] S. Kuranouchi and A. Yoshida, Thin Solid Films 343-344 (1999) 123

[68] J. McAleese, P. O'Brien and D.J. Otway, Chem. Vap. Deposition 4 (1998) 94

[69] P.A. Jones, A.D. Jackson, P.D. Lickiss, R.D. Pilkington and R.D. Tomlinson, Thin Solid Films 238 (1994) 4

[70] S. Duchemin, M.C. Artaud, F. Ouchen and J. Bougnot, J. Mater. Sci.: Mater. Electron. 7 (1996) 201

[71] M.C. Artaud, F. Ouchen, L. Martin and S. Duchemin, Thin Solid Films 324 (1998) 115

[72] G. Masse, K. Djessas, C. Monty and F. Sibieude, Thin Solid Films 414 (2002) 192

[73] G.W. El Haj Moussa, K.A. Ariswan, F. Guastavino and C. Llinares, Solid State Comm. 122 (2002) 195

[74] R.N. Bhattacharya, J. Electrochem. Soc. 130 (1983) 2040

[75] R.N. Bhattacharya, W. Batchelor, J.E. Granata, F. Hasoon, H. Wiesner, K. Ramanathan, J. Keane and R.N. Noufi, Sol. Energy Mater. Sol. Cells 55 (1998) 83

[76] J.C.Garg, R.P.Sharma and K.C.Sharma,Thin Solid Films 164(1988) 269

[77] K.T.R. Reddy, R.B.V. Chalapathy, M.A. Slifkin, A.W. Weiss and R.W. Miles, Thin Solid Films 387 (2001) 205

[78] S. Shirakata, Y. Kannaka, H. Hasegawa, T. Kariya and S. Isomura, Jpn. J. Appl. Phys. 38 (1999) 4997

[79] L. Thouin, S. Massaccesi, S. Sanchez and J. Vedel, J. Electroanal. Chem. 374 (1994) 81

[80] T. Pottier and G. Maurin, J. Appl. Electrochem. 1 9 (1989) 361

[81] A.N. Molin, A.I. Dikusar, G.A. Kiosse, P.A. Petrenko, A.I. Sokolovsky and Yu.G. Saltanovsky, Thin Solid Films 237 (1994) 66

[82] A.N. Molin and A.I. Dikusar, Thin Solid Films 237 (1994) 72

[83] R.N. Bhattacharya, J.F. Hiltner, W. Batchelor, M.A. Contreras, R.N. Noufi and J.R. Sites, Thin Solid Films 361-362 (2000) 396

[84] R.N. Bhattacharya, W. Batchelor, K. Ramanathan, M.A. Contreras and T. Moriarty, Sol. Energy Mater. Sol. Cells 63 (2000) 367

[85] P. Garg, A. Garg, A.C. Rastogi and J.C. Garg, J. Phys. D: Appl. Phys. 24 (1991) 2026

[86] S.N. Sahu, R.D.L. Kristensen and D. Haneman, Sol. Energy Mater. 18 (1989) 385

[87] Y. Sudo, S. Endo and T. Irie, Jpn. J. Appl. Phys. 32 (1993) 1562

[88] M.C.F. Oliveira, M. Azevedo and A. Cunha, Thin Solid Films 405 (2002) 129

[89] M.G. Ganchev and K.D. Kochev, Sol. Energy Mater. Sol. Cells 31 (1993) 163

[90] E. Tzvetkova, N. Stratieva, M. Ganchev, I. Tomov, K. Ivanova and K. Kochev, Thin Solid Films 311 (1997) 101

[91] T. Edamura and J. Muto, J. Mater. Sci., 5 (1994) 275

[92] S.N. Qiu, L. Li, C.X. Qiu, I. Shih and C.H. Champness, Sol. Energy Mater. Sol. Cells 37 (1995) 389

[93] S.N. Qiu, W.W. Lam, C.X. Qiu and I. Shih, Appl. Surf. Sci., 113-114 (1997) 764

[94] C.X. Qiu and I. Shih, Can. J. Phys. 65 (1987) 1011

[95] Akhlesh Gupta, Sho Shirakata and Shigehiro Isomura, Sol. Energy Mater. Sol. Cells 32 (1994) 137

[96] S.Isomura,S.Shirakata and T.Abe, Solar Energy Materials 22 (1991) 223

[97] H. Sakata and N.Nakao, Phys. Stat. Sol.(a) 161 (1997) 379

[98] J.Bardeen, F.J.Blatt and L.H. Hall, in: Proceedings of Photoconductivity Conf., Atlantic City, 1954, Eds R.Breckenridze, B.Russel and T.Hahn, (J.Wiley and Chapman and Hall , New York ,1956) p146.

[99] J.L. Shay, B.Tell, H.M. Kasper and L.M. Schiavone, Phys.Rev.B 7 (1973) 4485

[100] H. Sakata and H. Ogawa, Solar Cells 63 (2000) 259

[101] V. Alberts, R. Herberholz, T Walter and H.W. Schock, J.Phys.D: Appl.Phys. 30 (1997) 2156

[102] A. Catalano, Sol. Energy Mater. Sol. Cells 41/42 (1996) 205

[103] T. Walter, D. Baunger, D. Hariskos, Ch. Koble, H.W. Shock, in: Proc. 13th Europ. Photov. Sol. Energy Conf. (Nice, 1995) p597

[104] R. Klenk, P. Dobson, M. Falz, N. Janke, I. Luck, A. Perez-Rodryguez, R. Scheer and E. Terzini, in: Proc. of 16th EPVSEC, 2000.

[105] K. Siemer, J. Klaer, I. Luck, J. Bruns, R. Klenk, and D. Braunig, Sol. Energy Mater. Sol. Cells 67 (2001) 159

[106] S. Siebentritt, Thin Solid Films 403-404 (2002) 1

[107] J.J.M. Binsma, L.J. Giling and J. Bloem, J. Cryst. Growth 50 (1980) 429

[108] M.Kanzari and B.Rezig, Semicond.Sci.Technnol.15 (2000) 335

[109] L.L. Kazmerski, M.S. Ayyagari and G.A. Sanborn, J. Appl. Phys. 46 (1975) 4865

[110] L.L. Kazmerski, F.R. White, M.S. Ayyagari, Y.J. Juang and R.P. Patterson, J. Vac. Sci. Technol. 14 (1977) 65

[111] L.L. Kazmerski and G.A. Sanborn, J. Appl. Phys. 48 (1977) 3178

[112] R. Scheer, T. Walter, H.W.Schock, M.L Fearheily and H.J. Lewerenz, Appl. Phys. Lett. 63 (1993) 3294

[113] R. Scheer, M. Alt, I. Luck and H.J. Lewerenz, Sol. Energy Mater. Sol. Cells 49(1997) 423

[114] H. Metzner, U. Reislohner, J. Cieslak, W. Witthuhn, T. Hahn and J. Kraublich, Thin Solid Films 403-404 (2002) 13

[115] D. Braunger, D. Hariskos, T.Walter and H.W. Schock, Sol. Energy Mater. Sol. Cells 40 (1996) 97

[116] Y.L. Wu, H.Y. Lin, C.Y. Sun, M.H. Yang and H.L. Hwang, Thin Solid Films 168 (1989) 113

[117] M.K. Agarwal, P.D. Patel, S.H. Chaki and D. Lakshminarayana, Bull. Mater. Sci. 21 (1998) 291

[118] H. Neumann, W. Horig, V. Savelev, J. Lagzdonis, B. Schumann and G. Kuhn, Thin Solid Films 79 (1981) 167

[119] M.Gosslla, H.-E. Mahnke and H.Metzner, Thin Solid Films, 361-362 (2000) 56

[120] M.Gosslla,H.Metzner and H.-E.Mahnke,Thin Solid Films, 387(2001) 77

[121] Y. Ogawa, S. Uenishi, K. Tohyama, K. Ito, Sol. Energy Mater. Sol. Cells 35(1994) 157

[122] Y. Ogawa, A.J. Waldau, Y. Hashimoto and K. Ito, Jpn. J. Appl. Phys. 33 (1994) L1775

[123] T. Nakabayashi, T. Miyazawa, Y. Hashimoto and K.Ito, Sol. Energy Mater. Sol. Cells 49 (1997) 375

[124] R. Scheer, I. Luck, H.Sehnert and H.J. Lewerenz, Sol. Energy Mater. Sol. Cells 41/42 (1996) 261

[125] S. Bandyopadhyaya, S. Chaudhuri and A.K. Pal, Sol. Energy Mater. Sol. Cells 60 (2000) 323

[126] R. Klenk, U.Blieske, V. Dieterle, K. Ellmer, S. Fiechter, I. Hengel, A.J. Waldau, T. Kampschulte, C. Kaufmann, J. Klaer, M.C.L. Steiner, D. Braunger, D.Hariskos, M.Ruckh and H.W. Schock, Sol. Energy Mater. Sol. Cells 49 (1997) 349

[127] Y. Onuma, K. Takeuchi, S. Ichikawa, M. Harada, H. Tanaka, A. Koizumi and Y. Miyajima, Sol. Energy Mater. Sol. Cells, 69 (2001) 261

[128] S.P. Grindle, C.W. Smith and S.D. Mittleman, Appl. Phys. Lett. 35 (1979) 24

[129] J. Herrero and J. Ortega, Sol. Energy Mater. Sol. Cells 20 (1990) 53

[130] C. Dizionk, H. Metzner, S. Hessler and H.-E. Mahnke, Thin Solid Films 299 (1997) 38

[131] T. Negami, Y. Hashimoto, M. Nishitani and T. Wada, Sol. Energy Mater. Sol. Cells 49 (1997) 343

[132] T. Wada, T. Negami and M. Nishitani, J. Mater. Res. 8 (1993) 545

[133] Y.B. He, A. Polity, H.R. Alves, I. Osterreicher, W. Kriegseis, D. Pfisterer, B.K. Meyer and M.Hardt, This Solid films 403-404 (2002) 62

[134] A.N. Tiwari, D.K. pandya and K.L. Chopra, Thin Solid films 130 (1985) 217

[135] A.N. Tiwari, D.K. Pandya and K.L. Chopra, Sol. Energy Mater. 15 (1987) 121

[136] M. Krunks, V. Mikli, O.Bijakina, H.Rebane, A. Mere, T. Varema and E. Mellikov, Thin Solid Films 361-362 (2000) 61

[137] H. Gonzalez-Hernandez, P.M. Gorley, P.P. Horley, O.M. Vartsabyuk and Y.V. Vorobiev, Thin Solid Films 403-404 (2002) 471

[138] S. Bini, K. Bindu, M. Lakshmi, C.S. Kartha, K.P. Vijayakumar, Y. Kashiwaba and T. Abe, Renewable Energy 20 (2000) 405

[139] P.R.Subramanian and D.E. Laughlin, Bulletin of alloy phase diagrams10 (5) (1989) 554

[140] H. Okamoto, Journal of Phase Equilibria 15(2) (1994)

[141] A. Bolcovage , S. W. Chen, C. R. Kao, Y.A. Chang and A. D. Romig, J. Phase Equilibria 14 (1993) 14.

[142] R. Yoosuf, K.C. Jerome, A. Antony, R. Manoj and M. K. Jayaraj, (Eds) C. Hasnain, J. Connie, D. Huang, Y. Nakano, R. Xiaomin, Materials, Active Devices, and Optical Amplifiers, Proceedings of the SPIE 5280 (2004) p669

[143] H.Y. Ueng, H.L. Hwang, J. Appl. Phys. 62 (1987) 434

[144] A. Rocket, R.W. Brikmire, J. Appl. Phys. 70 (1991) R81

[145] A.S.Asha, Rahana Yoosuf, G.Sukesh, Aldrin Antony and M.K. Jayaraj, Int.Conference. on Electrochem. Power System – 2 (Hyderabad, India, December 2004)

CHAPTER 5

Preparation and characterisation of indium tin oxide thin films by rf magnetron sputtering

Indium tin oxide thin films were deposited onto glass substrates by rf magnetron sputtering at room temperature. Effect of annealing on the structural, electrical and optical properties was investigated. By vacuum annealing highly conducting and transparent films were obtained. The dependence of film properties on the substrate to target distance was also studied. Films deposited with a target to substrate spacing of 4cm showed the lowest resistivity of $3.07x10^{-3}$ Ω cm and maximum band gap of 3.89eV on annealing at a temperature of 250^0C under high vacuum for 1 hour.

5.1 Introduction

Nowadays, transparent conducting metal oxides (TCO) are used almost exclusively as the top contacts in CIS based solar cells. Narrow lined metal grids (Ni-Al) are usually deposited on top of the TCO in order to reduce the series resistance. The requirements for the electrical top contact of a CIS device are; sufficient transparency in order to let enough light to the underlying parts of the device, i.e. its band gap must be high enough, and sufficient conductivity to be able to transport the photogenerated current to the circuit without too much resistance losses. It also serves as the antireflection coating for the active region. Tin doped indium oxide (ITO) is one of the widely used transparent conducting front contacts for solar cells.

5.2 ITO – An overview of present status

Interest in transparent conductors can be traced back to 1907 when reports on transparent and conductive cadmium oxide (CdO) films first appeared [1]. Since then there has been a growing technological interest in materials with these unique properties as evidenced by not only their increased numbers but also the large variety of techniques that have been developed for their deposition. It is now known that non-stoichiometric and doped films of oxides of tin, indium, cadmium, zinc and their various alloys exhibit high transmittance and nearly metallic conductivity is achievable in them [2]. However, tin doped indium oxide (ITO) is the most popular among these thin films, which have found a host of electronic, opto-electronic and mechanical applications. Hence, some of the physical and technological aspects behind ITO films deposition and characterisation will be discussed in this chapter.

Although partial transparency with acceptable conductivity can be obtained for very thin metallic films, high transparency and simultaneously high conductivity cannot be attained in intrinsic stoichiometric materials. The only way this can be achieved is by creating electron degeneracy in a wide band gap ($E_g > 3eV$ for transparent to visible radiation) material by

introducing non-stoichiometry and/or appropriate dopants. These conditions can be conveniently met for ITO as well as a number of other materials previously mentioned.

Uses of ITO have traditionally ranged from transparent heating elements of aircraft and car windows, antistatic coatings over electronic instrument display panels, heat reflecting mirrors, antireflection coatings and even in high temperature gas sensors. Early electro-optic devices using ITO include CCD arrays, liquid crystal displays and transparent electrodes for various display devices. More recently, ITO has been used as a transparent contact in advanced optoelectronic devices such as solar cells, light emitting and photo diodes, phototransistors etc. Thus it is becoming an integral part of modern electronic technology wherever there is a potential for improving optical sensitivity of light detecting devices or quantum efficiency of light emitting devices.

Indium tin oxide is a highly degenerate n-type semiconductor with a reported low electrical resistivity of 8.45×10^{-5} Ωcm [3]. ITO is a wide band gap (3.3–4.3 eV) material, which shows high transmittance in the visible and near IR regions of the spectrum. Their high conductivity results from the non-stoichiometry produced by oxygen deficiency and the introduction of tin as dopant [4]. Because of these characteristics, ITO films are widely used in opto-electronic applications, such as transparent electrodes in liquid crystal displays, ferro-electric photo conductor storage devices and photovoltaic devices. ITO films have good efficiency for hole injection into organic materials, and hence they are widely utilised as the transparent conducting anode contact for organic light emitting diodes [5].

ITO films can be prepared by a wide variety of techniques such as plasma enhanced metallorganic chemical vapour deposition (PEMOCVD) [6], ion assisted deposition [7], sputtering [8], Pulsed Laser Deposition (PLD) [3], dip coating [9] etc. Sputtering is one of the effective methods to obtain good quality ITO thin films. It is superior in both its controllability and the uniformity of the films deposited on a large area substrate [10]. Reports also

show that good quality polycrystalline ITO films can be grown at room temperature by adopting PLD technique coupled with laser irradiation of substrate [11]. Production of low resistivity films at room temperature is of importance in high performance Flat Panel Displays (FPDs), which use heat sensitive substrates such as polymers.

The optical and electrical properties of the films depend strongly on the preparation technique. Theoretical understanding of ITO has been limited especially on the electronic band structure level, even though some results have been known about electronic structure, defect chemistry and carrier generation mechanisms [12]. The deposition of ITO in a manufacturing environment is typically by means of dc-magnetron sputtering [13]. The choice of target – ceramic or metal – depends on the film quality sought and the process control available. The variables adjusted during process optimization include oxygen partial pressure, total gas pressure, residual water-vapour partial pressure, substrate temperature and target temperature (due to unintentional heating), sputter power, and target composition and configuration. The goals are the minimization of micro structural features and impurities that lead to reduced electron mobility, the maximization of substitutional Sn, and the creation of optimal oxygen sub stoichiometry. The oxygen non-stoichiometry is critical to the minimization of resistivity, since each doubly charged oxygen vacancy contributes two free electrons [13].

Indium Tin Oxide is essentially formed by substitutional doping of In_2O_3 with tin, which replaces the In^{3+} atoms from the cubic bixbyite structure of indium oxide [14]. Sn thus forms an interstitial bond with oxygen and exists either as SnO or SnO_2 – accordingly it has a valency of +2 or +4 respectively. This valency state has a direct bearing on the ultimate conductivity of ITO. The lower valence state results in a net reduction in carrier concentration, since a hole is created which acts as a trap and reduces conductivity. On the other hand, predominance of the SnO_2 state means Sn^{4+} acts as an n-type donor releasing electrons to the conduction band. However, in ITO, both substitutional tin and oxygen vacancies contribute to the high conductivity and the material can be represented as $In_{2-x}Sn_xO_{3-2x}$.

168

Indium tin oxide prepared by various techniques is found to be polycrystalline always. ITO has a structure of bulk undoped In_2O_3. The lattice constant value of ITO is found to be larger than those of the bulk undoped In_2O_3. The amount of increase in lattice constant is found to depend on the deposition parameters. Lattice constant value strongly depends on oxygen partial pressure during sputtering process. ITO films in general are found to exhibit a strong (111) or (100) preferred orientations depending on deposition conditions [12].

Odaka et al. [15] used first principles band structure calculations to show that tin atom replacing an indium atom – irrespective of its site – leads to the formation of three impurity bands with s-like symmetry. One of these bands overlaps the conduction band of In_2O_3, and the Fermi level of ITO is located in this band, thus essentially accounting for the free electron like properties. Further more, it was found that the Sn substitution did not significantly destroy the shape of the density of states around the bottom of the conduction band. A quantitative theoretical model explaining the optical properties of ITO has been reported by Granqvist et al. [16]. In the ultraviolet region of the ITO, the absorption is strong due to excitations across the fundamental band gap E_g. Substitutional doping of Sn on In sites in the In_2O_3 lattice shifts E_g towards shorter wavelengths. This phenomenon is due to the Burstein-Moss effect, i.e. a blocking of the lowest states in the conduction band, which is partly balanced by many body effects [17,18].

Indium oxide films are generally doped with tin because Sn^{4+} substitutes for In^{3+} cation creating donor level in the energy band gap. Tin doping of indium oxide films decreases the electrical resistivity of the films. All tin doped indium oxide films have n-type conductivity. For optoelectronic applications, the transparent conductor must be carefully processed to maximize optical transparency in the visible regime, while achieving minimum electrical resistivity. The window of transparency in ITO extends from the band gap on the UV end to the plasma-absorption frequency at the IR end [13]. When the oxide is degeneratively doped, increasing carrier

density leads to a widening of the band gap due to the Burstein-Moss effect. The IR end of the transparency window is defined by the plasma-absorption frequency, which depends on the carrier density and the effective mass of the carrier.

The values of electrical parameters strongly depend on the dopant concentration, deposition and post-deposition process conditions. The decrease in mobility with increase of dopant level is due to enhancement of scattering mechanisms such as ionized impurity scattering. The substrate temperature is found to significantly affect the electrical properties [13]. The resistivity initially decreases as the substrate temperature increases. This type of dependence of resistivity on substrate temperature may be due to the fact that crystallinity of the films improves with increase in substrate temperature, thereby increasing conductivity. At higher substrate temperatures the resistivity increases again. This increase in resistivity may be due to the oxidation of tin doped indium oxide films. Oxidizing or reducing conditions will modify the oxygen-vacancy concentration and hence the carrier density. Increasing the substrate temperature creates more oxygen vacancies and hence higher conductivity [13].

ITO has good substrate compatibility. ITO thin films can be deposited at room temperature, and in general, its adhesion to most substrates is excellent. The deposition of ITO onto silicon for use in solar cell applications can lead to the formation of an interfacial layer of SiO_2 as indium oxide is reduced by silicon [19].

Low substrate temperatures and low oxygen partial pressures during low-power sputter deposition will result in amorphous or partially amorphous material [20]. Remarkably, amorphous indium oxide crystallizes rapidly at temperatures as low as 150^0C with a change in electronic band structure [21]. Low substrate temperatures and high deposition rates severely limit the quality of the as-deposited ITO films by reducing the activation efficiency of the tin dopant and by producing more highly defect microstructures.

Inactivated tin decreases the electron mobility through impurity scattering and does not increase the carrier density [13].

ITO films deposited by evaporation and sputtering at room temperature are reported to be generally amorphous or composed of very small grains, therefore showing low transparency and high resistivity. In the case of sputter-deposited films, better quality can be achieved by substrate heating or by introducing oxygen during sputtering. But the presence of too much oxygen will increase the resistivity [22]. When In_2O_3–SnO_2 targets are used for sputtering better stoichiometric films have been obtained [23,24]. Generally post deposition annealing is not essential when ITO films are grown from oxide targets. Oxygen is usually added to the sputtering gas in order to improve the structural, electrical and optical properties. But such an improvement is possible only when the oxygen partial pressure is low and within a narrow pressure range, typically (2–4) x 10^{-5} Torr. Films deposited at low temperature are amorphous in nature, whereas films deposited at higher temperature (250^0C – 400^0C) are polycrystalline [12]. It has been reported that the laser irradiation of the ITO films improves the structural, electrical and optical properties [25]. The laser treatment annihilates dislocations and promotes grain growth. Post deposition annealing in vacuum atmosphere is an effective method to decrease the resistivity of sputtered ITO films. Higuchi et al. have reported ITO films with resistivity 1.3x10^{-4} Ωcm after the annealing at 300^0C in vacuum with an improved crystallinity and transmittance [12]. The results of the post deposition annealing in air and vacuum showed that, in both cases the transmittance and crystallinity of the films improved and the surface topography didn't show any appreciable change. The resistivity of the ITO films is found to increase with air annealing above 300^0C, whereas the vacuum annealing showed decrease in resistivity. The resistivity is found to depend on the carrier concentration in the films. Carvalho et al. [13] studied the effect of rf power on the properties of ITO films deposited on transparent polymer substrates. Optical properties were sensitive to rf power below 45W and the surface morphology remained independent of rf power. The introduction of hydrogen into the sputtering gas during rf magnetron sputtering showed that

the surface morphology of the films improved and the films showed a reduced resistivity of 4.66 x 10^{-4} Ωcm with a transmittance of more than 80%. The films prepared by this technique didn't require any substrate heating or post deposition annealing [15]. Substrate temperature during the ITO deposition enhances crystallinity of the films. ITO films prepared by rf reactive magnetron sputtering onto glass substrates at different substrate temperatures showed a (222) peak showing a preferred orientation in the (111) direction. As the temperature increased, (400) peak intensity increases and results in a preferred orientation of (100) direction for the films prepared at 500^0C [17]. The resistivity of the ITO films deposited by PLD method is reported to decrease from 3.8×10^{-4} to 1.9×10^{-4} Ωcm as the substrate temperature increased from 25^0C to 300^0C. This might be due to the increase in the crystalline size with respect to the increase in the substrate temperature, thus reducing the grain boundary scattering and increasing the conductivity. This decrease in resistivity can also be due to the increase in carrier mobility [18].

In this chapter, the studies on the indium tin oxide thin films deposited by rf magnetron sputtering are presented. The films were deposited at room temperature and the influence of target to substrate spacing and the post deposition annealing on the structural, electrical and optical properties of these films are investigated.

5.3. Experimental details

ITO films were deposited on to glass substrates by rf magnetron sputtering at room temperature using an ITO target (5 cm diameter) containing 95 wt% of In_2O_3 and 5 wt% of SnO_2. The target used for sputtering was prepared from In_2O_3 (99.999 % pure) and SnO_2 (99.999 % pure) powders. The powders were mixed in a mechanical shaker for 1 hour, pressed into a 5 cm diameter pellet at 15000lb and then sintered at 1300^0C for 6hours in air. The sputtering time was adjusted in such a way that all the films studied have the same thickness irrespective of the substrate to target distance. The base pressure in the chamber was 5×10^{-6} mbar. Sputtering was carried out in

argon atmosphere at a pressure of 0.01 mbar with rf power of 20 watts. Deposition rate was found to decrease almost linearly from $35A^0$ /minute to $12 A^0$ /minute as target to substrate distance was increased from 4 to 8 cm (Fig. 5.1). The films prepared at room temperature were then annealed at various temperatures ranging from 100^0C to 300^0C in high vacuum (2×10^{-5} mbar) for 1hour.
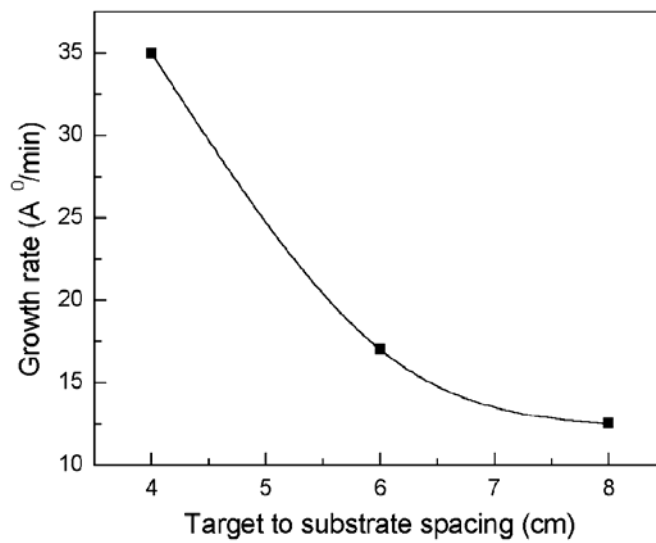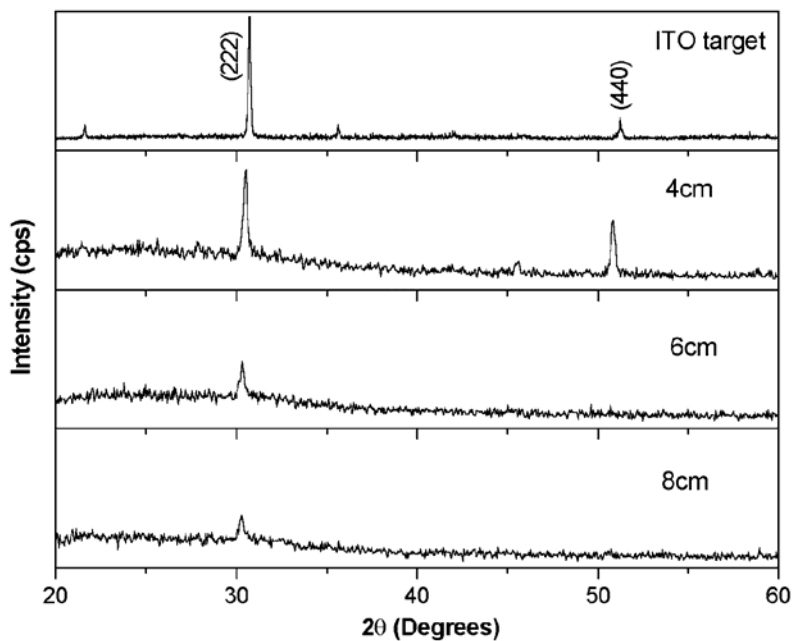

Fig.5.1 Growth rate of the ITO thin films for various target to substrate spacing. RF power = 20

The thickness of the films was determined by Tolansky's interference technique (see section 2.3.1). In the present study all the measurements were performed on the films having the thickness of 2500 A^0. Electrical measurements were carried out using a Hall measurement system (Model MMR technology H-50), which employs four-probe in Vanderpauw configuration (see section 2.3.6). Transmission spectra of the samples were recorded using a UV-VIS-NIR spectrophotometer (Hitachi U 3410). The crystallinity of the films were analysed using an X-ray diffractometer using the Cu-Kα radiation (1.5418 A^0).

5.4 Results and discussion

### 5.4.1 Influence of Target to substrate distance

The X-ray diffraction pattern of the ITO films deposited on glass substrates at various target to substrate spacings (T-S spacing = 4cm, 6cm, 8cm) is shown in figure 5.2. The substrates were not preheated intentionally. However, the substrate temperatures increased up to 55^0C during deposition when the T-S spacing was 4cm, 45^0C when the T-S spacing was 6cm and to 40^0C when the T-S spacing was 8cm. From the XRD pattern it is evident that the as deposited films are polycrystalline even though the crystallization temperature of ITO is 150^0C [26]. All of them showed a peak at $2\theta = 30^0$, which correspond to (222) plane of In_2O_3 [27]. This is because of the greater kinetic energy of the sputtered particles reaching the substrate surface.

Fig.5.2 XRD pattern of the ITO target and the as-deposited ITO thin films for various target to substrate spacing.

Generally, sputtered particles have kinetic energies of several electron volts. This kinetic energy enhances the surface migration of sputtered particles arriving at the substrate surface and the crystallinity of the films is greatly affected by them. Thus it is possible to deposit polycrystalline films even at room temperature by sputtering [28]. The crystallinity of ITO films showed a dependence on T-S spacing. With increase in T-S spacing, the kinetic energy of the sputtered particles reaching the substrate surface decreases. This retards the surface migration of sputtered particles and hence reduces the crystallinity of the films.

The grain size of the films as calculated from Scherrer's formula [29] is in agreement with the above result. The variation of grain size and the (222) peak intensity with T-S spacing is shown in figure 5.3. The decrease in grain size with increase in T-S spacing confirms the degradation in crystallinity with T-S spacing.
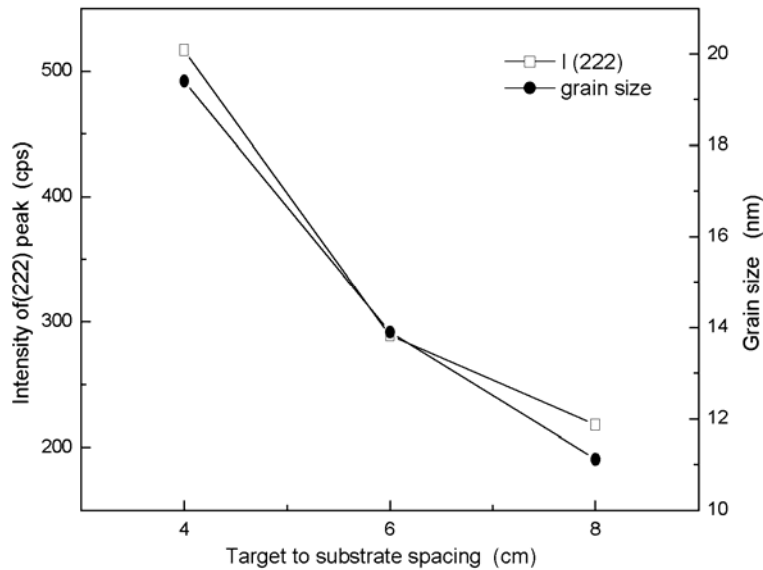
Fig.5.3 Variation of (222) peak intensity and the grain size with the target to substrate spacing for the as-deposited ITO films.

175

The crystallinity, transparency, electrical resistivity and mobility of the films prepared at T-S spacing of 6cm and 8cm showed similar variations on annealing as that of the variation in these properties for films deposited at a T-S spacing of 4cm. However, better film properties viz. lower resistivity, higher crystallinity and better transparency were observed for the films deposited at T-S spacing of 4cm in comparison with the other two T-S spacing.
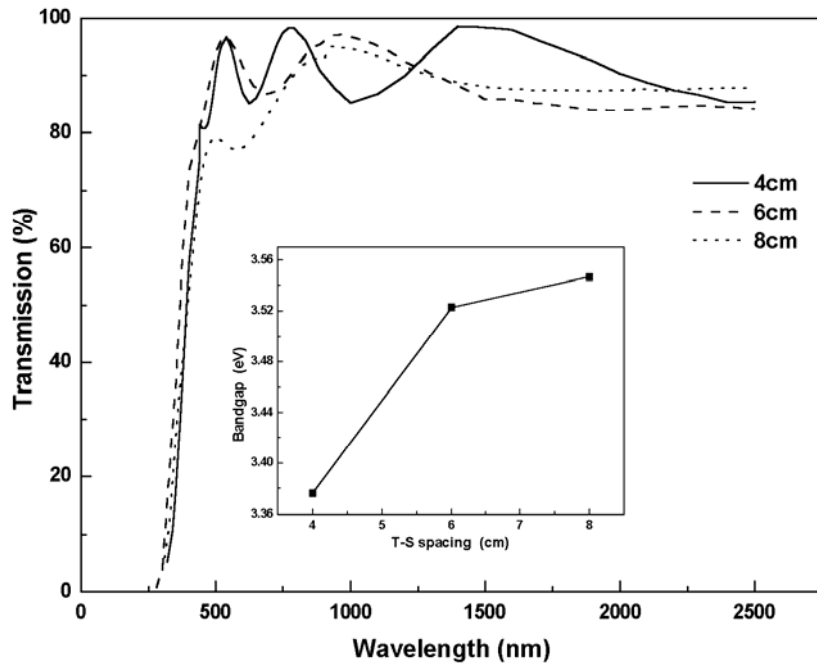

Fig.5.4 Optical transmission spectra of the as-deposited ITO thin films for various target to substrate spacing. The inset shows the variation in band gap with the T-S spacing.

The transmission spectra of the ITO films for various T-S spacings are shown in figure 5.4. All the films irrespective of T-S spacing were highly transparent. The average transmission in the visible region of the electromagnetic spectrum was >85%. The band gap of the ITO films was calculated from the transmission spectra. By assuming a parabolic band

structure for the material, the absorption coefficient and band gap can be related by the expression $(\alpha h\nu) = \beta(h\nu - E_g)^{1/2}$, since ITO is a direct band gap material [30]. The band gap E_g of the films was found out as described in section 2.3.5. It has been found that the band gap increases with increase in target to substrate spacing (Inset of figure 5.4).

The electrical characteristics of the films also showed dependence on target to substrate spacing. Figure 5.5 gives the variation of resistivity (ρ) and mobility (μ) with T-S spacing. The decrease in mobility and the increase in resistivity with T-S spacing are related to the degradation in crystallinity of the films with T-S spacing. At greater T-S spacing, the smaller grains increase the grain boundary scattering of carriers and hence reduce the mobility of the films, which result in higher resistivity.
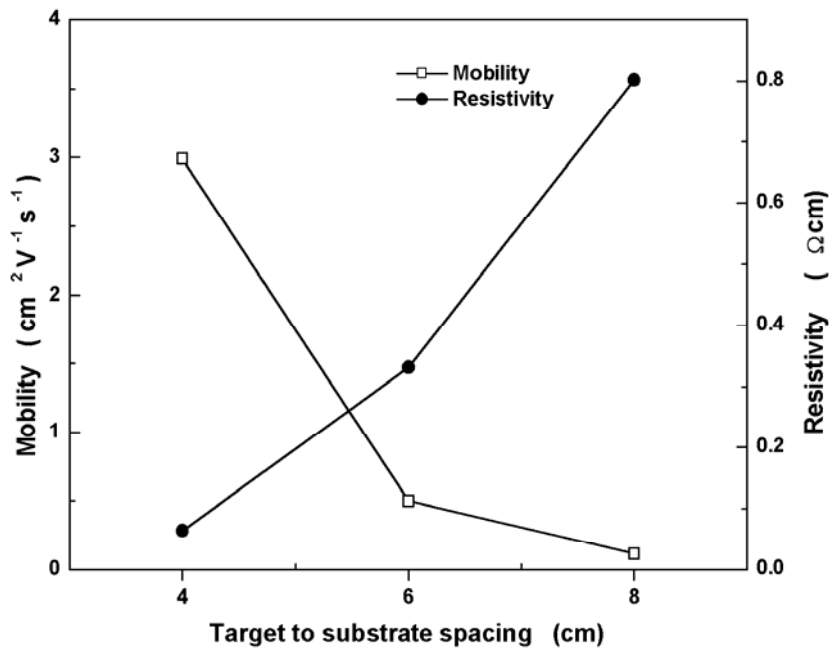

Fig.5.5 Variation in mobility and resistivity of the as deposited ITO thin films with the target to substrate spacing.

The X-ray diffraction pattern of the films for the various targets to substrate spacings shows that the (440) peak becomes prominent for the target to substrate spacing of 4cm (Fig. 5.2). From the measurement of resistivity and transmission, it can be seen that a target to substrate spacing of 4cm gives better crystalline and highly conducting films. The as prepared films have lower band gap when target to substrate spacing is 4cm. The band gap is found to increase with the increase in target to substrate spacing.

## 5.4.2 Effect of post deposition annealing

The X-ray diffraction patterns of the ITO films (target to substrate spacing = 4 and 6 cm) annealed at various temperatures in vacuum are shown in figures 5.6 and 5.7. All the films showed a peak at $2\theta = 30^0$ corresponding to (222) plane, and the peak at $2\theta = 51^0$ corresponds to (440) plane of In_2O_3.
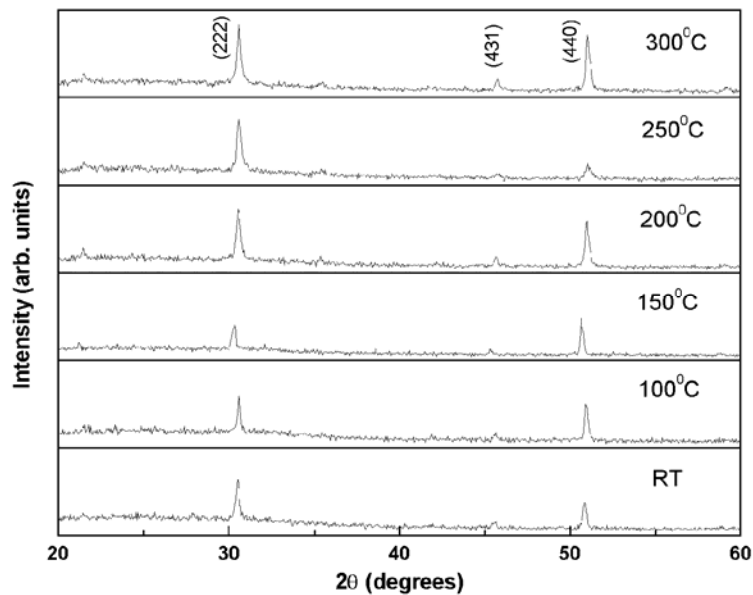
Fig.5.6 XRD pattern of the ITO thin films (T-S spacing= 4cm) deposited at room temperature and annealed at various temperatures.

178
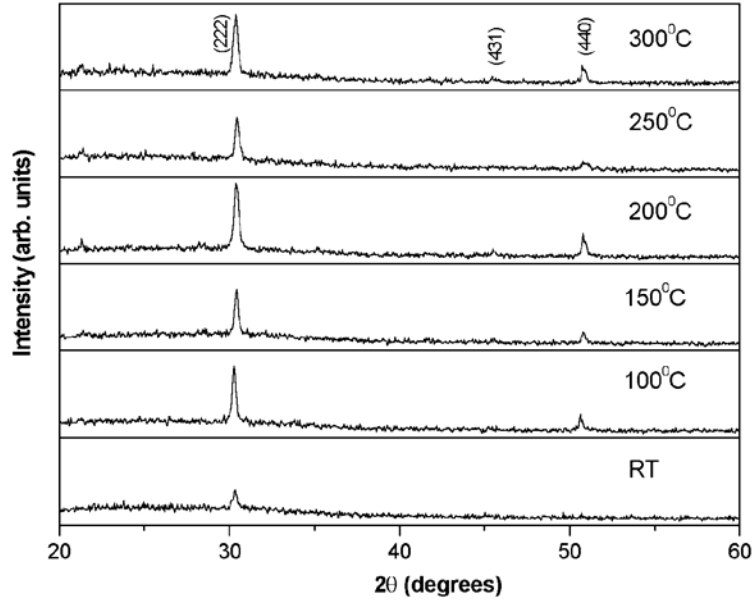
Fig.5.7 XRD pattern of the ITO thin films (T-S spacing= 6cm) deposited at room temperature and annealed at various temperatures.
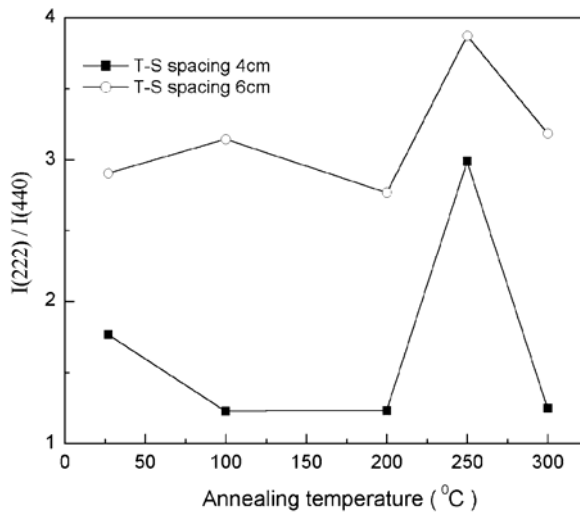
Fig.5.8 Variation of intensity ratio [I (222) / I (440)] of the ITO films deposited at target substrate spacings 4 cm and 6 cm with annealing temperature.

It was observed that, as the annealing temperature increases, the intensity of (222) peak increases and the intensity of (440) peak decreases; which is in

agreement with the literature [31]. The ratio of the intensities of the (222) peak to that of (440) peak increases with the annealing temperature and is maximum at 250^0C (Fig. 5.8). The films annealed at 250^0C shows a preferred orientation along (222) plane.

Table 5.1 The grain sizes and the lattice constants of the ITO thin films

| Annealing	Grain size (nm)		Lattice constant (A^0)	
temperature (^{0}C)	T-S = 4 cm	T-S = 6 cm	T-S = 4 cm	T-S = 6 cm
as-deposited	19.4	13.9	10.14	10.21
100	15.8	15.9	10.13	10.23
150	16.8	15.7	10.23	10.17
200	17.5	14.5	10.13	10.17
250	16.0	15.7	9.89	10.16
300	14.4	14.4	10.13	10.19

The grain size of the films was calculated from the XRD pattern using the Scherrer's formula and it was found that the grain sizes of the samples were in the range 14 to 20 nm. The lattice constants of the ITO films were also determined by analyzing the XRD patterns of the films. The calculated values of the average grain size and the lattice constants are given in Table 5.1. The lattice constant of the In_2O_3 thin films is reported as $10.117A^0$ [13]. Since the radius of Sn^{2+} ions (0.093nm) is greater than In^{3+} ions (0.079nm), the substitutional incorporation of Sn^{2+} ions into In^{3+} sites and the incorporation of Sn ions in the interstitial positions will result in a lattice expansion. All the films except the films annealed at 250^0C (T-S spacing = 4 cm) showed lattice expansion compared to the undoped In_2O_3. The estimated lattice constant of the films annealed at 250^0C was $9.89A^0$, which is same as that obtained for the ITO target used for the thin film deposition. The scanning electron micrographs of the as-deposited and the annealed ITO films (Fig. 5.9a and b) show that the crystallinity of the films improved due to the annealing with larger grains uniformly distributed over the surface.
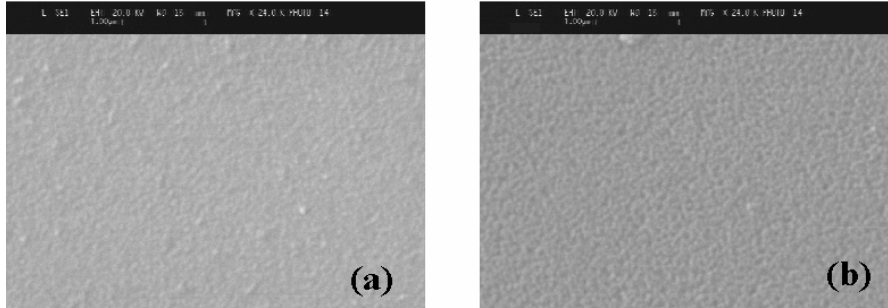
Fig.5.9 SEM pictures of ITO thin films (T-S spacing = 6cm) (a) as-deposited (b) annealed at 150^0C.
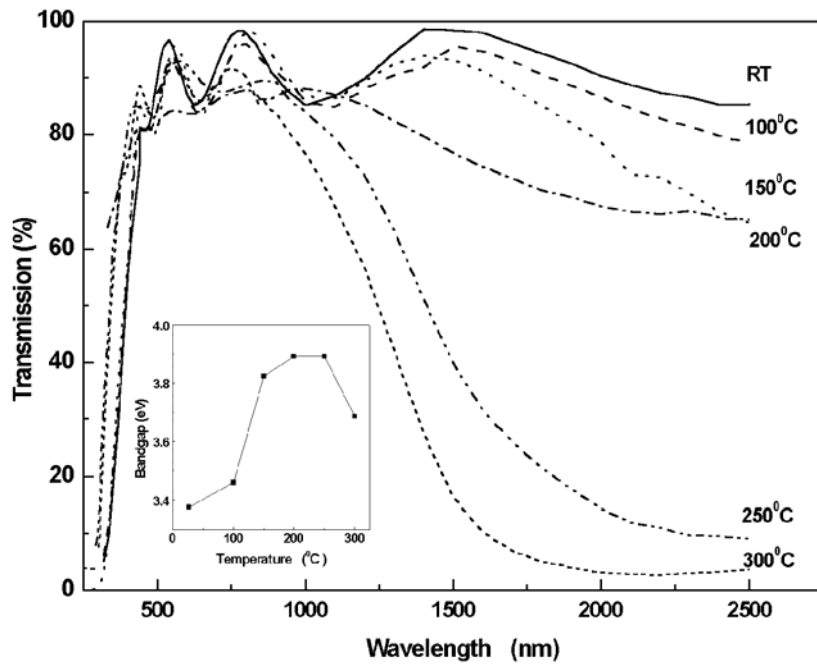
Fig.5.10 Optical transmission spectra of the ITO thin films (T-S spacing = 4cm) deposited at room temperature and annealed at various temperatures. The inset shows the variation in band gap with the annealing temperature.
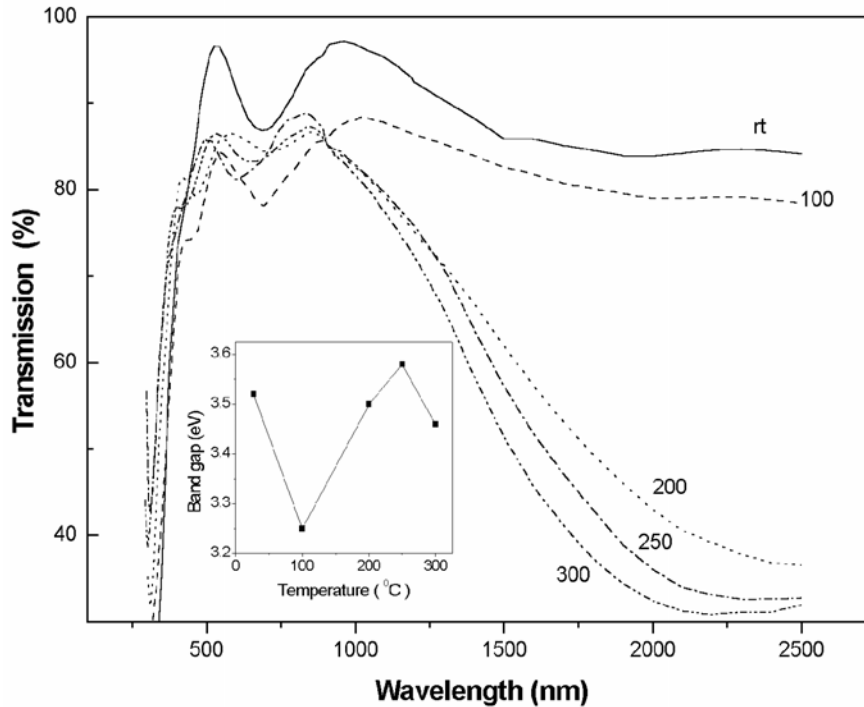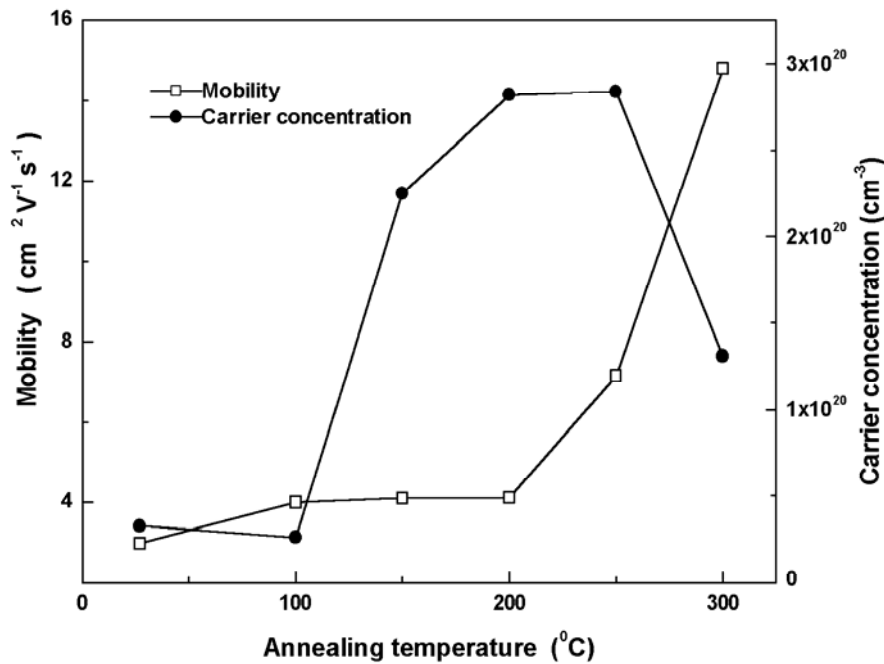
Fig.5.11 Optical transmission spectra of the ITO thin films (T-S spacing = 6cm) deposited at room temperature and annealed at various temperatures. The inset shows the variation in band gap with the annealing temperature.

The rf magnetron sputtered ITO films are highly transparent in the visible region and are reflecting in the IR region of the electromagnetic spectrum. The reflecting edge shifts towards the lower wavelength region on annealing the film at high temperature. The shift in reflecting edge is due to increase in carrier concentration. The transmission spectra of the ITO films deposited with a target to substrate spacing of 4 and 6 cm are shown in figures 5.10 and 5.11.

The band gap of ITO films increase with annealing temperature showed a maximum at 250^0C (3.89eV) and then decreased. The variation of band gap with annealing temperature is shown in the insets of figures 5.10 and 5.11. The increase in band gap can be explained on the basis of Burstein-Moss effect [33]. Burstein-Moss shift is proportional to carrier concentration. The

variation of the carrier concentration and mobility of the ITO films (T-S spacing = 4cm) with the annealing temperature is shown in figure 5.12. The carrier concentration increases with annealing temperature and is maximum at 250^0C. Increase in carrier concentration with increase in annealing temperature results in band gap widening showing a maximum at 250^0C. The annealed films exhibited high transmission in the visible region with long tail in the IR region. It was seen that the reflecting edge shifted towards the lower wavelength region on annealing in vacuum (Figures 5.10 and 5.11). The shift in reflecting edge is due to increase in carrier concentration introduced by the oxygen deficiencies created during annealing.

Fig.5.12 Mobility (μ) and carrier concentration (n) of the ITO thin films annealed at various temperatures (T-S spacing = 4cm).

The refractive index of the ITO film was determined from the transmission spectra of the film by the method of Manifacier et al. [34] as described in section 2.3.5. The refractive index of the films (Fig.5.13) remains almost a

constant in the visible range ($\approx$1.8), which is in close agreement with the value reported in literature [35].
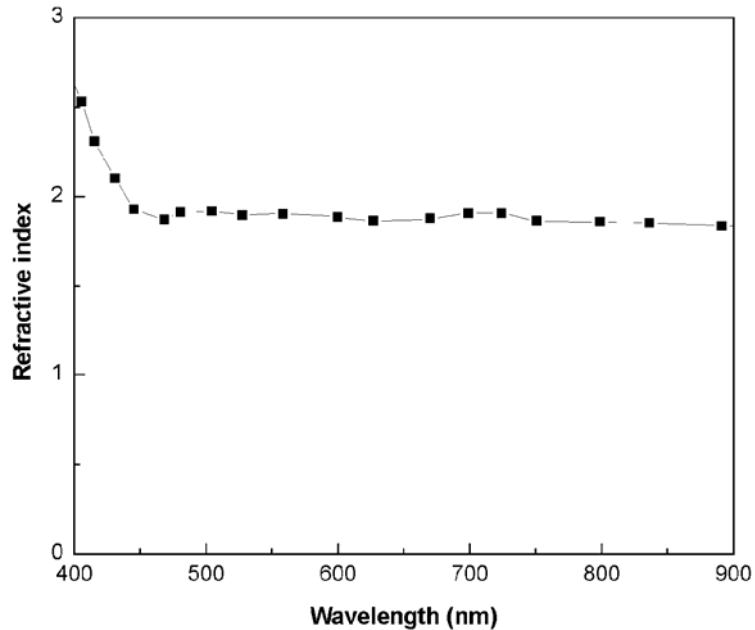

Fig.5.13 Variation in refractive index of the as-deposited ITO films with the wavelength (T-S spacing = 4cm).

The resistivity of the ITO films was found to decrease with increase of annealing temperature. The lowest resistivity of 3.07 x 10^{-3} Ωcm was obtained for the film prepared with a target to substrate distance of 4cm and then annealed at 250^{0}C. The resistivity showed similar behaviour on annealing, for the films prepared at various target to substrate spacings (Fig.5.14). The mobility of the ITO films increased with the increase of annealing temperature (Fig.5.12). In the case of ITO, oxygen deficiency is one of the reasons for high conductivity. Oxygen deficiencies induce free electrons as conduction carriers [36]. Vacuum annealing creates oxygen deficiency and this reduces the resistivity of the ITO films. The increase in carrier concentration, mobility and better crystallinity of the films are also

responsible for the decrease in resistivity. The films annealed at 250^0C showed a preferred orientation in the (222) plane and possess minimum resistivity.
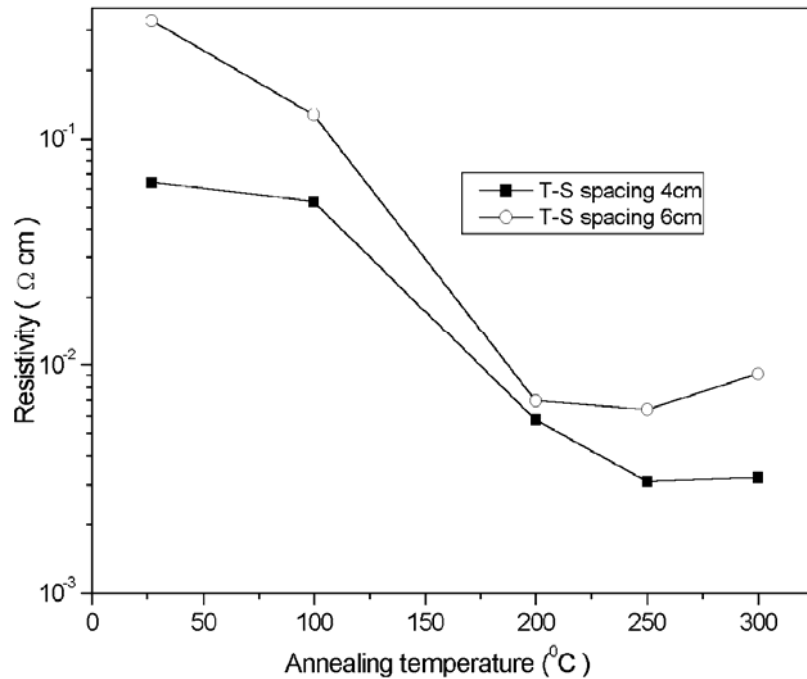
Fig.5.14 Variation in resistivity of the ITO thin films with the annealing temperature (T-S spacing = 4 and 6cm).

5.5 Conclusion

Tin doped indium oxide films were prepared at room temperature by rf magnetron sputtering. The effect of vacuum annealing and the target to substrate spacing, on the structural, electrical and optical properties were investigated. The films deposited at a target to substrate spacing of 4cm showed better crystallinity, transparency and low resistivity. The variation in optical and electrical properties of the ITO films with the annealing showed

185

similar behaviour irrespective of the target to substrate spacing. The films show a preferential orientation in the (222) plane. The X-ray diffraction pattern of the ITO films annealed at 250^0C shows the maximum peak intensity for the (222) plane. The resistivity of the film decreases with the annealing temperature and resistivity is minimum at 250^0C. The carrier concentration and band gap of the films were maximum for an annealing temperature of 250^0C.

References

[1] K. Badeker, Ann. Phys. 22 (1907) 749

[2] K. L. Chopra, S.Major and D. K. Pandya, Thin Solid Films 102 (1983) 1

[3] A.Suzuki, T.Matsushita, T. Aoki, A. Mori and M. Okuda, Thin solid films 411 (2002) 23

[4] C. N. Carvalho, A. Luis, O. Conde, E. Fortunato, G. Lavareda and A. Amaral, J. Non-crystalline solids 299-302 (2002) 1208

[5] D. Vaufrey, M.B. Khalifa, J. Tardy, C. Ghica, M.G. Blanchin, C. Sandu and J.A. Roger, Semicond. Sci. Technol. 18 (2003) 253

[6] Y.C. Park, Y.-S. Kim, H.-K. Seo, S.G. Ansari, H.-S. Shin, Surf. Coat. Technol. 161 (2002) 2

[7] D.E. Mortan and A. Dinca, Vacuum Technology & Coating. (2000) 53

[8] Y. Shigesato, N. Shin, M. Kamei, P.K. ong, I.Yasui, Jpn. J. Appl. Phys. 39 (2000) 6422

[9] S. Seki, Y. Sawada, T. Nishide, Thin solid films 388 (2001) 21

[10] Yoichi Hoshi, Takakazu Kiyomura, Thin solid films 411 (2002) 36

[11] F.O.Adurodija, H.Izumi, T. Ishihara et al, J.Appl.Phys 88, 7(2000) 4175

[12] H.L.Hartnagal, A.L.Dawar, A.K.Jain, C.Jagadish, Semiconducting Transparent Thin Films, Institute of Physics Publishing, London 1995

[13] B.G. Lewis and D.C. Paine, M.R.S. Bulletin 25 (2000) 22

[14] J. C. C. Fan and J. B. Goodenough, J. Appl. Phys. 48 (1977) 3524

[15] H. Odaka, Y. Shigesto, T. Murakami,S. Iwata, Jpn. .J. Appl. Phys. 40 (2001) 3231

[16] C.G. Granqvist, A. Hultaker, Thin solid films 411 (2002) 1

[17] I. Hamberg and C.G. Granqvist, Phys. Rev. B 30 (1984) 3240

[18] I. Hamberg and C.G. Granqvist, J. Appl. Phys. 60 (1986) R123

[19] C.W.Ow-Yang, Y. Shigesato and D.C. Paine, J. Appl. Phys. 88 (2000) 3717

[20] P.K. Song, Jpn. J. Appl. Phys. 37 (1998) 1870

[21] D.C. Paine, T. Whitson, D. Janiac, R. Beresford, C.W.Ow-Yang and B. Lewis, J. Appl. Phys. 85 (1999) 8445

[22] W.F. Wu, B.S. Chiou, Thin solid films 298 (1997) 221

[23] S. Ishibashi, Y. Higuchi, Y. Ota and K. Nakamura, J. Vac. Sci. Technol. A 8 (1990) 1399

[24] Y. Shigesato, S. Takaki and T. Haranoh, J. Appl. Phys. 71 (1992) 3356

[25] J. Echigoya, S. Kato and H. Enoki, J. Mater. Sci.: Mater. Electron. 3 (1992) 168

[26] P.K. Song, Y. Shigesato, I. Yasui, C.W.Ow-Yang and D.C. Paine, Jpn. J. Appl. Phys. 37 (1998) 1870

[27] JCPDS card No. 06-0416

[28] P.K. Song, Y. Shigesato, M. Kamei and I. Yasui, Jpn. J. Appl. Phys 38 (1999) 2921

[29] B.D. Cullity and S.R. Stock, Elements of X ray diffraction, Third edition, Prentice Hall, New Jersey (2001)

[30] J.Tauc,R. Grigorovici and A.Vancu, Phys. Status Solidi 15,627 (1966)

[31] M. Higuchi, S. Uekusa, R. Nanako, K. Yokogawa, Jpn. J. Appl. Phys 33 (1994) 302

[32] M.K. Jayaraj, S. Lorette, A. Agati and A. Parretta, Phys. Stat. Sol. (a) 155 (1996) 115

[33] E. Burstein, Phy Rev 93 (1954) 632

[34] J.C. Manifacier, J. Gasiot, J.P. Fillard, J. Phys. E: Scientific Instruments 9 (1976) 1002

[35] H. Kim, C.M. Gilmore, A. Pique, J.S .Horwitz, H. Mattoussi, H. Murrata, Z.H. Kafafi and D.B. Chrisey, J. Appl. Phy. 86 (1999) 6451

[36] F.O. Adurodija, H. Izumi, T. Ishihara, H. Yohioka, M. Motoyama, Solar Energy Mater. Solar Cells 71(2002) 1

CHAPTER 6

Summary and outlook

Chalcopyrite copper ternary compounds are the most promising absorber materials for polycrystalline thin film solar cells. The operational lifetimes of this type of solar cells are long due to their extraordinary stability. A record efficiency of 19.2% has been reported for CIGS solar cells with co-evaporated absorber layer. In order to lower the production costs of photovoltaic modules, alternative, low-cost deposition methods need to be developed. With this out look we have optimized the processing parameters of the materials for a complete heterojunction solar cell. The methods of deposition appropriate for each layer was chosen viz; chemical bath deposition for window layer, flash evaporation and two-stage process

for absorber layer, and rf sputtering for transparent conductor. Different characterisation tools such as, x-ray diffraction, optical transmission and absorption studies, electrical resistivity measurements, energy dispersive X-ray analysis, scanning electron microscopy etc. were used to analyse the structure, morphology, composition, electrical and optical properties of the materials prepared.

Chemical bath deposition was effectively employed to deposit different buffer layers for chalcopyrite based solar cells. CdS films with high transparency and desirable carrier concentration was prepared by this technique and characterized. A wide band gap window layer, (CdZn)S films were also prepared with a possibility of engineering the band gap from 2.43 to 2.66eV. The higher resistivity of these (CdZn)S films were reduced by doping indium during chemical bath deposition. Thus a low resistive wide band gap buffer layer was prepared and characterized by the simple low cost chemical bath deposition technique, which can be used as a heterojunction partner with CIS absorber layers to yield more efficient solar cells. A cadmium free wide band gap buffer layer- ZnS, with high transparency was also prepared by CBD method. It has also been demonstrated that an intrinsic ZnO film can be prepared by a simple technique – namely the thermal oxidation of the chemical bath deposited ZnS film.

CuInSe$_2$ absorber layers were prepared by the flash evaporation. Device quality films were not obtained since the as deposited films contain binary phases. Post deposition annealing in selenium vapour improved the crystallinity and show chalcopyrite structure for the films. The films were having a slightly In-rich surface, which is beneficial for the device performance since it form a homojunction with the n-type window layers. Two-stage process was optimised to prepare single phase, p-type CuInS$_2$ films. The experimental setup is relatively simple, and the advantages of the method include the potential for upscaling to large areas and production volumes.

Polycrystalline Tin doped Indium oxide (ITO) thin films were deposited by rf magnetron sputtering at room temperature. The films transparent and conducting properties improved with the post deposition vacuum annealing. The result of low temperature sputtering is of importance in the fabrication of flexible solar cells, where the films can be prepared on plastic substrates.

The growth technique for the different layers required for solar cell has been optimized. With this know-how a solar cell with $Mo/CuInS_2/CdS$ structure has been fabricated [1], which shows an efficiency of 5.6%. Further efforts are to be concentrated for improving the performance of this solar cell. One of the problems faced during the device integration was the poor adhesion of the absorber layer with molybdenum substrates. Poor junction quality was also observed due to the inter diffusion of the layers during the device processing. Further optimization can lead to devices with reasonable efficiency of 12-15% by the processing techniques, which has moderate cost. The methodology of two-stage process can be further extended to prepare $Cu(In,Ga)Se_2$ and $Cu(In,Ga)(S,Se)_2$ absorber layers which may show higher efficiencies.

References

[1] Asha A.S., Rahana Yoosuf, Sukesh G., Aldrin Antony and M.K. Jayaraj, Int.Conference. on Electrochem. Power System – 2 (Hyderabad, India, December 2004)